微小噴孔ノズルから超高圧で噴射したディーゼル噴霧の混合気形成と燃焼

学位取得年月（2008年9月）

張　　武

Mixture Formation and Combustion of Diesel Sprays from Micro-Hole Nozzles under Ultra-High Injection Pressures

by

Wu Zhang

Dissertation

Submitted to the Graduate School of Engineering

of Hiroshima University

in partial fulfillment of the requirements

for the degree of

Doctor of Philosophy

Hiroshima University

September, 2008

Acknowledgements

I would like to thank my supervisor, Professor Keiya Nishida, for his guidance and encouragement during the course of the work. Without his insightful advice and valuable assistance this work would not have been possible. I also would like to express my sincere gratitude to the committee members, Professors Satoru Ishizuka, Shirou Taki, and Hideto Yoshida, for reviewing the draft and for helpful discussion.

This project was financially supported by ISUZU Advanced Engineering Center, Ltd. My sincere thanks go to Mr. Minato for his valuable suggestions on the research proposal and data analyses. I also thank Mr. Suzuki for his assistance in preparing the experiments and in designing the impingement walls.

I would like to appreciate Professor Hiroyuki Hiroyasu for his insightful suggestions on my research. I also gratefully acknowledge Professor Xiyan Gao, my previous supervisor at Dalian University of Technology, for his advice and encouragement. Sincere thanks also go to Professor Yuyin Zhang for his help both in research and in everyday life.

I am indebted to my colleagues in Professor Keiya Nishida's group: Mr. Tetsuya Manabe, for initial training with instruments; Mr. Yuhei Matsumoto, for helping me solve various problems; Mr. Daisuke Miura, for his great assistance in carrying out the experiments; Mr. Jiangping Tian, for his assistance in preparing and conducting the experiments. Special thanks go to Dr. Jian Gao for sharing his experience on laser diagnostics. Finally, I would like to thank all of the students, researchers, and professors at the Laboratory of Combustion Engineering.

Last but not least, my deepest gratitude goes to my family, especially to my wife, Shanghong Cai, for her consistent love, encouragement, and support.

Mixture Formation and Combustion of Diesel Sprays from Micro-Hole Nozzles under Ultra-High Injection Pressures

Wu Zhang

Under the Supervision of Professor Keiya Nishida

At Hiroshima University

Abstract

The objective of this work is to get a better understanding of the mixture formation and combustion processes of Diesel sprays. The experimental study, focusing on the characteristics of Diesel sprays from micro-hole nozzles under ultra-high injection pressures, was conducted in a high-temperature high-pressure constant volume vessel using the laser absorption-scattering (LAS) technique and combustion diagnostics.

Firstly, the non-evaporating free spray was visualized using a direct photography system. The effects of the nozzle hole diameter, injection pressure, and ambient density on the spray tip penetration length were investigated. The dependence of the penetration on the nozzle hole diameter was clarified. Then, the preliminary experiment was made of the measurements of both liquid and vapor fuel for the evaporating free spray at a constant ambient density using the LAS technique and axisymmetric data processing method. The fundamental influence of injection parameters on the air entrainment, fuel vaporization, and drop size after the end of injection were acquired.

Subsequently, the flat wall impinging sprays were comprehensively investigated. The injection parameters were varied, simulated engine operating conditions were tested, and the measurement of the evaporating spray was carried out from the timing near the start of injection to the timing after the end of the injection. The mixing rate was

introduced to analyze the mixing process around the end of injection. The effects of the wall impingement and fuel evaporation were clarified experimentally. And the detailed evolution of the spray plumes was presented. To clarify the theoretical nature of the spray from micro-hole nozzles, a wall-impinging gas jet theory was employed to predict the spray tip penetration length.

To correlate the fundamental findings with some practical applications, 2-D piston cavity shape sprays and 2-hole nozzle sprays were investigated. The difference in the fuel vaporization for different spray types was clarified, which provides some useful information for the application of micro-hole nozzles and ultra-high injection pressures in real engines.

Finally, the auto-ignition and flame structure of the spray combustion were investigated using a high-speed video camera system. The soot luminosity was discussed qualitatively. The OH chemiluminescence was used as a marker of the auto-ignition and a measure of the flame lift-off length. The discussion was performed on the basis of the correlation between spray characteristics and combustion process. The primary findings of this work may provide useful information for the design of new Diesel fuel injection systems and for the calibration of predicative spray models.

Table of Contents

List of Tables

List of Figures

Nomenclatures

AEOI	after end of injection
ATDC	after top dead center
BP	band-pass
CCD	charge-coupled device
CI	compression ignition
CN	cetane number
*CH**	excited methylidyne radical
CO	carbon monoxide
C_a	area-contraction coefficient
C_d	discharge coefficient
C_f	constant in Eq. (5.4)
C_v	coefficient of velocity
d	nozzle hole diameter
DMN	1,3-Dimethylnaphthalene
EOI	end of injection
FIE	fuel injection equipment
F_m	function of Reynolds number
HC	hydrocarbon
HCCI	homogeneous charge compression ignition
HCDC	homogeneous charge Diesel combustion
HiMICS	homogeneous charge intelligent multiple injection combustion system
HTO	high temperature oxidation
IMEP	indicated mean effective pressure
ISFC	indicated specific fuel consumption

K	kinematic momentum flux
L	distance from nozzle tip to impingement point
LIEF	laser induced exciplex fluorescence
LTO	low temperature oxidation
LAS	laser absorption-scattering
LTC	low temperature combustion
m	constant in Eq. (5.4)
MK	modulated kinetics
MTBE	metyl-t-butyl ether
MULDIC	multiple stage Diesel combustion
M_a	mass of entrained gas
M_f	mass of injected fuel
M_l	mass of liquid phase fuel
M_v	mass of vapor phase fuel
Nd:YAG	neodymium-doped yttrium aluminum garnet
NTC	negative temperature coefficient
NO_x	nitrogen oxides
*OH**	excited hydroxyl radical
PAH	polycyclic aromatic hydrocarbon
PLII	planar laser-induced incandescence
PLIF	planar laser-induced fluorescence
PM	particulate matter
PREDIC	premixed lean Diesel combustion
P_a	ambient pressure
P_{inj}	injection pressure measured in common rail

S	spray tip penetration length
SI	spark ignition
SMD	Sauter mean diameter
SOF	soluble organic fraction
S_{Radial}	distance from impingement point to furthest location of fuel
S_{Axial}	distance from nozzle tip to impingement point
t	time after end of injection
t_s	laser shot timing after end of injection
THC	total hydrocarbons
T_a	ambient temperature
TDC	top dead center
U_0	injection velocity at nozzle hole exit
$UNIBUS$	uniform bulky combustion system
UV	ultraviolet
ϕ_{Liquid}	equivalence ratio of liquid phase fuel
ϕ_{Vapor}	equivalence ratio of vapor phase fuel
ρ_a	ambient density
ρ_f	fuel density
τ	injection duration
τ_{id}	ignition delay

Chapter 1 Introduction

1.1 MOTIVATION

Since a systematic control of the mixture formation in direct injection (D.I.) Diesel engines enables considerable improvements in the combustion process in terms of the reduced fuel consumption and emissions, the optimization of injection system is becoming more and more important recently. A fundamental understanding of the governing mechanisms of the mixture formation and combustion processes is, thus, critical both for improving the current design of injection systems and for developing the predictive models.

A great deal of research work has been conducted on improving the combustion process by adjusting the parameters of injection systems. It has been approved that decreasing nozzle hole diameter and increasing injection pressure are two effective approaches to improve the combustion characteristics. High pressure fuel injections are recommended for improving the D.I. Diesel engine performance and reducing particulate matters (PM). In addition, the increased injection pressures usually shorten the time required for the droplet vaporization and combustible mixture preparation and then reduce the ignition delay. At the same time, in various published experimental results, it has been shown that the Diesel engine emissions are reduced significantly by decreasing the nozzle hole diameter. In small-bore high-speed D.I. Diesel engines, information on the spray/wall interactions is essential to understand the detailed mechanism and to verify the spray and combustion models in engine simulations.

Many experimental studies have been carried out to provide qualitative and quantitative information, but most of them have focused on the investigation using the conventional nozzle hole diameters ($d > 0.10$ mm) and normal injection pressures ($P_{inj} <$ 200 MPa). At the same time, a few researchers have employed micro-hole nozzles and ultra-high injection pressures mainly to focus on the combustion process, exhaust emissions, and engine output performance. In current archives, there are few

fundamental experimental data, which are needed for successful engine design and modeling, about the spray and mixture characteristics with the micro-hole nozzle and ultra-high injection pressure.

1.2 OBJECTIVES AND APPROACHES

The objective of this research is to study the spray and combustion processes with the micro-hole nozzle and ultra-high injection pressure and to get a better understanding of the spray and mixture formation, ignition, and flame propagation. Fundamental knowledge of the governing mechanisms of the spray and combustion processes allows the improvement in predicative models and in developing the new combustion concepts in D.I. Diesel engines.

In this study, the laser absorption-scattering (LAS) technique was adopted to obtain the qualitative and quantitative information on the simulated D.I. Diesel sprays. Dimethylnaphthalene (DMN), a test fuel of the LAS technique, was used as the simulator of the Diesel fuel. For axisymmetric sprays (free and flat wall impinging sprays from single-hole nozzles), measurements were made of the liquid and vapor fuel concentrations, mass of entrained gas, and probability function in the mixture; for non-axisymmetric sprays (2-D piston cavity shape wall impinging spray from single-hole nozzles and sprays from a 2-hole nozzle), measurements were made of the mass of vapor fuel and projected mass concentration distribution. In addition, a high speed video camera was used to visualize the ignition and combustion process. The OH chemiluminescence and soot luminosity were investigated to qualitatively analyze the effects of nozzle hole diameter and injection pressure on the auto-ignition, flame lift-off, and soot formation.

Experiments were conducted at a range of nozzle hole diameters, injection pressures, ambient densities, and impingement conditions, which provided a systematic evaluation of the effects of various parameters on the mixture formation and combustion processes of Diesel sprays.

1.3 OUTLINES

To present this work, the dissertation is organized as follows: a review of the mixture formation and combustion process in D.I. Diesel engines and diagnostic techniques for the spray and combustion are given in Chapter 2. Chapter 3 describes the experimental configurations, principle of LAS technique, and data processing methods. The preliminary experiments on non-evaporating free sprays using a high-speed video camera and on evaporating free sprays using the LAS technique are presented in Chapter 4. The structure and characteristics of a flat wall impinging spray are comprehensively discussed in Chapter 5. To clarify the correlation between the fundamental findings and practical applications in Diesel engines, 2-D piston cavity shape impinging sprays and 2-hole nozzle sprays are given in Chapter 6 and 7 respectively. The measurement of the spray combustion and the correlation between mixture formation and combustion processes are described Chapter 8. Finally, general conclusions on mixture formation and combustion processes of Diesel sprays from micro-hole nozzles under ultra-high injection pressures are summarized in Chapter 9.

Chapter 2 Literature Review

2.1 COMBUSTION CONCEPTS IN DIESEL ENGINES

Diesel engines are the most efficient energy converters among all reciprocating engines, with a conversion efficiency of chemical into mechanical energy that can be higher than 50% (Kamimoto and Kobayashi, 1991). This is due to a thermodynamic cycle with a high compression ratio, reduced pumping losses during the induction process, and a capability to burn very lean mixture. Moreover, Diesel fuel is more energetic and can provide compactness of energy storage when compared to gasoline. Diesel combustion, at least up to now, is stratified and lean, allowing for low hydrocarbon (HC) and carbon monoxide (CO) emissions. Since part of the mixture burns in a rich regime, soot can occur, and a tradeoff as always is to be found with nitrogen oxides (NO_x) emission depending on the peak pressure timing.

Although the current Diesel engines have achieved a great success in noise and emission reduction by employing the sophisticated electronically controlled fuel injection system and advanced aftertreatment techniques, the conventional diesel combustion concept cannot meet the continuingly stringent emission regulations on their own. At the same time, emission aftertreatment systems for a Diesel engine are more difficult and costly than those for a spark ignition (SI) engine. The increased concerns of the energy and environmental issues have pushed Diesel engine technology towards a better control of the in-cylinder processes. Consequently, new combustion concepts have been proposed and investigated. In the following sections, the conventional Diesel combustion will be described briefly and the homogeneous charge compression ignition (HCCI) combustion in Diesel engines will be reviewed.

2.1.1 Conventional Diesel Combustion

In a D.I. Diesel engine, fuel is injected directly into the combustion chamber through a multi-hole nozzle. The temperature and pressure at the compression top dead

center (TDC) are in the range of 1000~2000 K and 4~12 MPa respectively (Kamimoto and Kobayashi, 1991). A typical heat-release-rate diagram for a D.I. Diesel engines are shown in **Fig. 2.1** (Heywood, 1988). The overall Diesel combustion process can be divided into four phases. After an ignition delay period of about one millisecond at normal operating conditions combustion starts. The primary combustion process consists of an initial premixed combustion phase and a mixing-controlled diffusion combustion phase, followed by a late combustion phase. During the premixed combustion phase, the heat release rate is very high and the flame luminosity is very weak, or transparent. On the contrary, during the diffusion combustion phase, the heat release rate becomes much lower and the flame luminosity becomes much brighter.

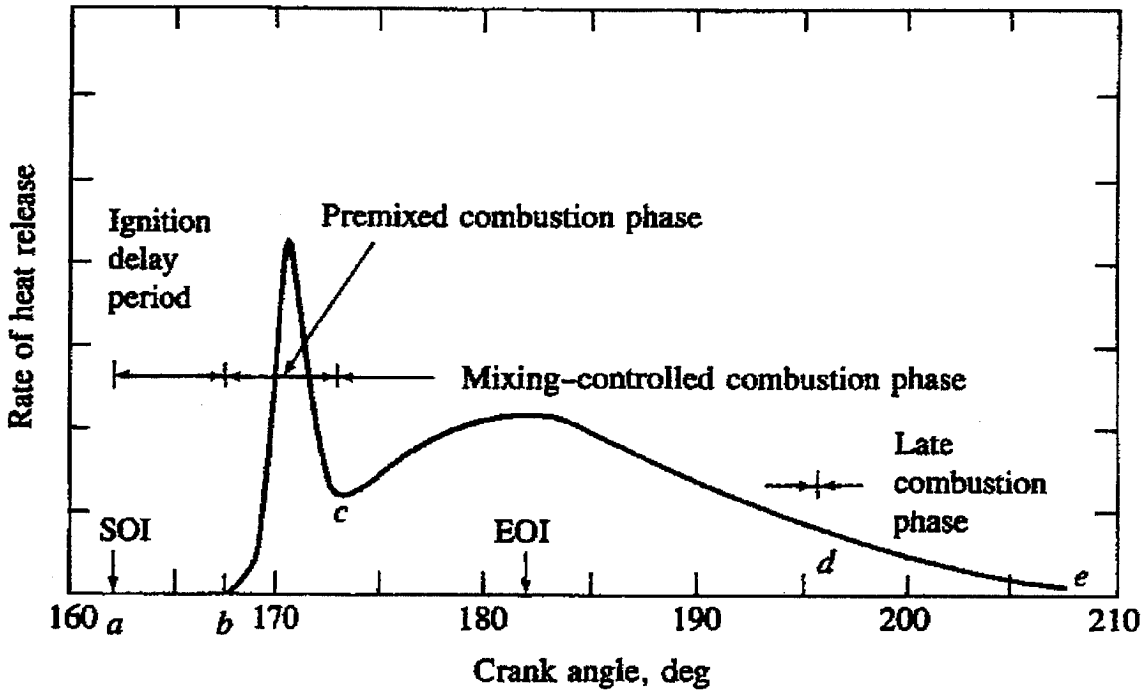

Figure 2.1 Typical D.I. Diesel engine heat-release-rate diagram identifying different Diesel combustion phases (Heywood, 1988)

The latest description of the D.I. Diesel engine combustion is summarized by Dec and coauthors (Dec, 1997, Flynn et al., 1999). **Figure 2.1** provides an integrated perspective of the thermal and chemical variations inside the burning fuel plume. Fuel is injected into the hot ambient air after the start of injection. More hot air is entrained

into the jet as the penetration increases, thus resulting in the increase in the temperature. The mixture of vaporized fuel and hot air forms a sheath around the jet's periphery and at the leading edge of the jet. The auto-ignition point examined using the chemiluminescence imaging occurs at multiple points of the downstream region of the fuel jet nearly simultaneously. Polycyclic aromatic hydrocarbons (PAHs), soot precursors formed by fuel pyrolysis (Tree and Svensson, 2007), is determined using the planar laser-induced fluorescence (PLIF). The results show that the premixed burn occurs volumetrically throughout the cross section of the leading portion of the jet. At the same time, the OH-radical PLIF images indicate that a thin diffusion flame is formed around the periphery of the burning plume. As shown in **Fig. 2.2**, no free oxygen is available inside the diffusion flame sheath, providing an ideal environment for soot formation. A great deal of soot generated in this region diffuses to the boundary and is consumed by the diffusion flame. The high temperatures and high oxygen concentrations at the diffusion flame interface provide an ideal environment for NO_x formation. After the end of injection, no cold fuel is injected into the partial burning zone. The soot oxidation becomes much stronger than soot production. Therefore, most of the soot formed at the early phase of the combustion is consumed at the late phase and the net soot emissions are reduced.

According to above discussion, the key issue of emission control in D.I. Diesel engines is how to reduce the soot and NO_x simultaneously. This is the so-called soot-NO_x trade-off presented in **Fig. 2.3** (Baumgarten, 2006). To reduce the NO_x formation, the local temperature above 2000~2200 K should be avoided during the combustion process. One possible conventional method is retarding the injection timing to shift the main combustion phase into the expansion stroke. This results in the decrease in the maximum temperature and NO_x formation, whereas the soot oxidation is inhibited by the relatively low temperature. In addition, the fuel economy is deteriorated by the longer late combustion phase. On the contrary, the advanced injection timing results in the

increase in the NO_x emission and in the decrease in the fuel consumption and smoke emission.

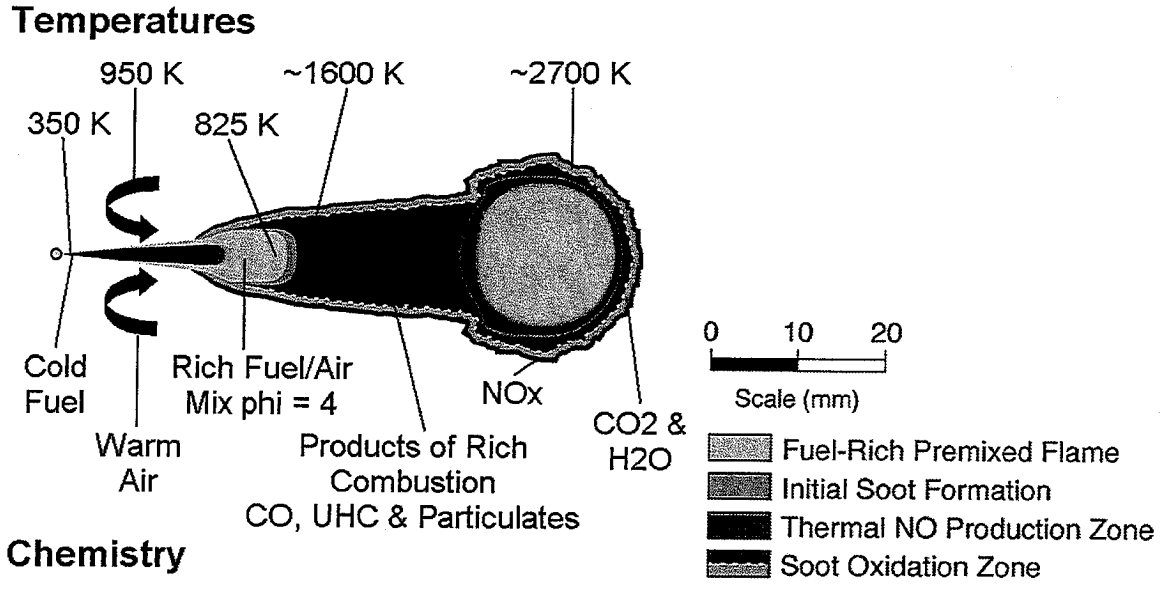

Figure 2.2 Schematic of a quasi-steady burning jet from laser measurements (Flynn et al., 1999)

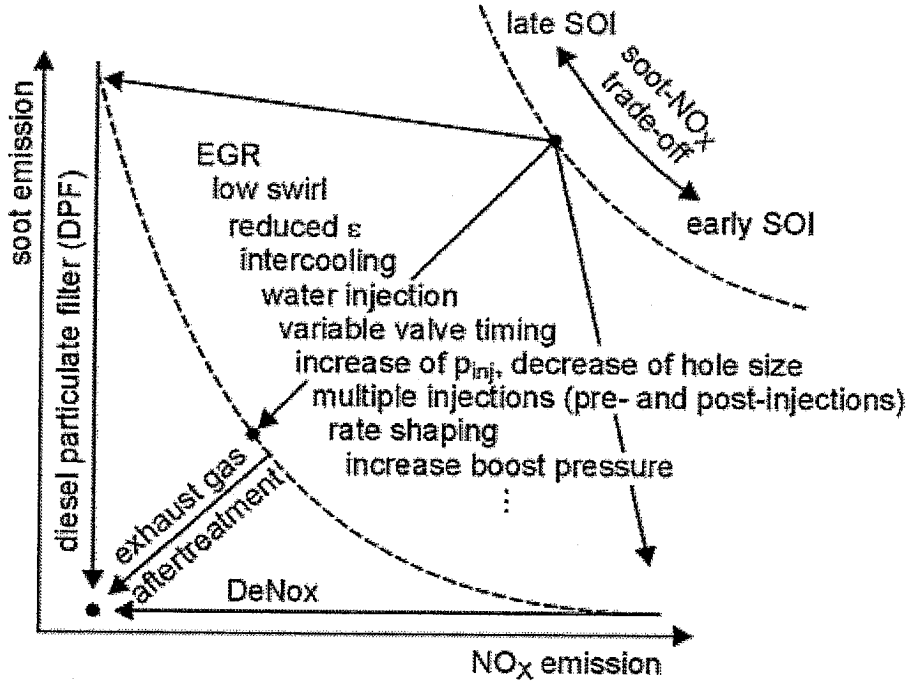

Figure 2.3 Soot-NO_x trade-off: measures for reduction of soot and NO_x in engine emissions (Baumgarten, 2006)

2.1.2 HCCI Combustion in Diesel Engines

Over the last 100 years, no fundamental changes have been implemented in commercial Diesel engines. With the progress of technology, there are only minor refinements to the traditional combustion concepts. HCCI, incorporating the best features of both SI and compression ignition (CI), is one of the most important refinements. HCCI is an alternative piston-engine combustion process that can provide efficiencies as high as D.I. Diesel engines, while producing low NO_x and smoke emissions. The basic principle of HCCI is forming a homogenous mixture before auto-ignition and starting the combustion volumetrically throughout the cylinder as it is compressed by the piston. Therefore, the diffusion combustion phase can be eliminated and emissions can be greatly reduced.

The theoretical and practical roots of the HCCI combustion concepts are ultimately credited to Nikolai Semenov and his colleagues, who began pioneering work in the field of ignition and built up the thermal and chemical ignition theories in the 1930s (Kowalewicz, 1984, Oppenheim, 1984, 1988). The typical two-stage HCCI combustion process is shown schematically in **Fig. 2.4** (Baumgarten, 2006). The first stage of heat release is associated with the low temperature oxidation (LTO) reactions and the second one is the high temperature oxidation (HTO) reactions. The delay between LTO and HTO is attributed to the negative temperature coefficient (NTC) regime. In addition, according to the definition of "mild combustion" proposed by Cavaliere and Mara (2004), HCCI combustion can be considered to belong to this category. They defined it as follows: "A combustion process is named Mild when the inlet temperature of the reactant mixture is higher than mixture self-ignition temperature whereas the maximum allowable temperature increase with respect to inlet temperature during combustion is lower than mixture self-ignition temperature (in Kelvin)".

The first engine study on HCCI combustion was performed by Onishi et al. (1979) in their study of combustion in a two-stroke SI engine. In this new combustion process, referred to as the active thermo-atmospheric combustion (ATAC), it was found

that the combustion occurred spontaneously at multiple points and there was no flame propagation. The air-fuel mixture was uniform and auto-ignition was initiated by the high-temperature residual gas. In the same year, Noguchi et al. (1979) proposed a similar combustion concept, named Toyota-Soken (TS) combustion, in an opposed-piston two-stroke SI engine.

Although HCCI combustion has been studied for many years, the application of the HCCI concept in Diesel engines started only about two decades ago. Early studies of HCCI combustion were mainly focused on SI engines, which were reviewed by Pucher et al. (1996). In this section, concerns focus on the implement of HCCI in Diesel engines. Njat and Foster (1983) demonstrated the feasibility of achieving HCCI combustion in Diesel engines. Due to the low volatility of Diesel fuel, it is more difficult to form a homogeneous charge before auto-ignition. Since an effective mixture formation is crucial for achieving HCCI combustion, in terms of the fuelling method, the measures to achieve HCCI combustion fall into three categories: port injection, early in-cylinder injection, and late in-cylinder injection (Stanglmaier and Roberts, 1999).

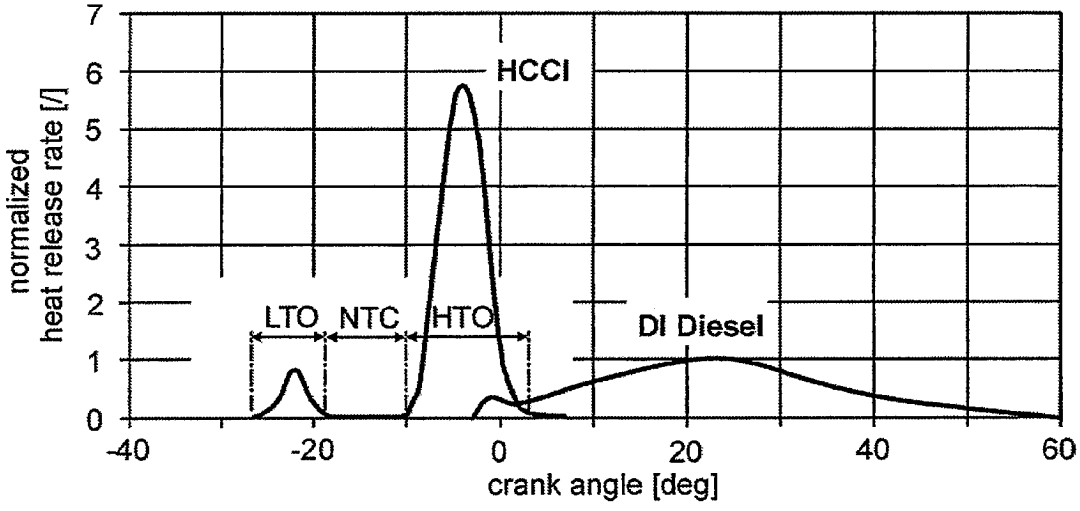

Figure 2.4 Schematic diagram of a two-stage HCCI Diesel combustion process (Baumgarten, 2006)

2.1.2.1 HCCI Combustion Using Port Injection

The simplest way of preparing a homogeneous air-fuel mixture is mixing the air and Diesel fuel during the intake stroke. This method takes advantage of the turbulence generated as the intake flow rushes past the intake valves to promote the mixing process. The air-fuel mixture, however, is exposed to the entire time-temperature history of the cylinder, and thus the start of reaction cannot be controlled by varying the injection timings. The port injection is the most common configuration in HCCI engines, but is mainly attractive for gaseous and liquid fuels with high volatility (Stanglmaier and Roberts, 1999). Only a few research groups carried out the experiments in Diesel engines using this method.

Thomas W. Ryan III and coworkers (Ryan III and Callahan, 1996, Gray III and Ryan III, 1997) in Southwest Research Institute conducted the experiments on HCCI combustion using a port injection strategy in Diesel engines. A specially designed single-cylinder research engine was employed. Since the high boiling point of Diesel fuel required very high air and surface temperature, the intake air was supplied using an external compressor and an air conditioning system which made it possible to control the intake manifold pressure and temperature. The EGR rate was controlled by adjusting the engine back-pressure to create the appropriate pressure differential. In their studies, various parameters, including the compression ratio, inlet temperature, and air-fuel ratio were tested to determine the range of operating conditions for HCCI combustion using Diesel fuel. Soot and NO_x emissions were found to be reduced significantly, whereas the HC emission was twice of that from the conventional D.I. Diesel engines. At the same time, the indicated specific fuel consumption (ISFC) value for HCCI mode was higher than that for D.I. Diesel engines with the similar power output. In their recent studies, the important fuel properties essential for HCCI combustion was identified (Ryan III and Matheaus, 2003), effects of various engine variables were summarized (Ryan III et al., 2004), and potentials of HCCI combustion were compared to the advanced gasoline and Diesel engines (Amann et al., 2006). In comparison to SI and CI engines, the HCCI

engine generally operated with higher HC and CO emissions, though with near zero NO_x emission. In regard to the vehicle certification test cycles, it was recognized that the fuel economy of the HCCI engine was slightly higher for the EPA combined test cycle but comparable with the other engine concepts on the Japan 10-15 test cycle.

A research group at Lund University also conducted a series of experiments on HCCI combustion using the port injection. An in-line six-cylinder heavy-duty Diesel engine was converted to operate in the HCCI combustion mode. Supercharging was employed to increase the indicated mean effective pressure (IMEP). The highest attainable IMEP was 14 bar using natural gas as fuel, which was achieved under the conditions of a boost pressure of 2 bar and a compression ratio of 17:1 (Christensen et al., 1998). Their investigation of the effect the fuel properties on engine variables and emissions demonstrated the feasibility of using different fuel in HCCI engines and showed that NO_x emission did not increase much with increasing fuel octane number and compression ratio (Christensen et al., 1999). Therefore, a dual-fuel port injection system was developed to achieve HCCI combustion and a variable geometry turbine (VGT) turbocharger was employed to obtain the adequate boost pressure regardless of the engine load (Wilhelmsson et al., 2007). In 2008, a new injection system combining the port injection and direct injection was proposed for dual-fuel HCCI operation (Ekholm et al., 2008). Ethanol fuel was premixed with the intake air during the intake stroke and Diesel fuel is directly injected into the cylinder. The experimental results showed that it was possible to reach the IMEP of 18.4 bar which was comparable with the conventional Diesel engine.

Although the port injection prepares more homogeneous air-fuel mixture, the requirements of preheating, difficulties in the control of start of reaction, and relatively poor atomization and vaporization greatly inhibit the practical applications of this method in commercial Diesel engines. Most of the applicable techniques are based on the in-cylinder direct injection strategies as in the conventional D.I. Diesel engines.

2.1.2.2 HCCI Combustion Using Early In-Cylinder Direct Injection

There are different kinds of direct injection strategies to implement HCCI combustion concept in Diesel engines. Two most important ones are the early in-cylinder injection and late in-cylinder injection.

Takeda et al. (1996) proposed the premixed lean Diesel combustion (PREDIC) system. In their study, the fuel injection timing was advanced greatly to promote fuel and air mixing. Two side injectors were adopted to avoid the collision of the fuel spray with the cylinder liner. In addition, to further avoid the wall impingement, a nozzle tip with more holes and smaller diameters was adopted and another injector was located in the center of the cylinder head to execute the main injection after the early premixed injection. It was reported that, NO_x emission decreased greatly due to the homogenous air-fuel mixture, whereas the total hydrocarbons (THC) and CO emission increased obviously because the mixture at the quench areas was too lean to be burned. Since the operating conditions of PREDIC were limited at low load, MULDIC (MULtiple stage DIesel Combustion) (Hashizume et al., 1998) was proposed to extend the operating condition to the high-load region. In this system, the first stage was PREDIC combustion and the second stage was diffusion combustion under the conditions of high temperatures and low oxygen concentration. Further improvements on the PREDIC system were reported later (Akagawa et al., 1999, Nishijima et al., 2001). A newly designed pintle-type injector was adopted to reduce the spray tip penetration length, and an impingement spray system with two single-hole side injectors was tested. The split injection pattern was recommended to reduce the THC and CO emissions.

Yokota et al. (1997, 1998) developed a homogeneous charge intelligent multiple injection combustion system (HiMICS) combining the premixed compression ignition combustion concept with the multiple injection strategy. Different multiple injection strategies, including pilot-main, pilot-pilot-main, pilot-main-after, and early-main were tested to clarify the influence on fuel consumption and emissions. The spray umbrella angle was varied to avoid the wall impingement. Results showed that, for the early-

main injection strategy, it was difficult to control the ignition timing. Although the fuel consumption, NO_x and smoke emissions decreased obviously, HC and CO emission increased. Metyl-t-butyl ether (MTBE) blended fuel could improved the combustion characteristics.

Homogeneous charge Diesel combustion (HCDC) system was proposed by Suzuki et al. (Ishii et al., 1997, Suzuki et al., 1997, Suzuki et al., 1998). In HCDC system, fuel was injected into the intake manifold, mixed with the air, and then ignited by small amount of fuel directly injected into the cylinder. NO_x emission was reduced by retarding the in-cylinder direct injection timing, and EGR was used to reduce smoke emission. To obtain higher thermal efficiency, MTBE-blended Diesel fuel was used to retard the ignition timing close to TDC.

Uniform bulky combustion system (UNIBUS) was developed by Toyota (Yanagihara et al., 1996, Hasegawa and Yanagihara, 2003) to achieve the low temperature combustion (LTC) using the double injection technique. The first injection was used as an early injection to enhance the air-fuel mixing process and to initiate LTC. The second injection was used to trigger the ignition of all fuel. It was reported that the ignition of premixed fuel could be controlled by the second injection, and the non-luminous combustion could be achieved using this system. To compare the UNIBUS with port-injection HCCI and in-cylinder single-injection HCCI, the 2-D PLIF measurements of OH and formaldehyde were applied in an optical light-duty Diesel engine (Hildingsson et al., 2005). Results showed that the UNIBUS formed more NO_x emission when compared to the other two HCCI strategies. The cycle-to-cycle variation of UNIBUS was larger than that of in-cylinder single-injection HCCI, but was lower than that of port-injection HCCI.

2.1.2.3 HCCI Combustion Using Late In-Cylinder Direct Injection

As mentioned above, the difficulties of the optimum injection timing control and relatively high HC emissions are two major unsolved problems for the early injection concept. At the same time, injection strategies should be carefully designed to suppress

the increase in the combustion noise at high load (Iwabuchi et al., 1999, Okude et al., 2004). Therefore, the late in-cylinder direct injection concept was proposed and investigated by Kimura et al. (1999, 2001). In their studies, a concept, named modulated kinetics (MK), was developed in a small-bore high-speed Diesel engine. The basic concept of MK combustion is shown schematically in **Fig. 2.5** (Kimura et al., 2002). Since NO_x formation is strongly dependent on the combustion temperature, the heavy EGR and low compression ratio are effective to reduce NO_x emission. At the same time, reducing the oxygen concentration increases the smoke emission in the conventional diffusion combustion phase. Therefore, special measures should be employed to achieve the premixed combustion. The retarded fuel injection timing and a low compression ratio are adopted to prolong the ignition delay, and thus ensured the homogenous mixture preparation prior to ignition. However, the retarded injection timing and low compression ratio may result in a decrease in thermal efficiency and in an increase in HC emission. The combustion chamber shape should be carefully designed and a high swirl ratio should be employed to suppress HC and soluble organic fraction (SOF) formation and to reduce the cooling losses from the hot burning gas to the chamber walls. Several attractive benefits are associated with the adoption of this combustion concept: the fuel injection equipment (FIE) and combustion chamber are those of a typical Diesel combustion system, ignition timing is controlled by the fuel injection event, and low NO_x and smoke emissions can be obtained simultaneously. To investigate the degree of initial premixing, the influence of the intake temperature, injection pressure, and flow swirl on combustion and emission formation processes was investigated by Choi et al. (2005). In their study, the MK combustion was viewed as "a high-EGR, retarded-injection calibration of conventional Diesel combustion, rather than a predominantly pre-mixed HCCI-like combustion process". It was stated that it was difficult to obtain a real homogenous charge in D.I. Diesel engines using the late injection.

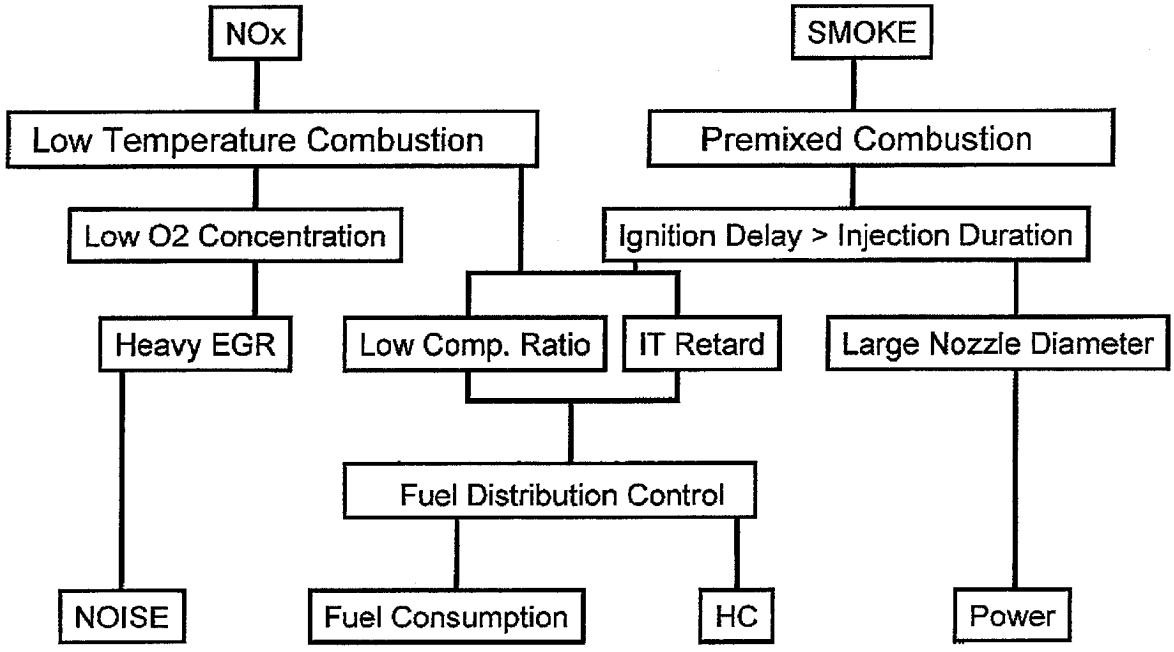

Figure 2.5 Basic concept of MK combustion (Kimura et al., 2002)

Another HCCI combustion concept using the late direct injection was proposed by Shimazaki et al. (2003). A narrow injection angle (27.5 deg. from horizontal) and a shallow dish combustion chamber were used in their studies. By increasing the turbulent mixing rate through increasing the injection pressure, a lean fuel-air mixture can be formed even with the injection timing around -26 deg.ATDC. In their study, low cetane number (CN) fuel (CN = 19) was used to achieve the premixed compression ignition (PCI) combustion with the fuel injection timing near to TDC. To apply this concept to the conventional Diesel fuel, Minato et al. (2005) employed an ultra-high injection pressure (P_{inj} = 240 MPa) and a micro-hole nozzle (d = 0.08 mm) to increase the turbulent mixing rate. The injection timing of indicating extremely low NO_x emission level was -38 deg.ATDC using the commercial Diesel fuel of Japan (JIS#2, CN = 62). In their later studies, a reentrant type combustion chamber and a low compression ratio piston were employed to expand the operation range of PCI combustion using supercharging (Kitabatake et al., 2007). At the same time, the application of this concept in multi-cylinder D.I. Diesel engines was tested (Ishikawa et al., 2007). Engine test results showed that an EGR rate of 55% was required to maintain the NO_x emission

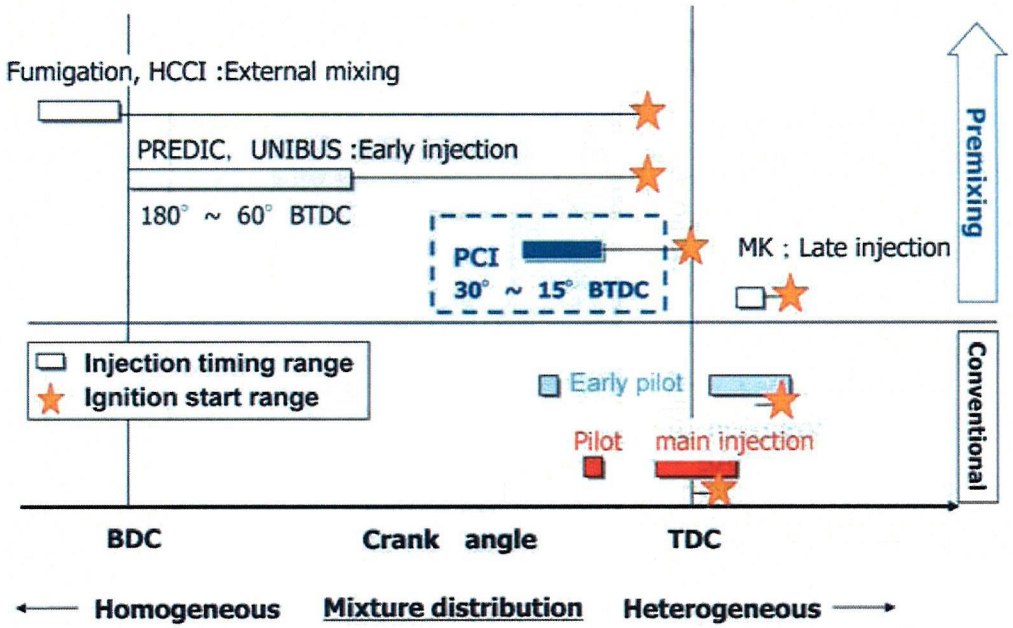

Figure 2.6 Classification of combustion modes in terms of injection timing (Shimazaki et al., 2007)

of 20-30 ppm. High cooling efficiency was essential for the EGR system. According to the computational analysis using KIVA II, the slight increase in THC was caused by the increase in the area of the low temperature region.

A summary of various approaches to achieve HCCI-like combustion is given in **Fig. 2.6** (Shimazaki et al., 2007). Approaches to implement HCCI combustion in Diesel engines include the port injection, early injection, and late injection. It is evident that the direct injection strategy is expected to become the preferred method for HCCI combustion in D.I. Diesel engines in the future (Stanglmaier and Roberts, 1999). Among so many investigations on HCCI combustion in Diesel engines as discussed above, however, only UNIBUS and MK are successfully applied in the commercially available engines, running in HCCI mode over only part of their cycles. As shown in **Fig. 2.7** (Tsujimura et al., 2008), HCCI combustion is only a small domain in the modified ϕ-T map. Since it is difficult to obtain a perfect homogenous air-fuel mixture in D.I. Diesel engines, to improve the engine performance and to expand the operation range, more practical approaches should be developed to meet the future requirement. PCI combustion can prevent a Diesel knocking by retarding the injection

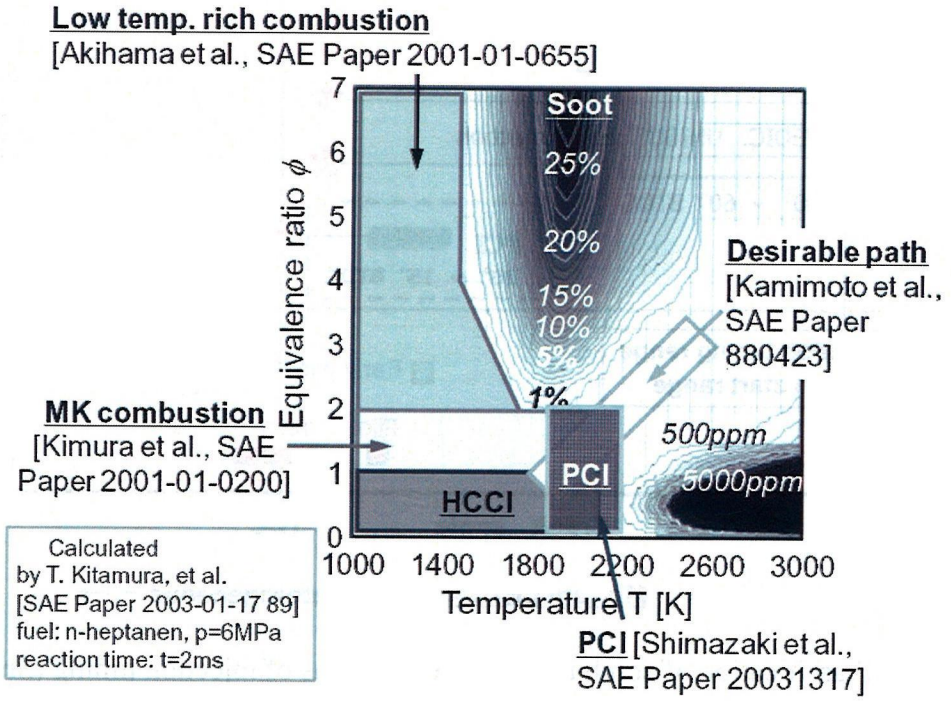

Figure 2.7 Modern combustion concepts in ϕ-T map (Tsujimura et al., 2008)

timing close to TDC. In addition, it is expected to be able to accurately control the ignition timing and to greatly reduce the emissions. However, to achieve this aim, further fundamental research on the mixture preparation, ignition, and combustion processes are required for the successful modeling and engine design.

2.2 SPRAY AND MIXTURE FORMATION PROCESS IN DIESEL ENGINES

2.2.1 Structure of Diesel Sprays

2.2.1.1 Free Spray

The importance of the internal structure of a Diesel spray has been recognized for a long time. The breakup of Diesel sprays and following spray formation have been one of the most debated issues in the Diesel combustion process. Due to the lack of effective experimental method to visualize the internal feature of the Diesel sprays with very high optical density. In the past, the dense core region was thought to have consisted of an intact liquid core. A widely accepted view, as describe in Smallwood and Gulder's excellent review paper (2000), is that the jet breakup was not complete near

the nozzle tip and an intact core existed, extending beyond more than 100 nozzle hole diameters downstream. This view is primarily based on the extrapolation of the information obtained from the pressure-atomized steady liquid sprays at low injection pressures into low-pressure ambient conditions. In the steady pressure-atomized sprays, the dense spray region consists of an intact liquid core, which is similar to the potential core in a single-phase turbulent jet, surrounded by a dispersed-flow region that begins at the nozzle exit (Faeth, 1991, Wu and Faeth, 1993, Faeth et al., 1995). The atomization progresses by primary breakup forming droplets through stripping from boundary layers on the liquid core surface followed by a secondary breakup of ligaments and large droplets. **Figure 2.8** shows a sketch of the near-nozzle region of a pressure-atomized spray for atomization breakup conditions (Faeth, 1987). As the liquid leaves the nozzle,

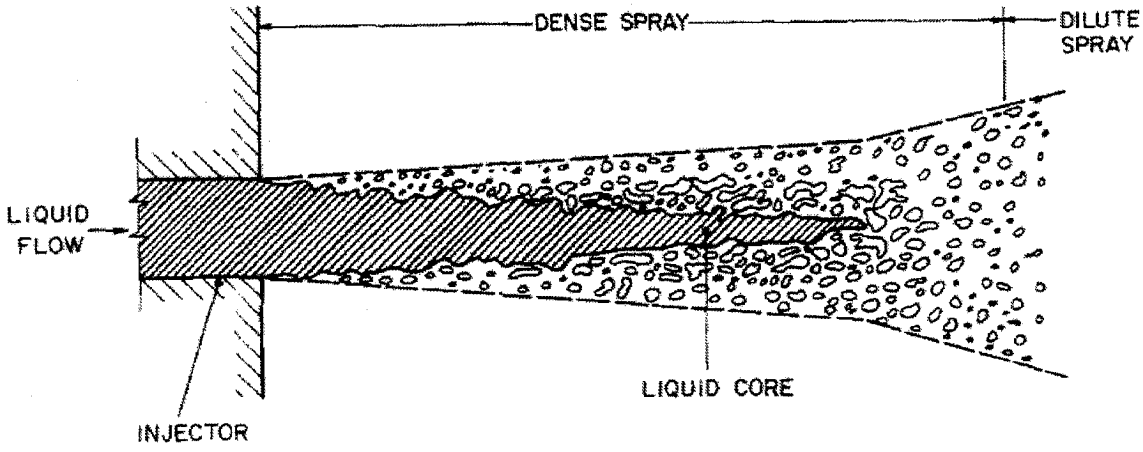

Figure 2.8 Sketch of the near-nozzle region of a pressure-atomized spray for atomization breakup conditions (Faeth, 1987)

it enters a region defined as a churn flow pattern. This region includes the all-liquid core and other irregularly-shaped liquid elements near the axis of the flow. In this region, the liquid elements are rather large and the momentum exchange capabilities of the gas phase are relatively limited due to the small gas density and volume fraction. In analogy with this steady liquid sprays, the transient and intermittent Diesel sprays with high injection pressures were thought to have a similar breakup mechanism. Therefore, the spray process is divided into two regions. The tip of the spray plume moves at an

almost constant velocity during the initial injection period, followed by a sharp transition to decelerating motion. This transition was interpreted to be that from an intact liquid core to an atomized spray.

A lot of research work has been conducted to clarify the structure of Diesel sprays. The structure of non-evaporating Diesel sprays were comprehensively summarized by Hiroyasu and Arai (1990). Four main parameters (breakup length, spray angle, spray tip penetration, and droplet size distribution), as shown in **Fig. 2.9**, were employed to express the structure of a Diesel spray. These four parameters of the spray are related to each other in the disintegrating process and affect the mixture formation through aerodynamic and thermodynamic processes in the combustion chamber of Diesel engines. In their study, they investigated the breakup mechanism using various techniques, including an electric resistance method to measure the breakup length, photographic observations for the spray angle, a photo-transistors array system to measure the progression of the spray, and a laser diffraction method to determine the Sauter mean diameter (SMD) of the spray. The effects of injection velocity, injection pressure, and nozzle geometry on the breakup length, spray angle, and spray tip penetration length were clarified. The detailed breakup mechanism for a hole-type nozzle and its applications were reviewed by Hiroyasu (2000). The observation and phenomenological analysis of the behavior of the internal flow and the disintegration of the liquid jet demonstrates that the strong turbulence in the nozzle hole due to cavitation greatly contributes to the breakup of the liquid jet.

Based on the recent experimental studies, Smallwood and Gulder (2000) summarized the view of the breakup and structure of D.I. Diesel sprays as follows: A small quantity of poorly atomized liquid is injected initially. This produces a relatively large, contiguous, and low-velocity fuel mass, which is subsequently atomized by the highly disruptive cavitating flow. The cavitating flow dominates the injection period, producing small droplets until the needle closing, at which point a few relatively large droplets may emerge from the nozzle.

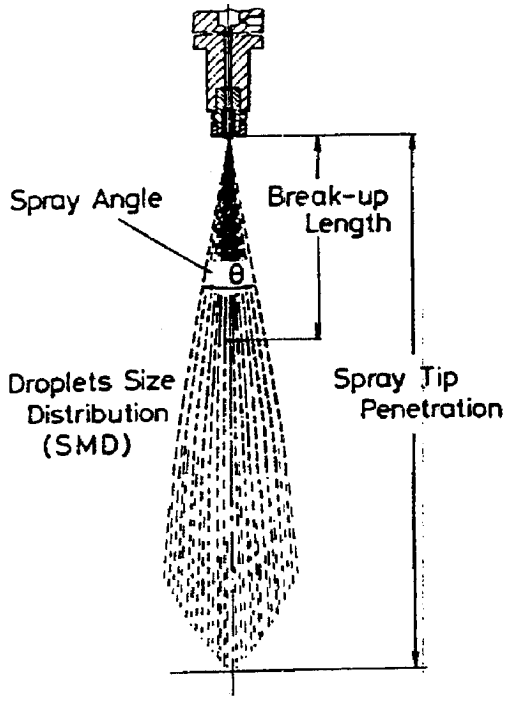

Figure 2.9 Main Parameters of a Diesel Spray (Hiroyasu and Arai, 1990)

However, previous attempts using optical techniques, including schlieren, Mie scattering, and PLIF, to provide information about the internal structure of Diesel sprays have been unsuccessful due to the very dense region of the spray near the nozzle exit (Chigier, 2006). The major breakthrough has recently been achieved at the U.S. Argonne National Laboratory using very high energy x-ray radiography (Yue et al., 2001, MacPhee et al., 2002, Tanner et al., 2006). Their results show that the maximum liquid volume fractions in the near nozzle region (< 500 μm), are between 0.6 and 0.7, clear evidence that liquid breakup and air entrainment occur very close to the nozzle exit, where there is instantaneous atomization. In addition, the spray tip penetration was found not to be linear with the injection time within the first 20 mm from the nozzle. In the downstream area, Hiroyasu's model fits the x-ray absorption data reasonably well.

2.2.2.2 Impinging Spray

Spray/wall interactions occur if a spray penetrating into a gaseous atmosphere impacts a wall. **Figure 2.10** shows the schematic structure of an impinging full-cone

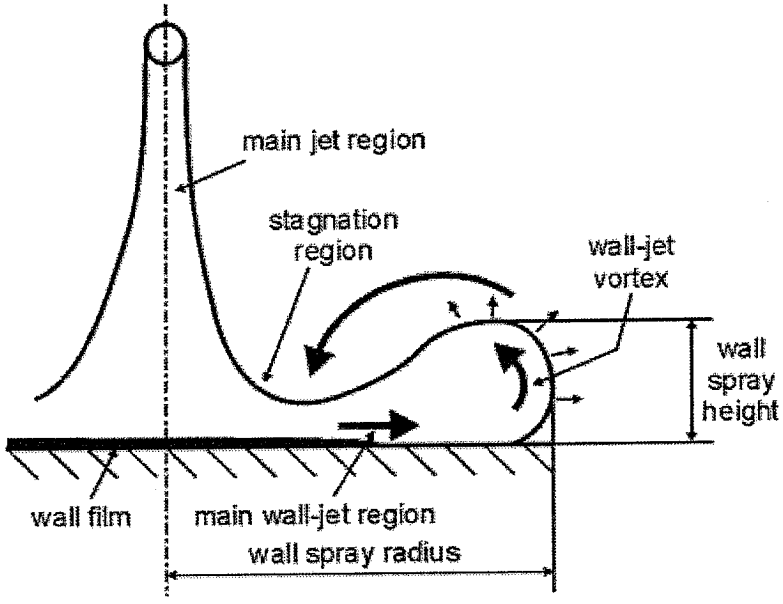

Figure 2.10 Schematic illustration of an impinging full-cone spray (Baumgarten, 2006)

spray (Baumgarten, 2006). Two main physical processes can be involved: wall-spray development and wall film evolution. Whether the wall impingement occurs or not depends on the spray tip penetration length and on the distance between the nozzle tip and wall. Depending on wall temperature and on the amount of fuel film, the spray/wall interactions can have both negative and positive effects. Liquid fuel impinging on a wall at low temperatures will significantly increase the unburned HC and soot emissions due to the slow evaporation of fuel film. However, the impingement may intensify the droplet disintegration and large-scale gas vertex close to the wall may enhance the air entrainment and mixture formation. In addition, a hot wall may intensify the fuel evaporation.

To determine the effect of spray/wall interactions on mixture formation and emission characteristics, fundamental understanding of drop/wall interactions is required. As reviewed by Kong (2007), outcomes of drop/wall interactions vary and depend on the surface conditions and impact energy, i.e., drop Weber, Reynolds, and Ohnesorge numbers. Possible outcomes include stick, rebound with or without breakup, wall jet, spread, film formation, splashing, and inducing droplet breakup by interactions with an existing fuel film. **Figure 2.11** shows the possible hydrodynamic and heat transfer

regimes of drop/wall interactions based on the Weber number and surface temperatures (Kong, 2007).

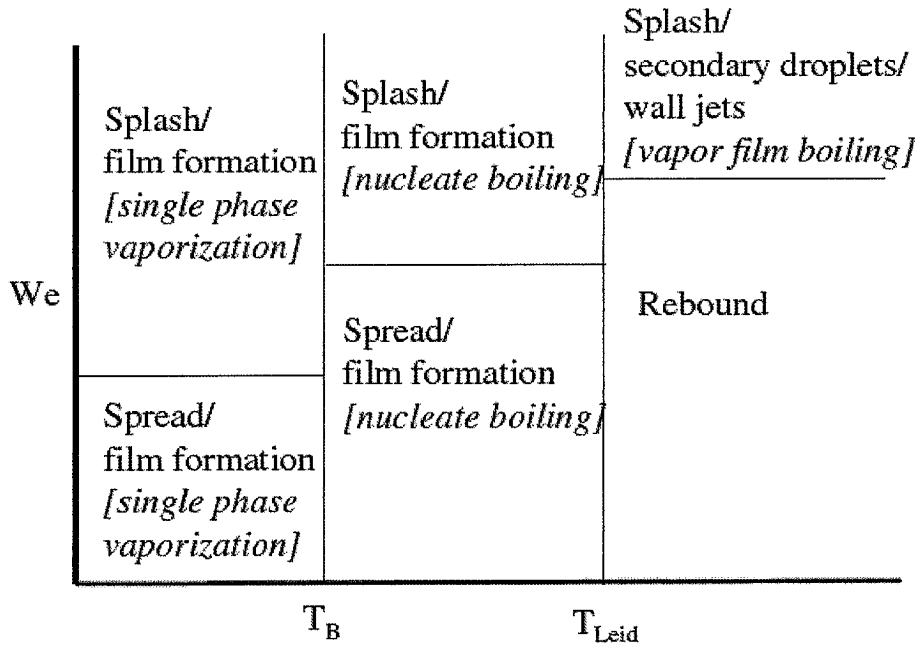

Figure 2.11 Possible drop/wall interaction regimes (Kong, 2007)

In small-bore high-speed D.I. Diesel engines, information on the spray/wall interactions is essential to understand the detailed mechanism and to verify the spray and combustion models in engine simulations. Many experimental studies have been carried out to provide qualitative and quantitative data. Mathews et al. (2003) presented a fundamental set of spray impingement and film evolution data with the detailed information. Ko and Arai (2002a, b, c, d) investigated Diesel sprays impinging on a flat wall, measured the spray volume, adhered fuel film, and proposed an empirical equation for the spray tip penetration length.

2.2.2 Effects of Injection Pressure and Nozzle Hole Diameter

As discussed previously, increasing the injection pressure and decreasing the nozzle hole diameter are effective approaches to improve combustion and emission formation processes in Diesel engines. In this section, effects of these two parameters on the spray and mixture formation process will be reviewed.

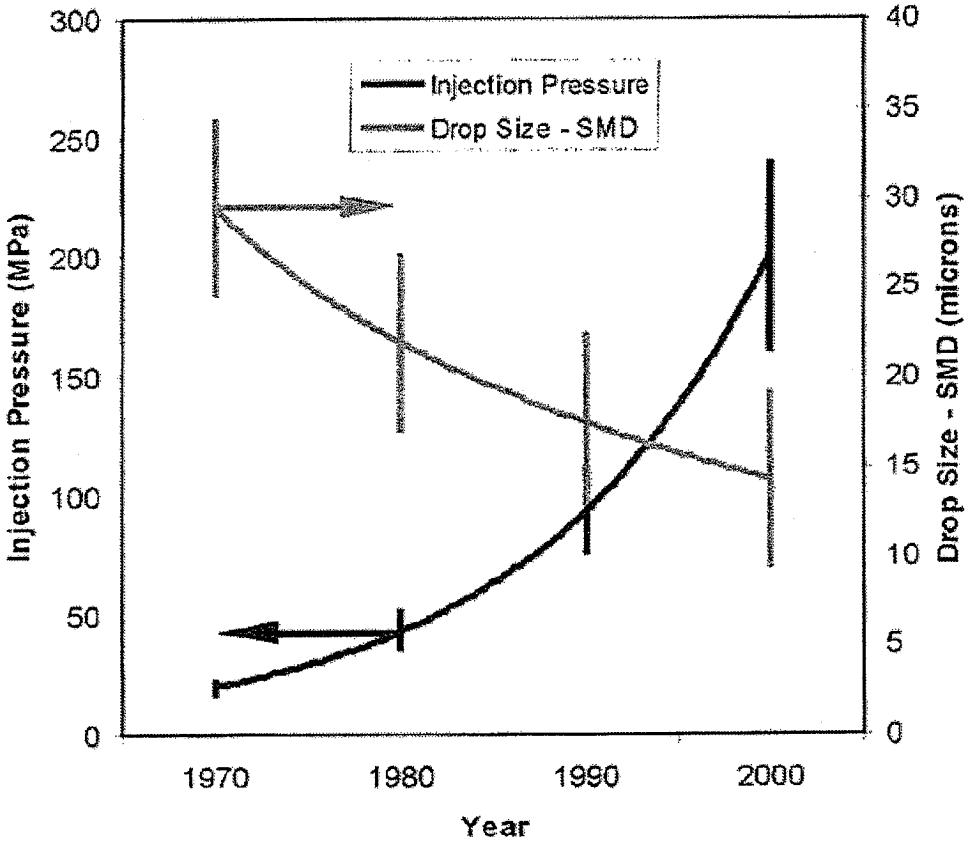

Figure 2.12 Increase in injection pressure and related decrease in SMD in commercially available Diesel engines (Smallwood and Gulder, 2000)

As shown in **Fig. 2.12**, the rapid change in Diesel engine technology has resulted in a dramatic increase in the injection pressure and in a related decrease in SMD. The bars represent the range found in commercially available Diesel engines. High pressure fuel injections are recommended for improving the D.I. Diesel engine performance and reducing PM (Kato et al., 1989, Pierpont and Reitz, 1995, Su and Farrell, 1998, Dodge et al., 2002). An increase in the injection pressure can increase the turbulence intensity due to higher spray momentum, and the small-scale high-intensity turbulence is considered to be effective for atomization, air entrainment, and homogeneous mixture formation (Ikegami, 1990, Molina et al., 2004). In addition, the increased injection pressures usually shorten the time required for the droplet vaporization and combustible mixture preparation and then reduce the ignition delay (Kobori et al., 2000).

At the same time, the nozzle hole diameter is an important variable for planar-orifice nozzles, and a number of droplet size correlations, showing a decrease in droplet size with decreasing the nozzle hole diameter, were summarized by Lefebvre (Lefebvre, 1989). In various published experimental results, Diesel engine emissions are reduced significantly with decreasing nozzle hole size (Montgomery et al., 1996, Bergstrand and Denbratt, 2001, Benajes et al., 2006). In general, this is attributed to finer droplets, shorter spray tip penetration length, and enhanced fuel-air mixing, which result in a homogenous mixture, short ignition delay, and low emissions. Furthermore, in a HCCI engine, since the injection event usually occurs at very low cylinder pressures, micro-hole nozzles offers a chance of getting small SMDs with an acceptable spray tip penetration.

2.3 DIAGNOSTIC TECHNIQUES IN DIESEL ENGINES

2.3.1 Combustion Diagnostic Techniques

Many of the current limitations in understanding the nature of combustion can be attributed to the inability to experimentally probe the combustion processes to the extent essential for empirical and theoretical advances. Combustion processes, whether subsonic or supersonic, are delicately stabilized and easily changed by the physical intrusion. Optical techniques have long been recognized by combustion researchers. Combustion and optical diagnostics have been intertwined since Swan's observation in 1857 of the green bands from C_2 emission in a candle flame. Flames became a good source for optical emission spectroscopy and this early literature is well reviewed in Gaydon's book (1974).

Combustion systems constitute a harsh, high-temperature environment, which often features complex chemistry and a turbulent flow field. In addition, practical combustion often takes place at elevated pressures and in two-phase flows. Experimental determination of the basic information requires significant effort: temperature, concentrations of major species and reactive intermediates, flow velocities, and potential temporal and spatial fluctuations of these quantities must be measured

simultaneously. It is evident that not one single technique will provide all the necessary quantities to characterize a practical combustion process. Many different combustion diagnostic techniques have been developed to meet these demands. The basic physics underlying linear and nonlinear diagnostic techniques used for spatially resolved gas-phase measurements is reviewed by Eckbreth (1996). In his excellent book, the fundamental principles and applications of laser-based combustion diagnostics are treated comprehensively. More recently, Kohse-Hoinghaus and Jeffries (2002) review several optical combustion diagnostic techniques and discuss their applications in various research fields. The combustion diagnostics in engines is summarized by Zhao and Ladammatos (1998b, 2001) in their review paper and book. In this section, the background of combustion diagnostic techniques used in this dissertation will be briefly reviewed, including the imaging of broadband natural flame luminosity and flame chemiluminescence.

2.3.1.1 Experimental Setup for Optical Diagnostics in Diesel Engines

Because of the complexity of the phenomena involved in the Diesel combustion process, detailed investigations using optical diagnostics are applied on three types of experimental setup. High temperature and pressure constant volume vessel, employed in the research work of this dissertation, are used to investigate the auto-ignition and flame structure in originally quiescent gases. In simplified optical research engines, the interaction of injection and combustion can be characterized with a well-controlled flow and thermodynamic conditions. Finally, in converted engines with the geometry and compression ratio similar to those of real engines, the effect of the actual combination of all engine operation parameters can be studies.

As shown **Fig. 2.13**, one excellent example of experimental setups for engine diagnostics is developed by U.S. Sandia National Laboratories (Espey and Dec, 1993, Musculus, 2006). They employ multiple laser-based and/or imaging diagnostics, including laser-elastic (Mie) scattering for the liquid fuel penetration, OH-PLIF, Fuel-

PLIF, ignition chemiluminescence imaging, soot luminosity, and planar laser-induced incandescence (PLII).

2.3.1.2 Broadband Natural Flame Luminosity

Natural flame luminosity imaging without any band-pass filters is a rather common and powerful technique to study the flame structure and ignition characteristics. Direct photography of the natural flame luminosity has been widely used in the field of engine diagnostics. Natural luminosity is usually recorded as a 2-D image. However, unlike the laser-sheet techniques, the light forming the luminosity image is not from a single plane. Rather, it arises from a 3-D source and is integrated over the line of sight in the third dimension. In highly sooting flames like those of Diesel engines, the natural luminosity is dominated by gray body emission from combustion-heated soot, with the intensity of the luminosity from any point in the plume being a function of a local soot volume fraction and the temperature. The contribution of luminous soot at various depths along the line of sight to the natural luminosity image depends on the soot concentration in the combusting plume. For high soot concentrations, only luminous soot on or near the surface of the plume will reach the camera, while for lower concentrations luminous soot throughout the plume will contribute to the flame luminosity image (Dec, 1992, Dec and Espey, 1995).

To take advantage of the luminous nature, the two-color method has been developed and used to measure the temperature distribution and soot concentration in Diesel engines (Matsui et al., 1979, 1982). The detailed principle and applications of the two-color method are comprehensively reviewed by Zhao and Ladommatos (1998b) and are out of the scope of this dissertation.

Natural flame luminosity is also used to investigate the auto-ignition in Diesel engines. When imaging with a moderate light sensitivity, the first bright spots of light appear quite early, and during injection. In general, there are many auto-ignition points, and their locations are a function of injection, fuel, and ambient conditions. The

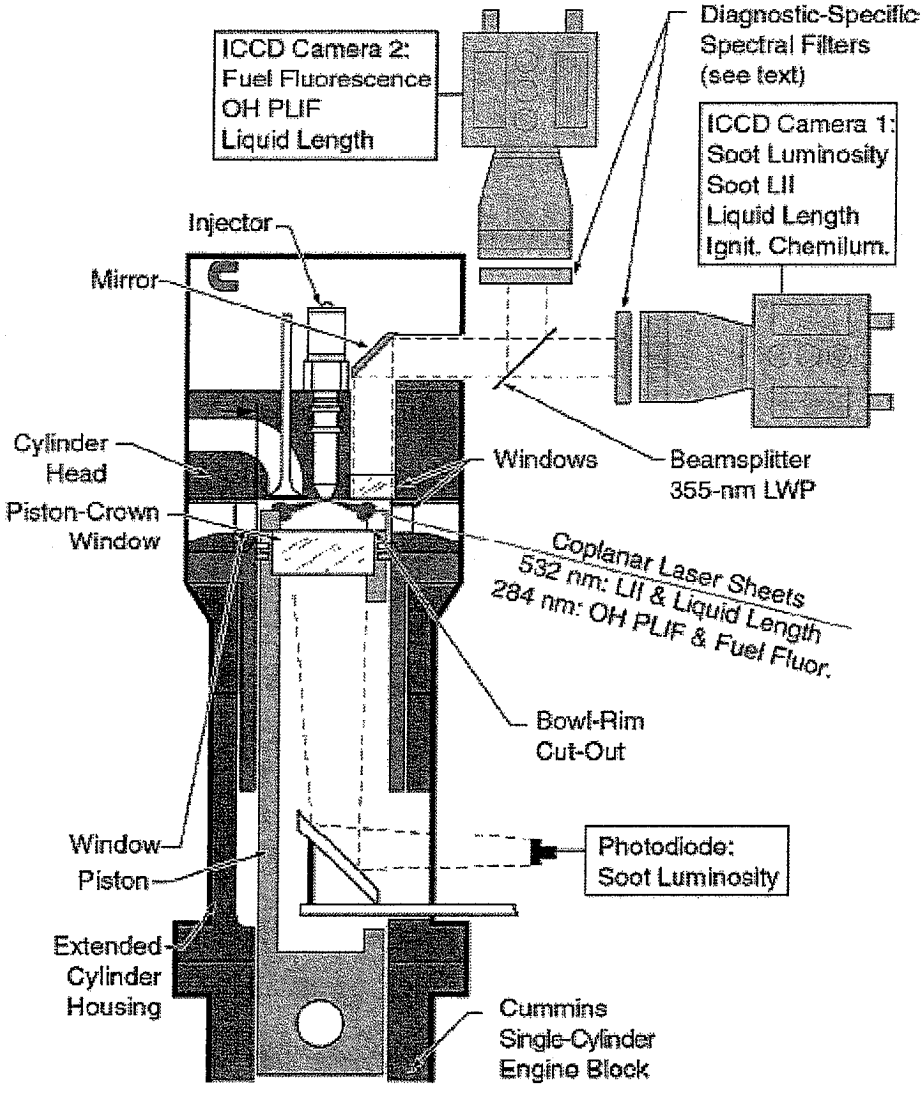

Figure 2.13 Schematic diagram of the optically accessible D.I. Diesel engine and optical setup in U.S. Sandia National Laboratories (Musculus, 2006)

visualization of auto-ignition and its statistical location probability has been observed by Baritaud et al. (1994).

Recently, Mueller and Martin (2002) have proposed a broadband natural luminosity imaging technique to visualize the combustion process and to yield estimates of relative in-cylinder soot volume fractions. The two primary components of the natural luminosity signal are broadband thermal radiation from hot soot particles and the spontaneous, non-thermal radiation from gas-phase molecules as they relax from excited

electronic states. The intensifier gain, lens aperture, and exposure time are optimized to use the full dynamic range of the camera under different test conditions.

2.3.1.3 Flame Chemiluminescence

Flame chemiluminescence, an optical signature of the combustion process, has been recognized as an interesting alternative for combustion diagnostics. Its experimental simplicity due to an optically passive nature compared to laser diagnostics is quite attractive for applications in Diesel combustion. In hydrocarbon-air flames, the strongest chemiluminescent intensity peaks are produced by the excited hydroxyl radical (OH*) at 280 to 310 nm and methylidyne radical (CH*) at 431 nm. The primary path for forming CH* is the reaction $C_2+OH \rightarrow CH^*+CO$. Succeeding this process, OH* is produced by the reaction $CH+O_2 \rightarrow CO+OH^*$ (Gaydon, 1974). The CH* concentration increases rapidly to a maximum within the flame and then decays rapidly downstream of the reaction zone where the radiation decay rate is first order. OH* appears mainly in the combustion region where the oxygen exists because its concentration depends on those of CH* and oxygen. The OH* concentration profiles show a similar behavior across the main reaction zone where the CH* concentration is high, while downstream of the reaction zone the OH* radiation decay rate abruptly slows and becomes second order. Since the reduced decay rate does not occur until the CH* emission has decreased to about 0.5% of their maximum values, it can be concluded that both CH* and OH* show a close correspondence across the main reaction zone and are thus equally suitable as markers for the flame zone location (Schefer, 1997).

The chemiluminescence imaging of CH* and OH* has been widely implemented in Diesel combustion to investigate the cool-flame reaction, auto-ignition, and flame structure (Fujimoto et al., 1994, Dec and Espey, 1998, Higgins et al., 2000, Costa et al., 2005). The spectral features of HCO and CH radicals appear before the start of combustion, whereas typical peaks of the OH radical appear in correspondence to the start of combustion (Costa et al., 2005). Recently, there is growing evidence to suggest that flame lift-off length plays a significant role in D.I. Diesel combustion and emission

Table 1.1 Summary of optical techniques for in-cylinder mixture formation measurement (Zhao and Ladommatos, 1998a)

Technique	Applications	Advantages	Limitations
LRS	Density measurement Vapor concentration	Strong signal Simple setup 2-D imaging	Interference from Mie and spurious scattering Limited to gaseous fuel
SRS	A/F ratio Residual gas fraction	Multi-species detection Multi-point detection Most accurate A/F readings Unaffected by window fouling	Weak signal
LIF	Fuel concentration	Strong red shifted signal 2-D imaging of fuel	Quenching at high pressures Difficult to calibrate
FARLIF	A/F ratio	Direct A/F measurements 2-D imaging	Careful calibration required High pressure operation
LIEF	Fuel vaporization & atomization	2-D imaging Simultaneous detection of vapor and liquid	Quenching by oxygen Only qualitative visualization
LEA (LAS)	Fuel vaporization & atomization	Quantitative concentration measurements Droplet size information	Poor spatial resolution

formation processes. The effect of lift-off length on Diesel combustion occurs as a result of premixing of injected fuel and entrained air upstream of the lift-off length. Siebers and Higgins (2001) have proposed a technique to determine the flame lift-off length of Diesel spray combustion using OH chemiluminescence. OH chemiluminescence is selected for determining lift-off lengths because it is a known to occur under high temperature, stoichiometric combustion conditions (Gaydon, 1974). The energetic reactions and high temperatures that occur during stoichiometric combustion of typical hydrocarbon fuels form excited state species that include OH*. Once formed, OH* returns rapidly to its ground state, a portion through chemiluminescence emission and a portion through collisional quenching. The time

scale for the chemiluminescence emission is on the order of one microsecond. Since the chemiluminescence process is fast compared with transport processes, OH chemiluminescence provides an excellent marker of the high heat release regions where it is generated, such as the stoichiometric combustion region at the lift-off length (Siebers and Higgins, 2001). The band of OH chemiluminescence used to generate the images for determining lift-off is the band near 310 nm, which is one of the strongest bands. This wavelength of light provides the best trade-off between image quality and detectability of the furthest upstream combustion zone in a sooting Diesel spray.

2.3.2 Spray Diagnostic Techniques

To understand the nature of Diesel sprays, a lot of efforts have been made to develop diagnostic techniques and to design well-controlled experiments. As shown in **Table 1.1**, the limitations and advantages of various optical techniques as well as alternatives have been presented in some excellent review papers (Zhao and Ladommatos, 1998a, Smallwood and Gulder, 2000). In this section, several sprays diagnostic techniques, including conductivity, schlieren/shadowgraphy, Mie scattering, x-ray radiography, laser induced exciplex fluorescence (LIEF), and LAS will be briefly reviewed.

2.3.2.1 Conductivity

Some of the earliest insights to the structure of Diesel sprays were provide by measuring the breakup length using the conductivity technique in continuous Diesel sprays (Hiroyasu et al., 1982, Chehroudi et al., 1985, Hiroyasu and Arai, 1990). Conductivity technique is based on the measurement of the electric impedance between the nozzle and a fine wire net detector for continuity. Substitute test fuel was used to provide sufficient conductivity. Although the diesel spray is highly transient, the submodels of Diesel sprays based on the long breakup length measured with conductivity have provided reasonable predictions of the spray tip penetration length in numerical simulations (Yule and Watkins, 1991).

Yule and Salters (1995) applied a new conductivity probe technique to high-speed, pulsed Diesel sprays to measure the dimensions and time dependency of the breakup zone. Breakup length was found to be of the order 100 nozzle diameters at engine-like conditions of gas density. Only 1% of injected fuel was measured to be incompletely atomized 100 nozzle diameters downstream, and the proportion is not linear with distance, as most of fuel was atomized very close to the nozzle exit.

2.3.2.2 Schlieren and Shadowgraphy

Schlieren and shadowgraphy, which were established as visualization tools in the 20th century, are two kinds of earliest available optical diagnostics in experimental fluid mechanics. The history, principles, and applications of these two techniques have been comprehensively summarized by Settles (2001). Due to the high obscuration of Diesel dense sprays, it is recognized that it is difficult to obtain sufficient information related to the internal structure of full-cone transient Diesel sprays using these line-of-sight techniques. However, computers have changed schlieren and shadowgraph techniques in several useful ways. Computational fluid dynamics yields computed schlieren images and shadowgraphs to compare with the experimental kind. Ray-tracing optical design codes make it possible to design much more complex systems. In addition, thanks to the computer for relieving the tedious work of data acquisition and image processing, quantitative schlieren and shadowgraph techniques have staged a comeback.

Recently, in the field of Diesel spray diagnostics, schlieren has been employed to identify the outer boundary of the vapor phase under engine-like conditions (Siebers, 1998). It was reported that the vapor phase would continue to penetrate, whereas the liquid phase penetration would remain constant for fixed conditions.

2.3.2.3 Mie Scattering

Most of current optical diagnostic techniques applied to the fields of drops and sprays are largely based on Mie scattering. It is often used to study the liquid phase penetration, structure of spray plumes, and spray/wall interactions. Bohren and

Huffman (1983) provided a very comprehensive treatment of Mie scattering in their classic textbook.

In the research field of Diesel sprays, the imaging of scattering from sprays has primarily been performed in one of two ways: illumination of the full volume of the spray, or planar sheet illumination for tomographic imaging. Volume imaging of Mie scattering is currently routinely applied to identify the extent of the liquid phase penetration of Diesel sprays (Siebers, 1998). Tomographic imaging has been used to identify the extant nature of the structure of the dense core region in high pressure transient Diesel sprays (Gulder et al., 1992).

The cross-sectional distribution of the fuel vapor concentration in an evaporating spray can be measured quantitatively using a 2-D Mie scattering technique (Kosaka et al., 1992, Kosaka and Kamimoto, 1993). In addition, visualization of the relative locations of the liquid and vapor phases has been performed using dual-intensity Mie scattering (Verhoeven et al., 1998). Weak laser excitation was used in the top region of the spray plumes to visualize the liquid phase. Since a high-boiling-point tracer was added to the Diesel fuel, strong laser excitation was used in the lower region to visualize the scattering from the tracer droplets in the vapor phase. More recently, Bruneaux (2001) combined LIEF with a 2-D Mie scattering technique and measured the distributions of liquid and vapor phases separately.

2.3.1.4 X-Ray Radiography

In recent years there has been a great deal of work performed to use monochromatic x-ray sources, such as synchrotrons, to visualize high-speed Diesel sprays. It is a very promising technique for the dense core measurement because x-rays are minimally scattered by fuel, allowing a direct absorption measurement to be made.

The application of x-ray radiography in Diesel sprays was first investigated by U.S. Argonne National Laboratory (Yue et al., 2001, MacPhee et al., 2002). The x-ray beams are monochromatic, with photon energy of 8keV. The 200 μm × 30 μm x-ray beam illuminates an avalanche photodiode whose output is proportional to the intensity

of the beam. The x-ray absorption data provides an integrated measure of liquid quantity along the length of the path. Signals are recorded every nanosecond, and data are taken at thousands of individual locations in diesel sprays. Measurements begin at 200 μm from the nozzle exit, and measurements cover the full width of the spray at numerous axial locations. X-ray pulses are repeated every 3 μs and there is no significant variability in spray-to-spray injections. The rise in mass density was detected 25 μs after the start of injection.

The most recent results from the Argonne Laboratory show that the maximum liquid volume fractions in the near injector tip region (< 500 μm), are between 0.6 and 0.7, clear evidence that liquid breakup and air entrainment occur very close to the injector exit, where there is instantaneous atomization.

This collaboration among US government high-energy laboratories, industrial diesel injection experts and universities, has provided a new physical description for diesel sprays. Atomization is essentially instantaneous at or very near the nozzle exit. With this physical quantitative description, computational fluid dynamics can provide calculation and predictions which will permit more effective control of direct injection in both diesel and gasoline engines.

2.3.1.5 Laser-Induced Exciplex Fluorescence

Laser-induced exciplex fluorescence (LIEF), originally developed by Melton and Verdieck (Melton and Verdieck, 1985), is a unique technique allowing simultaneous visualization of both liquid and vapor distributions for Diesel sprays. Although elastic scattering, such as Rayleigh and Mie scatterings, can be used to visualize the liquid droplet and fuel vapor at the same time, the signal from the liquid phase normally is much stronger than that from the fuel vapor, which greatly limits the dynamic range of measurements. LIEF technique provides a significant improvement in the dynamic range because the fluorescence from the liquid and vapor phases can be separated in wavelength and detected individually (Zhao and Ladommatos, 1998a). Semi-quantitative information about the fuel sprays, such as relative gas and liquid

concentrations, is available with exciplex fluorescence. Exciplex fluorescence also provides the relative locations of the liquid and vapor phases. The detailed principle and applications of LIEF in Diesel sprays have been summarized by Zhao and Ladommatos (2001).

2.3.1.6 Laser Absorption-Scattering

Although LIEF, as discussed previously, can be used to visualize fuel atomization and vaporization, it is difficult to carry out a reliable quantitative analysis. For instance, the estimation of the absolute liquid phase concentration by LIEF requires detailed information on temperature-dependent spectral emission form exciplex dopants in the spray, which is difficult to implement. Besides, LIEF cannot be used to acquire the droplet size distribution, which is important for describing the spray and mixture formation process.

To meet the requirement of measuring the liquid and vapor phases simultaneously, Chraplyvy (1981) proposed a two-wavelength laser absorption-scattering technique. In this system both laser beams were scattered by the droplets in the sprays, but only the 3.39 μm wavelength was absorbed. The scattering effect of the droplets was removed from the measured transmitted light intensity using a 632 nm laser beam to characterize the light attenuation due to scattering and to measure the droplet size distribution. And then Mie theory was used to predict the total (absorption and scattering) attenuation of the 3.39 μm beam. If the droplet attenuation was removed from the total attenuation, the attenuation caused by vapor phase absorption could be calculated. The authors further assumed that the spray was axisymmetric and then performed a deconvolution on the measured line-of-sight attenuation to obtain the local vapor concentration.

Based on this principle, Suzuki et al. (1993) used 280 nm and 560 nm beams from a dye laser to probe an α-methylnaphthalene spray. The two laser beams were collimated to parallel beams of 100 mm diameter before they passed through a Diesel spray injected into a constant volume vessel at high temperatures and pressures. The

transmitted light beams were then separated into two paths and were detected with two charge-coupled devices (CCD) cameras. Resulting images were digitized on a computer and calculations were then carried out to find the 3-D equivalence ratio distributions of fuel droplets and vapor in Diesel sprays using a computerized tomographic transformation method.

More recently, Zhang et al. (2000, 2001) improved this method and developed a new laser absorption-scattering (LAS) system. Dimethylnaphthalene (DMN), a test fuel of the LAS technique, was used as the simulator of the Diesel fuel. The second harmonic (visible light, 532 nm) and fourth harmonic (UV light, 266 nm) of an neodymium-doped yttrium aluminum garnet (Nd:YAG) laser (Continuum, NY 61-10) were selected as the incident light. The two beams were initially coaxial and were separated into a UV beam and a visible beam by a dichroic mirror. The separated beams were expanded by the respective beam expanders and were made coaxial again using a harmonic separator. Then, the beams were directed to a fuel spray. After being attenuated by the spray, the beams were separated again into two beams by another harmonic separator. The two beams were then focused to the respective CCD cameras (Hamamatsu Photonics, C 4880). The light extinction at the two wavelengths was recorded as 12 bit images by CCD camera chips. The image acquisition and arithmetic processing were carried out by an IPLab (Spectrum Signal Analytics) image analysis system.

In this dissertation, this new LAS system was employed to quantitatively measure the liquid and vapor phases of Diesel sprays from micro-hole nozzles under ultra-high injection pressures.

2.4 SUMMARY

HCCI combustion is a promising combustion mode to reduce PM and NO_x emissions simultaneously. It is not only applicable to CI engines, but also to SI engines. Due to high viscosity and low volatility, it is more difficult for Diesel fuel to form a homogeneous mixture before auto-ignition. Special techniques should be employed to

achieve HCCI combustion in Diesel engines. Since the port fuel injection is too complicated to be implemented in Diesel engines, it is not a practical technique to achieve HCCI combustion mode. In-cylinder direct injection technique is a promising approach to implement HCCI combustion in commercial Diesel engines. Various strategies of in-cylinder direct injection technique has been investigated by researchers. The UNIBUS and MK combustion modes have been successfully applied in production engines. There still are several difficulties for these techniques, including an accurate control of the ignition timing, relatively narrow operation range, and high emissions of HC and CO. In-cylinder late injection technique to achieve PCI combustion near TDC is one of the most promising ways to achieve HCCI-like combustion in commercial Diesel engines. The advanced FIE and electronic control systems have made it possible to prepare a uniform and lean air-fuel mixture close to TDC. The ultra-high injection pressure and multi-micro-hole nozzle are considered to be effective in forming a homogenous mixture and in reducing the mixing time. The understanding of the detailed mechanisms requires the fundamental knowledge of the mixture formation and combustion processes.

The importance of the internal structure of a Diesel spray has been recognized for a long time. Due to the lack of effective experimental method to visualize the internal feature of the Diesel sprays with very high optical density. A widely accepted view is that the jet breakup was not complete near the nozzle tip and an intact core existed, extending beyond more than 100 nozzle hole diameters downstream. This view is primarily based on the extrapolation of the information obtained from the pressure-atomized steady liquid sprays at low injection pressures into low-pressure ambient conditions. In this research field, the major breakthrough has recently been achieved at the U.S. Argonne National Laboratory using very high energy x-ray radiography. Their results show that the liquid breakup and air entrainment occur very close to the nozzle exit, where there is instantaneous atomization. In addition, the spray tip penetration was found not to be linear with injection time within the first 20 mm from the nozzle. In the

downstream area, Hiroyasu's model fits the x-ray absorption data reasonably well. In a small bore D.I. Diesel engine, the spray/wall interaction is a critical issue for the atomization and vaporization. The injection parameters also play an important role in the mixture formation process. The effects of the injection pressure, nozzle hole geometry, ambient conditions have been investigated by researchers. However, the atomization mechanism of the ultra-high injection pressure and micro-hole nozzle has not been studied comprehensively. Fundamental studies are required to clarify the detailed influence on mixture formation and combustion processes.

Diagnostic techniques play important roles in the experimental study on the spray and combustion processes. Natural flame luminosity imaging without any band-pass filters is a rather common and powerful technique to study the flame structure and ignition characteristics. Direct photography of the natural flame luminosity has been widely used in the field of engine diagnostics. Flame chemiluminescence has been recognized as an interesting alternative for combustion diagnostics. Its experimental simplicity due to an optically passive nature compared to laser diagnostics is quite attractive for applications in Diesel combustion. Mie-scattering techniques allow the qualitative measurement of the liquid phase development and spray/wall interactions. LIEF is a useful technique for simultaneous imaging of both liquid and vapor distributions. X-ray radiography is a very promising technique for dense core measurement. LAS is a powerful technique to meet the requirement of quantitatively measuring the liquid and vapor phases simultaneously.

Chapter 3 Experimental Details

3.1 INJECTION SYSTEM

A manually operated piston screw pump, high pressure generator (High Pressure Equipment Co., Model 37-5.75-60), was used to generate the ultra-high injection pressure up to 300 MPa in the common rail. **Figure 3.1** shows the schematic of injection system employed in this research work. All components were connected by special high pressure fittings and tubing. The handle of the high pressure generator was rotated counter-clockwise to draw fuel from the fuel reservoir into the cylinder body of the generator. And then, the inlet valve was closed and the outlet valve was opened. By rotating the handle clockwise, the piston compressed the fuel to develop pressure. After repeating this procedure several times, a pressure of 300 MPa, measured with a pressure transducer, could be obtained in the common rail.

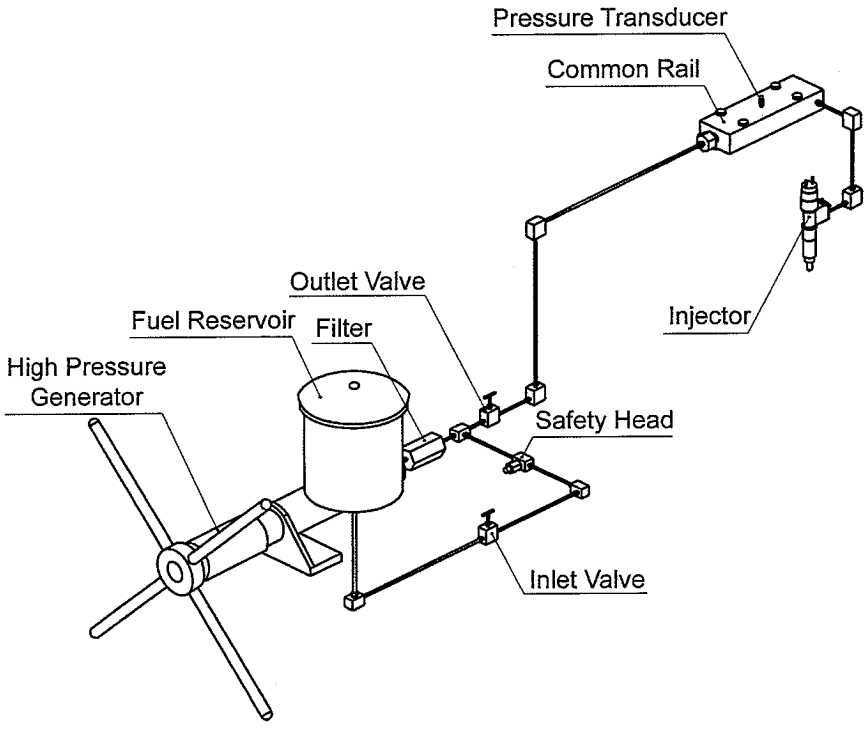

Figure 3.1 Schematic diagram of high pressure injection system

A Diesel injector, electronically controlled by an injector driver, was specially designed to meet the requirement of ultra-high injection pressures. Two pulse generator (Stanford Inc., DG 535) were used to provide the external trigger for the injector driver and to synchronize the Nd:YAG laser, CCD cameras, and injection system. A cross-sectional schematic diagram of the nozzle tip is shown in **Fig. 3.2**. The length of the nozzle hole was 1.2 mm and was held constant for all of test nozzles. The sac volume was 0.488 mm^3. The injection rate was measured with the Bosch long-tube method. **Figure 3.2** shows three injection rate curves versus the time after the end of injection (EOI) at three representative injection pressures.

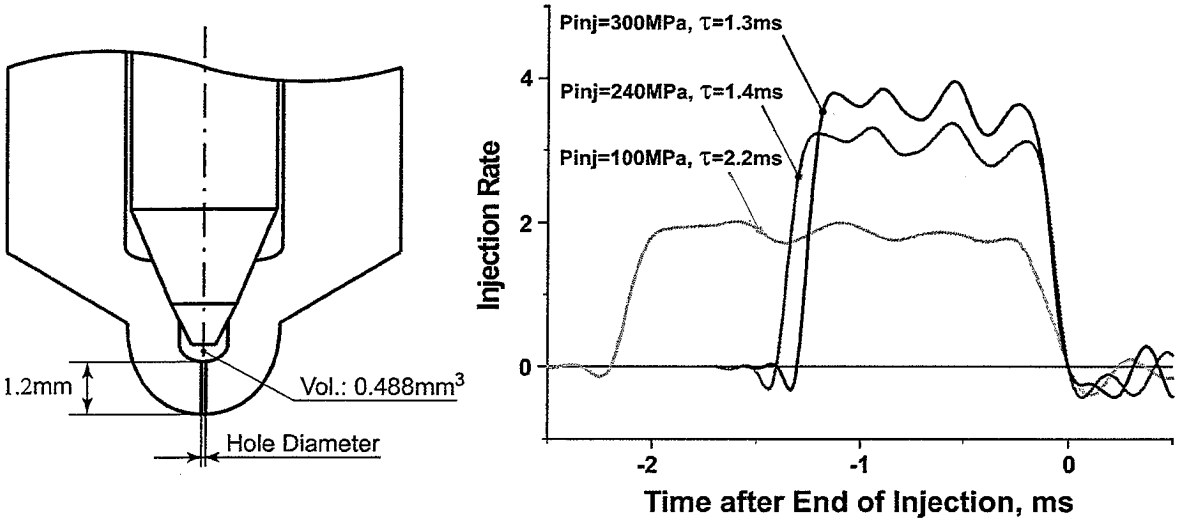

Figure 3.2 Cross-sectional schematic diagram of nozzle tip and injection rate curves

3.2 CONSTANT VOLUME VESSEL

The injector was mounted in a pressure vessel to allow for pressurization of the environment into which the fuel was injected. The constant volume vessel, used in both spray and combustion experiments, is schematically shown in **Fig. 3.3**. The vessel was filled with nitrogen gas and was heated with electrical heaters. To simulate the engine-like conditions, the ambient pressure and temperature could be increased up to 5 MPa and 1000 K respectively. A thermocouple was fixed close to the spray. The temperature distribution was measured under the condition of elevated temperature and atmospheric

pressure. It was found that, at 15 minutes after reaching the desired temperature, the temperature variation was less than 30 K. In addition, the internal surfaces of the vessel were covered with thermal insulators to reduce the heat radiation and loss. Therefore, the ambient temperature distribution was assumed homogenous. Two quartz windows with a diameter of 100 mm were installed to provide enough field of view to visualize the spray and combustion. During the experiments of direct photography of the spray and combustion, one quartz window was replaced by a metal block with a black surface.

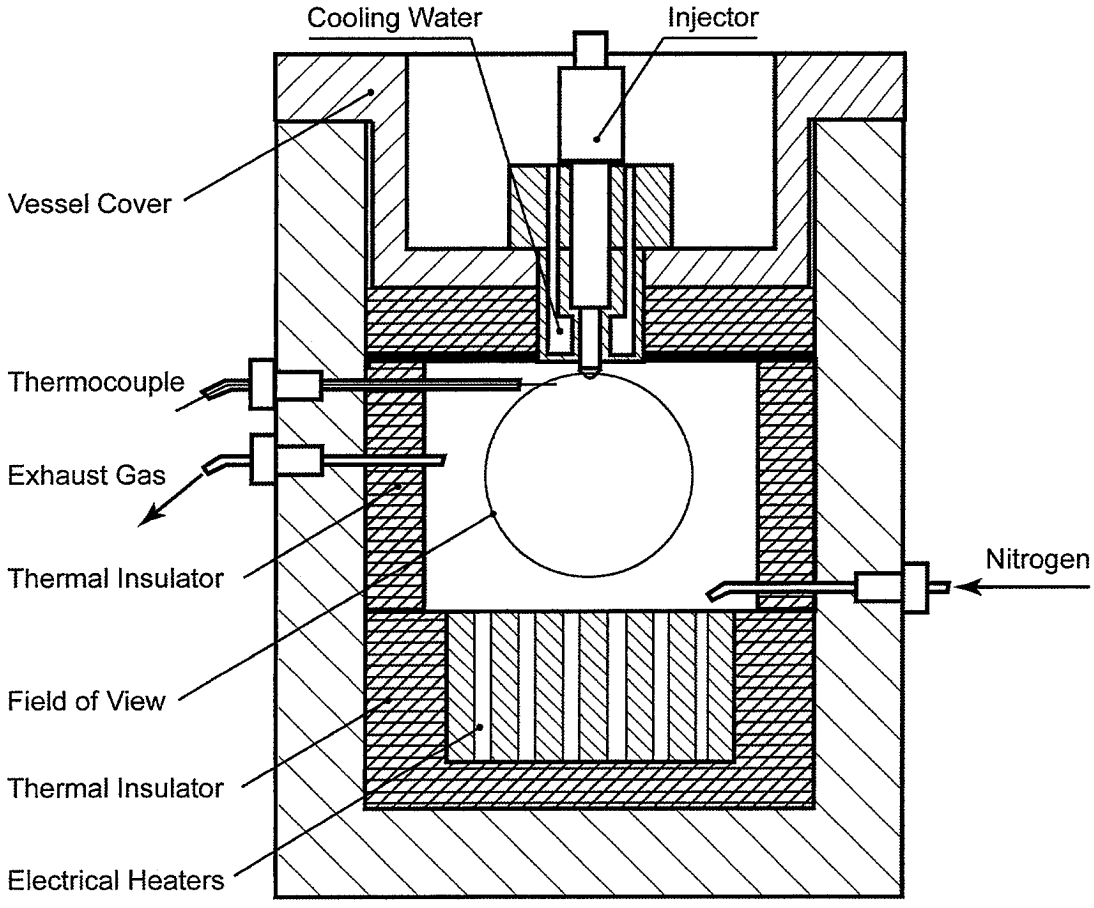

Figure 3.3 Schematic diagram of high-temperature high-pressure constant volume vessel

3.3 DIRECT PHOTOGRAPHY SYSTEM

A high-speed video camera (Photron Co., ultima APX RS) was employed to take the direct photography of sprays and combustion. Utilizing 10-bit CMOS sensor with 17 μm pixels, 16.7 ms to 2 μs global electronic shutter, this camera provided full mega

pixel resolution images at frame rates up to 3,000 frames per second (fps), 512 x 512-pixels resolution at 10,000 fps, and at reduced frame rates to the fastest frame rate of 250,000 fps. DaVis (LaVision Inc., DaVis 7.0) was used for data acquisition and processing.

During the imaging of non-evaporating sprays, as shown in **Fig. 3.4**, a xenon lamp (Ushio Inc., SX-UID 510XAMQ) was used to illuminate the sprays. The xenon lamp provided an effective radiation diameter of 50 mm and an irradiance of 1,200,000 lux with the irradiance uniformity of 70%. A Nikkor visible lens (Nikon, 70-210 mm, f/4-5.6) was mounted. The focus length of about 85 mm and the aperture of f/4 were used for all test conditions.

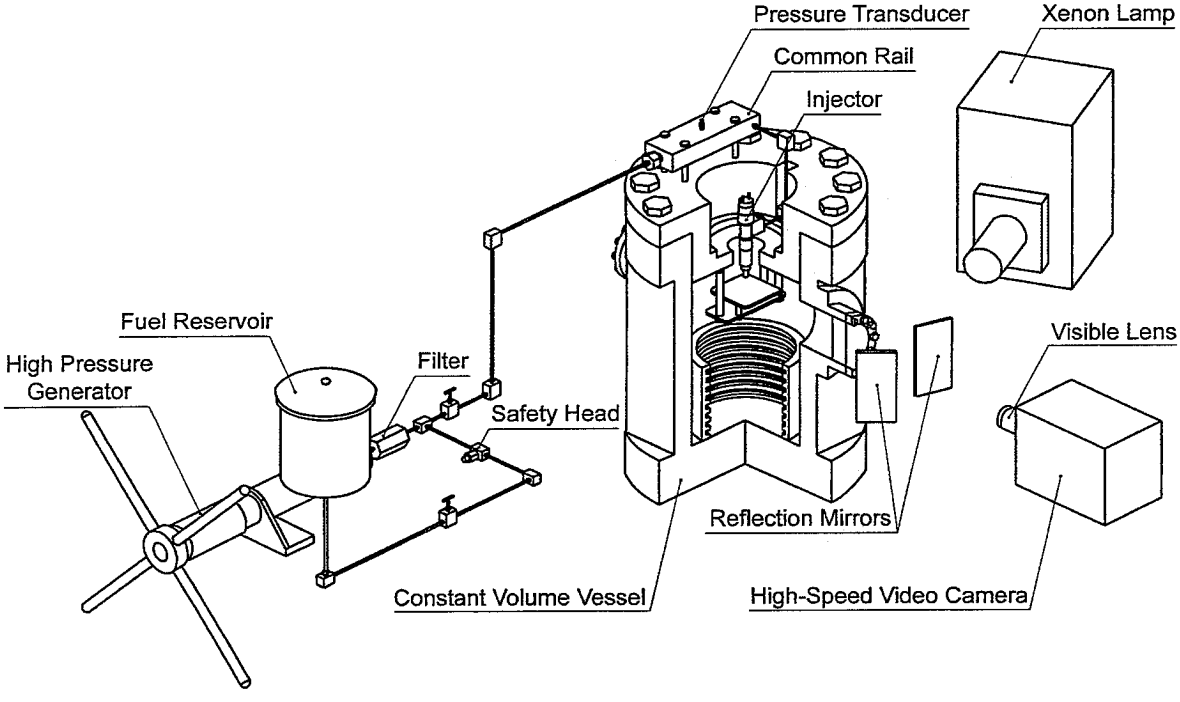

Figure 3.4 Schematic diagram of direct photography system for non-evaporating sprays

During the imaging of spray combustion at elevated pressure and temperature, as shown in **Fig. 3.5**, an image intensifier (LaVision Inc., HS-IRO) was coupled and a UV-Nikkor lens (Nikon, 105 mm, f/4.5) was used to visualize the broadband natural flame luminosity. The gain and gate of the image intensifier were adjusted carefully to acquire

clear flame images. A band-pass filter, centered at 313 nm with 10 nm full width at half maximum (FWHM), was used to visualize the ling-of-sight OH chemiluminescence.

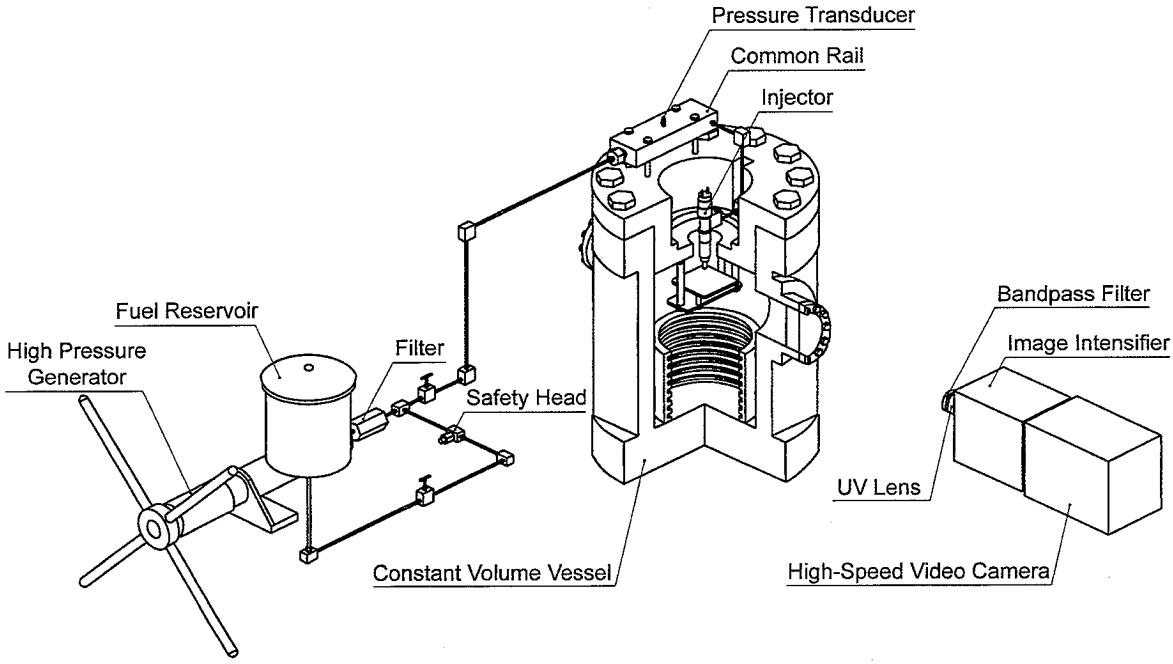

Figure 3.5 Schematic diagram of direct photography system for spray combustion

3.4 LASER ABSORPTION-SCATTERING SYSTEM AND PRINCIPLES

3.4.1 Experimental Setup

Figure 3.6 shows the experimental setup of LAS system. The second harmonic (visible light, 532 nm) and fourth harmonic (UV light, 266 nm) of an Nd:YAG laser (Continuum, NY 61-10) were selected as the incident light. The two beams were initially coaxial and were separated into a UV beam and a visible beam by a dichroic mirror. The separated beams were expanded by the respective beam expanders and were made coaxial again using a harmonic separator. Then, the beams were directed to a fuel spray. After being attenuated by the spray, the beams were separated again into two beams by another harmonic separator. The two beams were then focused to the respective CCD cameras (Hamamatsu Photonics, C 4880). The light extinction at the two wavelengths was recorded as 12 bit images by CCD camera chips. The laser pulse was triggered by the injection pulse through the Q-switch of the Nd:YAG laser. A pulse

generator (Stanford Inc., DG 535) was used to synchronize the Nd:YAG laser, CCD cameras, and injection system. The image acquisition and arithmetic processing were carried out by an IPLab (Spectrum Signal Analytics) image analysis system. To minimize the shot-to-shot variation, the LAS images were determined by averaging four images that were taken at four times under the same conditions.

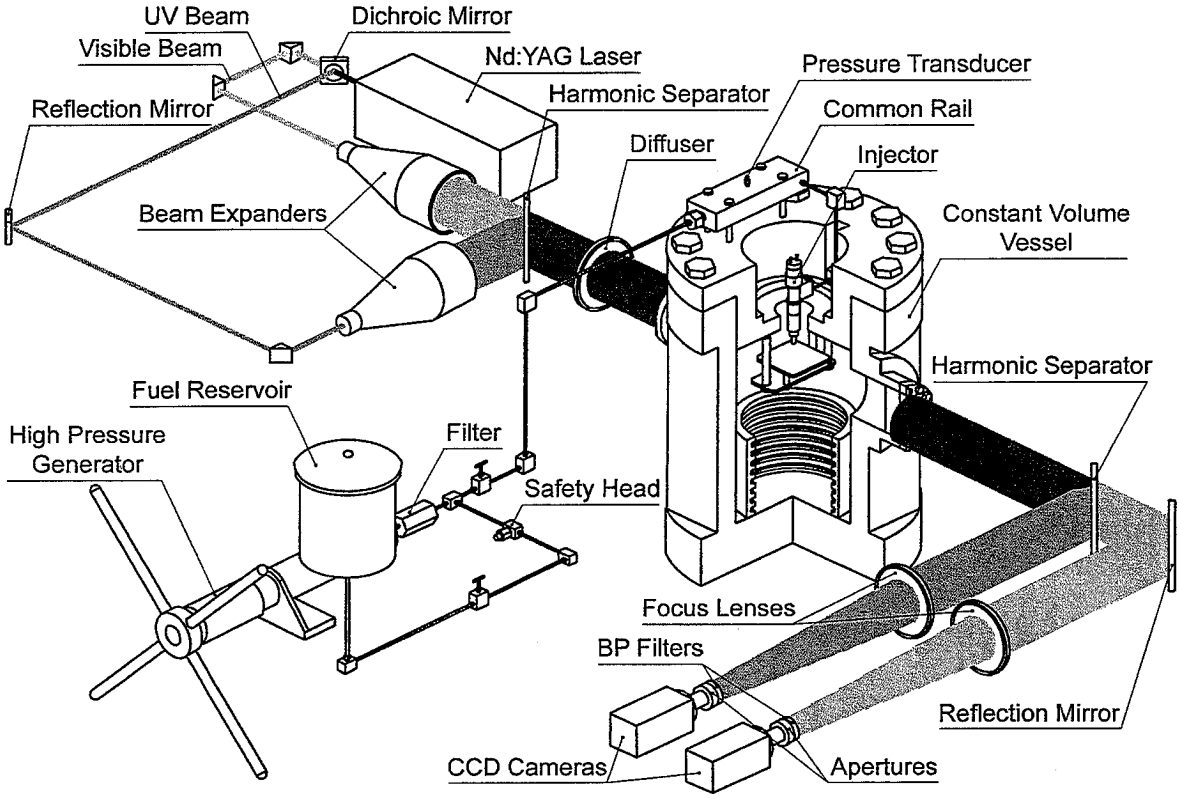

Figure 3.6 Experimental setup of LAS system

3.4.2 Principles of LAS Technique

3.4.2.1 Absorption and Scattering

As shown in **Fig. 3.7**, a two-wavelength (λ_A: absorption wavelength, λ_T: transparent wavelength) incident light of intensity I_0 transmits through a mixture of both vapor and liquid phases, and is attenuated into a transmitted light of intensity I_t. The extinction of the absorption wavelength light is attributed to the liquid phase droplets scattering and absorption as well as the vapor phase absorption, as expressed by **Eq.**

(3.1). The extinction of the transparent wavelength light is only attributed to the liquid phase droplets scattering, as expressed by **Eq. (3.2)**.

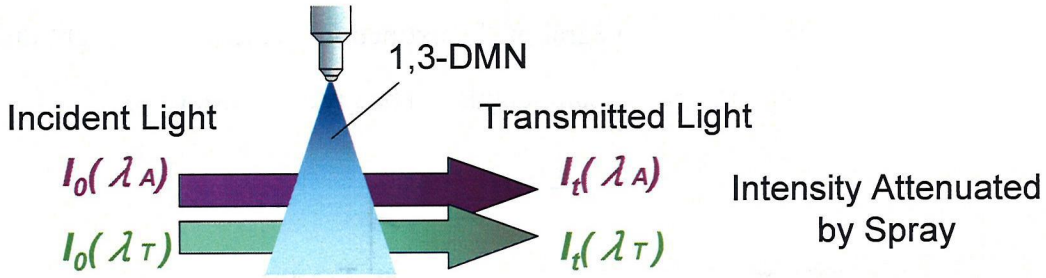

Figure 3.7 Principle of LAS technique

$$\ln\left(\frac{I_0}{I_t}\right)_{\lambda_A} = \ln\left(\frac{I_0}{I_t}\right)_{L_{sca}+L_{abs}} + \ln\left(\frac{I_0}{I_t}\right)_{V_{abs}} \tag{3.1}$$

$$\ln\left(\frac{I_0}{I_t}\right)_{\lambda_T} = \ln\left(\frac{I_0}{I_t}\right)_{L_{sca}} \tag{3.2}$$

If the extinction of the two wavelength lights due to the liquid phase is the same, the extinction by the vapor absorption and liquid scattering can be expressed by **Eqs (3.3)** and **(3.4)** respectively.

$$\ln\left(\frac{I_0}{I_t}\right)_{V_{abs}} = \ln\left(\frac{I_0}{I_t}\right)_{\lambda_A} - \ln\left(\frac{I_0}{I_t}\right)_{\lambda_T} \tag{3.3}$$

$$\ln\left(\frac{I_0}{I_t}\right)_{L_{sca}} = \ln\left(\frac{I_0}{I_t}\right)_{\lambda_T} \tag{3.4}$$

In this study, the second harmonic (visible light, 532 nm) and fourth harmonic (UV light, 266 nm) of an Nd:YAG laser (Continuum, NY 61-10) are selected as the transparent wavelength light and absorption wavelength light. Dimethylnaphthalene (DMN), a test fuel of the LAS technique, was used as the simulator of the Diesel fuel. DMN has similar physical properties as those of Diesel fuel. At the same time, it is a strong UV light absorber and is transparent in visible light. Its absorption coefficient is not strongly dependent on the temperature.

3.4.2.2 Vapor Phase Concentration

As shown in **Fig. 3.8**, the defined filed is assumed to be filled with the fuel vapor. Based on Lambert-Beer's law, the integral of the extinction of the incident light due to the vapor absorption along the optical path length can be given by **Eq. (3.5)**.

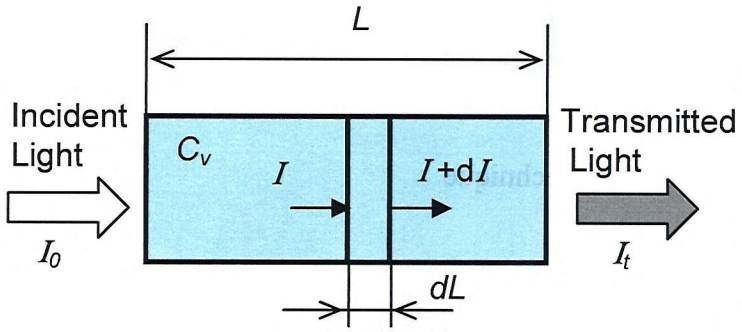

Figure 3.8 Extinction of absorption wavelength light due to vapor absorption

$$\ln\left(\frac{I_0}{I_t}\right)_{V_{abs}} = \int_0^L \alpha dx = \int_0^L \frac{\varepsilon \times 10^2}{MW} \cdot C_v dx \tag{3.5}$$

where L : optical path length, m

α : absorption coefficient, m^2/kg

C_v : vapor mass concentration, kg/m^3

ε : molar absorption coefficient, l/(mol·cm)

MW : mole weight, g/mol

The optical path length L is given from the experimental setup. The extinction can be experimentally determined based on **Eq. (3.3)**. The molar absorption coefficient is a temperature dependent value and will be discussed later. The mole weight depends on the fuel property. If the vapor in the defined field is homogeneous, the vapor mass concentration can be expressed as

$$C_v = \frac{MW \cdot \ln(I_0/I_t)_{V_{abs}}}{\varepsilon \cdot L \times 10^2} \tag{3.6}$$

Furthermore, the equivalence ratio of the vapor concentration is given by

$$\phi_v = \frac{AF_{stoich}}{AF_v} = \frac{AF_{stoich}}{\left(\frac{C_a}{C_v}\right)} \tag{3.7}$$

where AF_{stoich} : stoichiometric air-fuel ratio

AF : actual air-fuel ratio of vapor phase fuel

C_a : ambient gas concentration, kg/m^3

For a hydrocarbon fuel with a formula of C_nH_m, the stoichiometric air-fuel ratio AF_{stoich} can be calculated by **Eq. (3.8)** based on the chemical reaction theory.

$$AF_{stoich} = \frac{137.3 \times \left(n + \frac{m}{4}\right)}{12n + m} \tag{3.8}$$

3.4.2.3 Liquid Phase Concentration

Similarly, a droplet cluster is supposed to be distributed in the defined field. With neglecting the multiple scattering, the transparent incident light of intensity I_0 is attenuated to the transmitted light of intensity I_t only by the droplet scattering. Accordingly, the extinction of the light is given by

$$\ln\left(\frac{I_0}{I_t}\right)_{\lambda_T} = \int_0^L K_{ext}\, dx \tag{3.9}$$

where K_{ext}, the extinction coefficient, is defined as

$$K_{ext} = \frac{\pi D^2 C_n Q_{ext}}{4} \tag{3.10}$$

where D : droplet diameter, μm

C_n : droplet number density, m^{-3}

Q_{ext} : extinction efficiency

In a Diesel spray, if the droplets, assumed to be approximately spherical, are poly-dispersed, K_{ext} can be expressed as

$$K_{ext} = \frac{\pi}{4} C_n \int_0^\infty Q_{ext} N(D) D^2 dD \tag{3.11}$$

where $N(D)$ is the droplet size distribution function, which is normalized by

$$\int_0^\infty N(D)dD = 1 \tag{3.12}$$

Thus, substituting **Eq. (3.11)** into **Eq. (3.9)** gives

$$\ln\left(\frac{I_0}{I_t}\right)_{\lambda_T} = \int_0^L \int_0^\infty \frac{\pi}{4} Q_{ext} C_n N(D) D^2 dD dx \tag{3.13}$$

In **Eq. (3.13)**, the extinction efficiency Q_{ext} can be calculated from Mie theory. For spherical particles, it is dependent on the refractive index and size parameterχ (for a particle with a diameter of D, $\chi = \pi D / \lambda$, λ is the light wavelength). According to the light scattering theory (Kerker, 1969, Van de Hulst, 1981, Bohren and Huffman, 1983), if the particle size is sufficiently larger than the light wavelength, Q_{ext} approaches to a value of 2 regardless of the wavelength. **Figure 3.9** shows the calculated results of the correlation between the droplet diameter and extinction efficiency of two wavelength (266 nm and 532 nm) lights.

Nonetheless, the extinction efficiency Q_{ext} due to the light scattering will be underestimated when the forward scattered light entered into the light receiver, especially in the dense core region of the spray where multiple scattering occurs. A lens-pinhole-receive optical arrangement may be available when the detection half angle is set as narrow as possible. However, for the spray imaging, the excessively narrow half angle will sacrifice the light intensity and may be a big concern. Therefore, it is necessary to introduce a correction factor R_k for the calibration of the extinction efficiency. It has been shown that the correction factor R_k is dependent on the size parameter χ and detection half angle θ. For a small θ and a large χ, R_k can be calculated based on Rayleigh's approximate diffraction theory (Gumprecht and Sliepcevich, 1953). **Figure 3.10** shows the calculated results.

According to the above discussion, **Eq. (3.13)** can be rewritten as

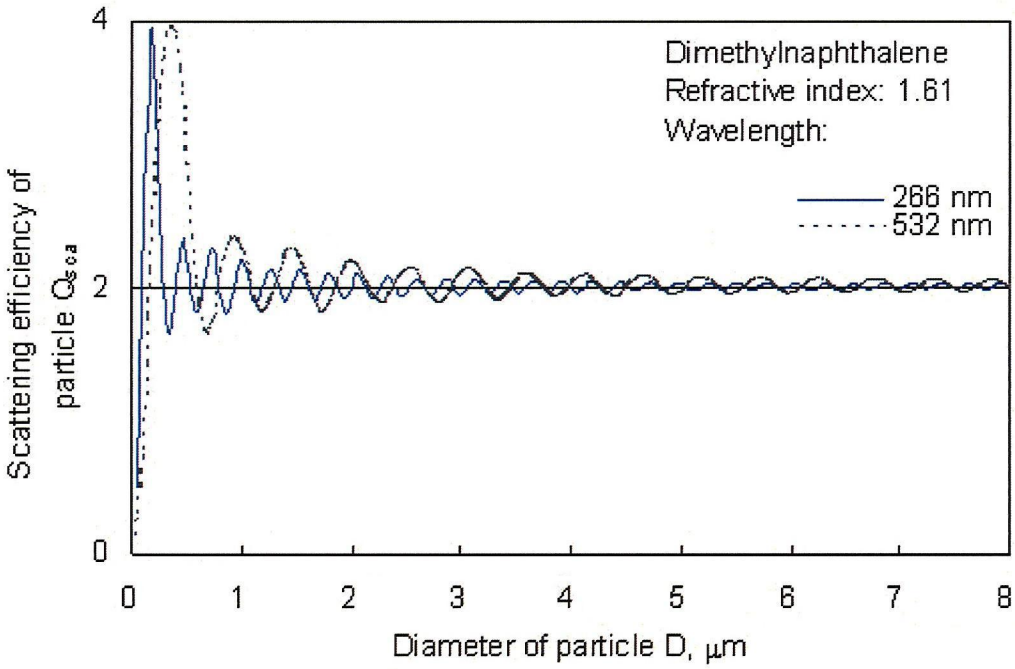

Figure 3.9 Extinction efficiency by a DMN droplets at the fixed wavelengths of 266 nm and 532 nm (Calculated by approximation equation of H. C. Van de Hulst)

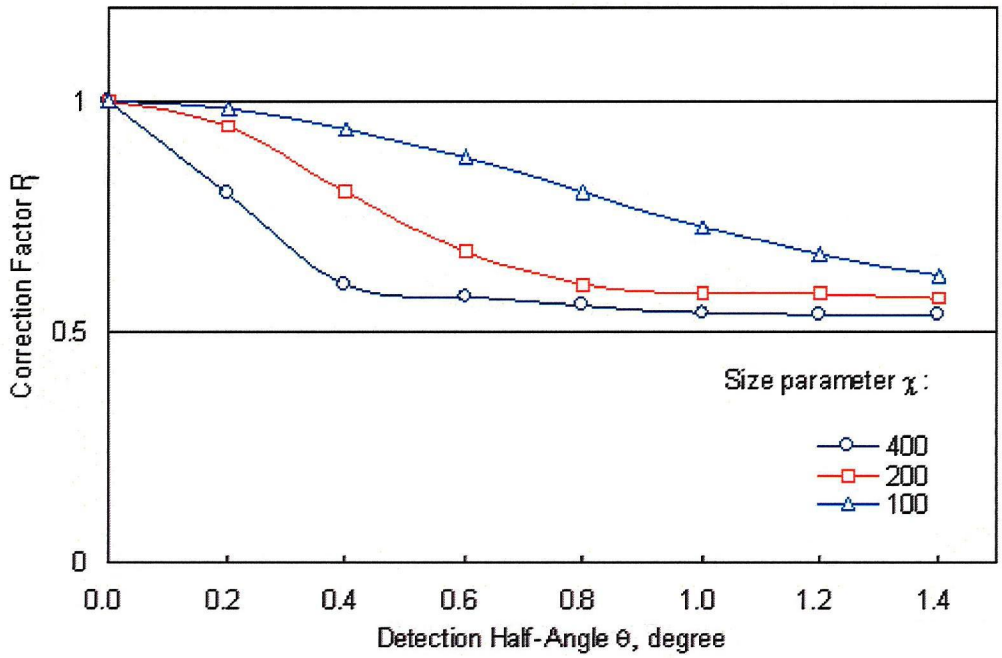

Figure 3.10 Correction factor for extinction efficiency Q_{ext} due to liquid droplets (Gumprecht and Sliepcevich, 1953)

$$\ln\left(\frac{I_0}{I_t}\right)_{\lambda_T} = R_k Q_{ext} \int_0^L \int_0^\infty \frac{\pi}{4} C_n N(D) D^2 dD dx \tag{3.14}$$

The concentration of the liquid phase fuel C_d is given by

$$C_l = \frac{1}{L} \int_0^L \int_0^\infty \frac{\pi}{6} \rho_f D^3 C_n N(D) dD dx \tag{3.15}$$

Suppose that SMD D_{32} represents the droplet diameter of the whole spray, combining Eq. (4.14) and the definition of D_{32}

$$D_{32} = \frac{\int_0^\infty D^3 C_n N(D) dD}{\int_0^\infty D^2 C_n N(D) dD} \tag{3.16}$$

Then **Eq. (4.15)** can be rewritten as

$$C_l = \frac{2}{3} \rho_f D_{32} \frac{1}{L} \int_0^L \int_0^\infty \frac{\pi}{4} D^2 C_n N(D) dD dx = \frac{2}{3} \rho_f D_{32} \frac{\ln\left(\frac{I_0}{I_t}\right)_{\lambda_T}}{R_k Q_{ext} L} \tag{3.17}$$

In this study, D_{32}, related to the total mass of the liquid phase fuel M_l and the summation of the optical thickness over the entire spray, is approximately determined using the light extinction method (Kamimoto et al., 1989).

$$D_{32} = \frac{3}{2} \cdot \frac{R_k Q_{ext} M_l}{\rho_f \sum_S \ln\left(\frac{I_0}{I_t}\right)_{\lambda_T} \Delta S} \tag{3.18}$$

where S : projected area over the entire spray, m^2

ΔS : unit projected area, m^2

Therefore, the equivalence ratio of the liquid phase fuel ϕ_l can be expressed as

$$\phi_l = \frac{AF_{stoich}}{AF_l} = \frac{AF_{stoich}}{\frac{C_a}{C_l} - \frac{C_a}{\rho_f}} \tag{3.19}$$

where AF_l is the air-fuel ratio of the liquid phase fuel.

3.4.2.4 Deconvolution of line-of-sight measurement results

Since the derived concentration or equivalence ratio is a line-of-sight value, to obtain the spatial distributions, a scheme for the deconvolution of the line-of-sight value should be proposed. For an axisymmetric spray, onion-peeling model can be adopted to perform the deconvolution (Hammond Jr., 1981). As shown in **Fig. 3.11**, the cross-section of the spray is presumably comprised of a series of concentric rings. If the area of each ring is sufficiently small, the concentration in each ring can be considered to be homogenous. Based on **Eq. (3.5)**, the extinction due to the vapor phase absorption in the first ring can be expressed as

$$\ln\left(\frac{I_0}{I_1}\right)_{\lambda_A} = \varepsilon\times 10^2 \cdot \frac{C_v(1)}{MW}\cdot l_{1,1} \tag{3.20}$$

Accordingly, the vapor concentration $C_v(1)$ in the first ring can be obtained. In the second ring, the extinction of the vapor phase absorption can be expressed as

$$\ln\left(\frac{I_0}{I_2}\right)_{\lambda_A} = \frac{\varepsilon\times 10^2}{MW}\cdot\left(C_v(1)\cdot l_{2,1} + C_v(2)\cdot l_{2,2}\right) \tag{3.21}$$

Then, the $C_v(2)$ is resolvable. Similarly, the extinction due to the vapor absorption in the i-th ring can be obtained. Thus the vapor phase concentration in the i-th ring can be derived as

$$C_v(i) = \frac{1}{l_{i,i}}\left[\frac{MW}{\varepsilon\times 10^2}\left\{\ln\left(\frac{I_0}{I_t}\right)_{\lambda_A} - \ln\left(\frac{I_0}{I_t}\right)_{\lambda_T}\right\} - \sum_{k}^{i-1}\left(C_v(k)\cdot l_{i,k}\right)\right],\ i = 1,2,\ldots \tag{3.22}$$

Using the same method, the concentration of the liquid phase fuel can be derived as

$$C_l(i) = \frac{1}{l_{i,i}}\left\{\frac{2\rho_f D_{32}}{3R_k Q_{ext}}\cdot\ln\left(\frac{I_0}{I_t}\right)_{\lambda_T} - \sum_{k}^{i-1}\left(C_l(k)\cdot l_{i,k}\right)\right\} \tag{3.23}$$

Thus the local concentration of both liquid and vapor phases can be obtained.

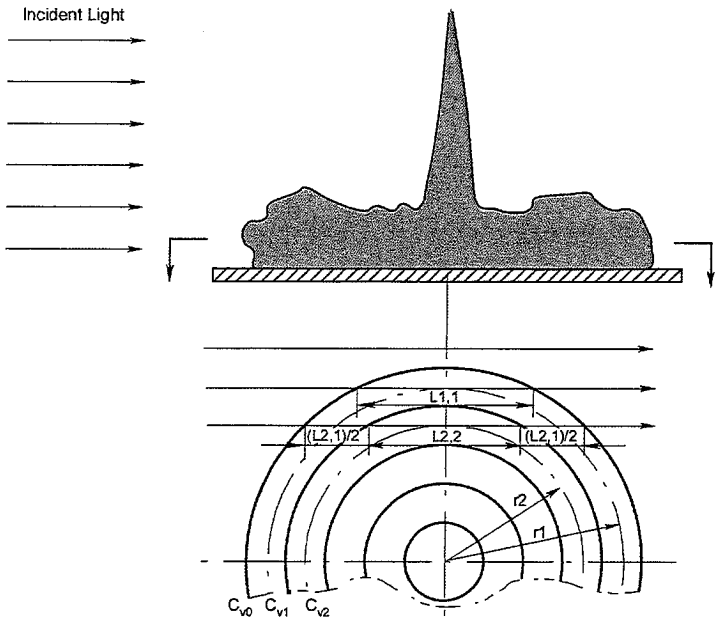

Figure 3.11 Onion-peeling model for LAS deconvolution

3.4.2.5 Temperature distribution

Due to the heat and mass transfer occurring in the evaporating spray plume, the temperature in the air-fuel mixture is spatially different. In **Eqs (3.7)** and **(3.19)**, the air concentration C_a should be determined for the calculations of ϕ_v and ϕ_l. The air concentration is dependent on the local temperature. Nevertheless, the molar absorption coefficient in **Eq. (3.6)** is a temperature-dependent variable as well. Consequently, the information about the spatial temperature distribution in the mixture is necessary for the LAS measurement.

Unfortunately, the measurement of temperature distribution in a transient evaporating spray is quite difficult. So far, no reliable methods can provide the accurate information about both temperature and concentration distributions simultaneously. Therefore, a model for the local temperature calculation is employed and it is schematically illustrated in **Fig. 3.12**. With the assumption of an axisymmetric spray, the cross-section of the spray is assumed to be comprised of a series of concentric rings. In the *i*-th ring, the enthalpy conservation gives

$$C_v(i)(T_{mix}(i)\cdot c_{pv} - T_{l0}\cdot c_{pl}) + C_v(i)\cdot H = C_a(i)\cdot c_{pa}\cdot(T_{ent}(i) - T_{mix}(i)) \tag{3.24}$$

where c_{pv} : specific heat of fuel vapor at constant pressure, kJ/(kg·K)

c_{pl} : specific heat of liquid fuel at constant pressure, kJ/(kg·K)

c_{pa} : specific heat of ambient air at constant pressure, kJ/(kg·K)

H : potential heat of vaporization of fuel, kJ/kg

T_{l0} : initial temperature of liquid fuel, K

$T_{mix(i)}$: temperature of mixture, K

$T_{ent(i)}$: temperature of entrained gas, K

Thus, the mixture temperature of the i-th ring can be obtained as

$$T_{mix}(i) = \frac{C_v(i)(c_{pv}\cdot T_{l0} - H) + C_a(i)\cdot c_{pa}\cdot T_{ent}(i)}{C_v(i)\cdot c_{pv} + C_a(i)\cdot c_{pa}} \tag{3.25}$$

The vapor concentration $C_{v(i)}$ is deconvoluted from the experimental results. The thermodynamic parameters depend on the fuel properties and can be determined from the empirical equations (Poling et al., 2001). The entrained gas temperature is defined by

$$T_{ent}(i) = \frac{T_a + T_{mix}(i-1)}{2},\ T_{mix}(0) = T_a,\ i = 1,2,... \tag{3.26}$$

where T_a is the temperature of the ambient gas.

When an initial temperature of the mixture $T_{mix}(i)$ is proposed, the local ambient gas concentration $C_a(i)$ can be obtained. Thus, using the iteration algorithm, the local temperature $T_{mix}(i)$ can be finally determined.

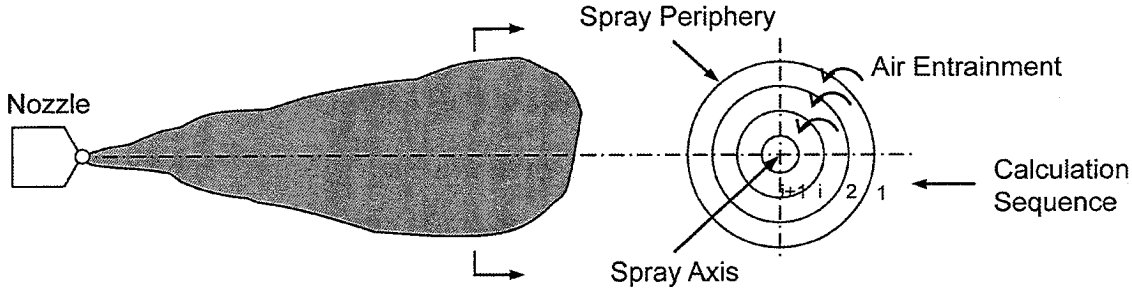

Figure 3.12 Model for temperature calculation in an evaporating spray

3.4.2.6 Selection of test fuel

Since the accuracy and sensitivity of LAS system are greatly influenced by the fuel properties, it is vital to find a test fuel to simulate the Diesel fuel. The test fuel must have the following properties:

(1) Suitable physical properties, including boiling point, viscosity, and evaporation characteristics, which are similar to those of Diesel fuel;

(2) Strong absorption at one wavelength of the dual-wavelength incident light, but slight absorption at another one;

(3) Suitable optical absorption characteristics, such as a temperature dependence of the absorption coefficient.

According to the above criteria, an investigation has been made of the absorption spectra characteristics of a number of fuels in the hydrocarbon and naphthalene-family. **Table 3.1** lists these test fuels and their physical properties (Thermodynamics Research Center, 1982). The absorption spectra of the liquid candidate fuels were measured using an ultraviolet-visible spectrophotometer (Shimadzu Co., UV-3000) with a 190~1200 nm bandwidth. The results, as shown in **Fig. 3.13**, indicate that 1,3-DMN and α-MN greatly absorb the ultraviolet light but are almost transparent for the visible light. Moreover, 1,3-DMN is the strongest ultraviolet light absorber in the group. **Figure 3.14** shows the evaporation characteristics of 1,3-DMN, α-MN, and Diesel fuel. It indicates that evaporating rate of 1,3-DMN is close to that of Diesel fuel at the test conditions. So far, 1,3-DMN was selected as the test fuel of the LAS technique to measure both vapor and liquid concentrations in a Diesel spray.

Zhang (2001) has investigated the effects of the ambient temperature and pressure on the absorption properties of 1,3-DMN, as shown in **Fig. 3.15**. His results show that the absorbance decreases with increasing the ambient temperature and pressure. Note that the peak absorption wavelength barely changes with varying the temperature and pressure. To obtain the absorption coefficient of 1,3-DMN at 266 nm, the absorbance measurement at different ambient temperatures and pressures was conducted. The

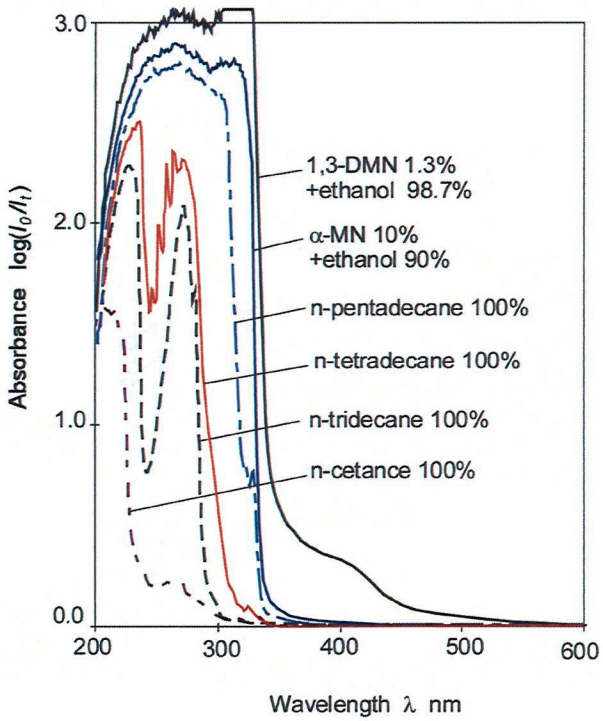

Figure 3.13 Absorption spectra of liquid fuels with physical properties similar to those of Diesel fuel. Ethanol was employed as a solvent to dilute 1, 3-DMN and α-MN to avoid exceeding the measurement range of the instrument.

Table 3.1 Properties of candidate test fuels (Thermodynamics Research Center, 1982)

Substance	Diesel JIS #2	n-Tridecane $C_{13}H_{28}$	n-Tetradecane $C_{14}H_{30}$	n-Penta-decane $C_{15}H_{32}$	n-Cetane $C_{16}H_{32}$	1,3-Dimethyl-naphthalene $C_{10}H_6(CH_3)_2$	α-Methyl-naphthalene $C_{10}H_7(CH_3)$
Boiling point ℃ (1 atm.)	~273	235	253.7	270.6	287.0	265.2	244.7
Density kg/m^3 (20°C, 1 atm.)	~830	756	760	770	780	1018	1016
Kinetic viscosity (10^{-6})m^2/s (20°C, 1 atm.)	~3.86	2.47	3.04	3.73	4.52	3.95	2.58
Refractive index in visible light (20°C, 1 atm.)						1.6102	1.6419
Molecular structure						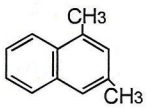	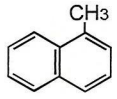

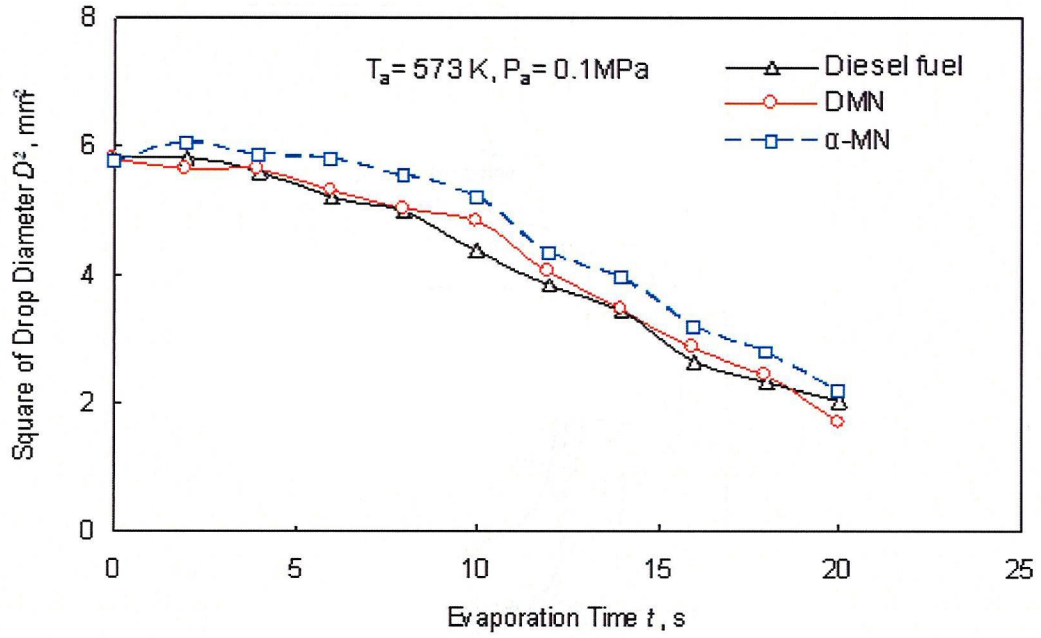

Figure 3.14 Evaporation characteristics of 1,3-DMN, α-MN and diesel fuel. Ambient temperature T_a = 573 K, ambient pressure P_a = 0.1 MPa

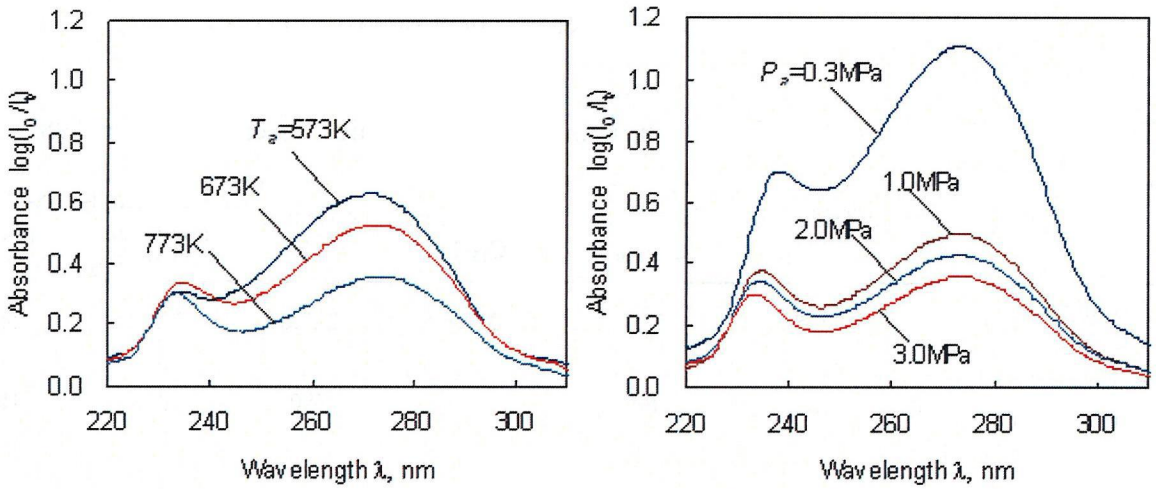

Figure 3.15 Absorption spectra of 1, 3-DMN at various temperatures and pressures. Ambient gas: nitrogen, ambient pressure P_a = 3.0 MPa, vapor concentration C_v = 0.06 mol/m^3, optical path length L = 100 mm.

correlation of the absorbance and vapor mole concentration at 723 K and at various pressures is shown in **Fig. 3.16(a)**. It is found that the correlation is linear over a certain range of absorbance. This linear range increases with increasing the ambient pressure. **Figure 3.16 (b)** shows the correlation of the molar absorption coefficient and absorbance.

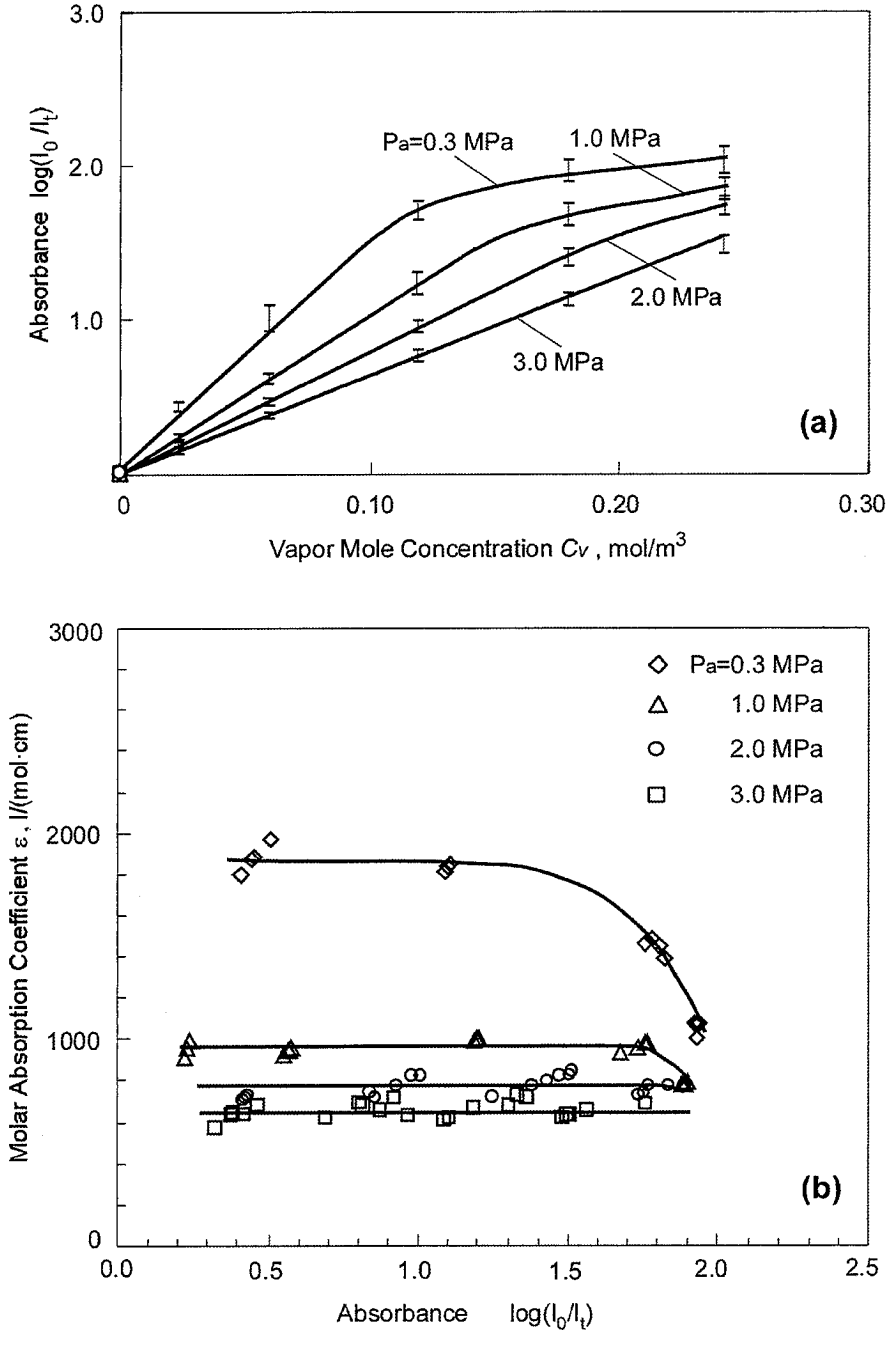

Figure 3.16 1,3-DMN vapor concentration dependence of UV absorption. Ambient gas: nitrogen, ambient temperature T_a = 723 K, wavelength λ= 266 nm, optical path length L = 100 mm. (a) Correlation between absorbance and vapor mole concentration, (b) Correlation between absorption coefficient and absorbance.

It indicates that, within a certain range, the molar absorption coefficient remains constant with increasing the absorbance. The threshold value is about 1.8. It means that, for the ambient conditions employed in this research, Lambert-Beer's law holds true if the

absorbance is lower than 1.8. The detailed discussion on this issue can be found in Zhang's dissertation (2001).

3.4.2.7 Error Analysis

The accuracy of the LAS system has been investigated by previous students in this group using a swirl injector (Zhang, 2001, Li, 2004). It has been found that the error in the vapor concentration increases with increasing the optical thickness. In the region where the vapor phase fuel dominates, the error is estimated to be about 5%.

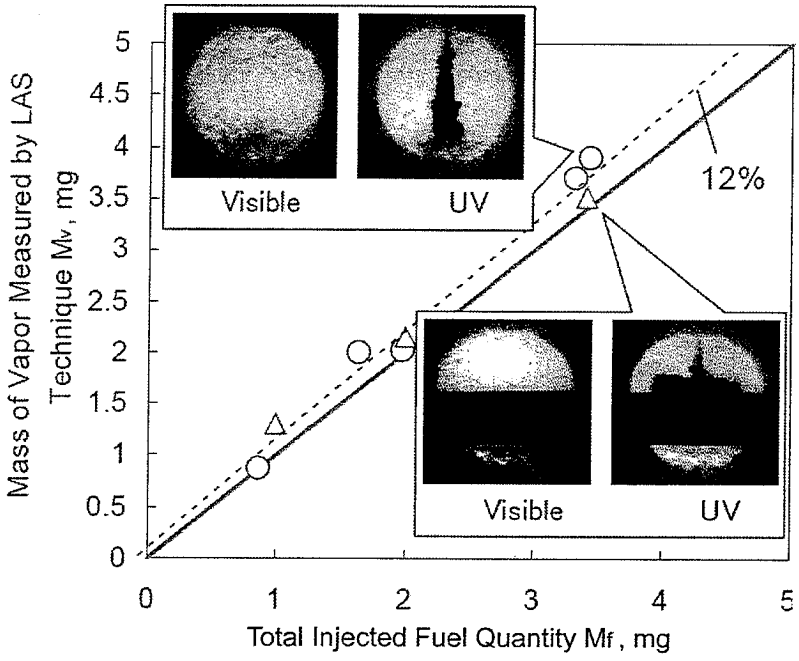

Figure 3.17 Comparison of total injected fuel quantity and vapor mass measured under complete evaporating condition (Matsumoto et al., 2008)

In this research, to estimate the overall accuracy of the LAS technique, an experiment on completely evaporated free spray was conducted. The images were acquired at a timing long enough after the end of injection (EOI) when no liquid phase fuel could be detected by the visible light. It is assumed that all injected fuel evaporated completely at this timing. The difference between the calculated vapor mass and weighted injected fuel mass was used to estimate the accuracy. The measurement was performed for both free and flat wall impinging sprays. As shown in **Fig. 3.17**, it is

found that, under completely evaporated conditions, the average measurement error of the vapor mass was approximately 12% (Matsumoto et al., 2008). This error increased with increasing amount of the liquid fuel in the mixture.

3.4.3 Data Processing for Axisymmetric Sprays

As mentioned previously, the LAS technique was initially implemented with an assumption of axisymmetric Diesel sprays. The procedures of data processing, as shown in **Fig. 3.18**, are briefly described here. According to the Lambert-Beer's law, at the absorbing wavelength (266 nm), the total optical thickness measured using a CCD camera included the optical thickness of vapor due to absorption and the optical thickness of drops due to the scattering and absorption; whereas at the non-absorbing wavelength (532 nm), the total optical thickness measured using a second CCD camera was the optical thickness of drops due to scattering alone. Since it had been experimentally proved that the optical thickness of drops at the two wavelengths was almost identical in a Diesel spray, the optical thickness of vapor could be obtained by subtracting the total optical thickness at 532 nm from the total optical thickness at 266 nm. Therefore, using the onion-peeling model, the vapor concentration distribution could be calculated from the optical thickness of the vapor and the mass of entrained gas could be integrated if the spray was axisymmetric. Furthermore, the equivalence ratios of both vapor and liquid fuel could be calculated.

3.4.4 Data Processing for Non-Axisymmetric Sprays

When the LAS technique is implemented in a non-axisymmetric spray, such as a spray impinging on a 2-D piston cavity shape wall and a spray injected by a 2-hole nozzle, the onion-peeling model described previously cannot be employed to calculate the fuel vapor concentration distribution. Therefore, an extended LAS data processing method should be developed. The method of data processing for non-axisymmetric sprays used in this work was proposed by Zhang and Nishida (2004).

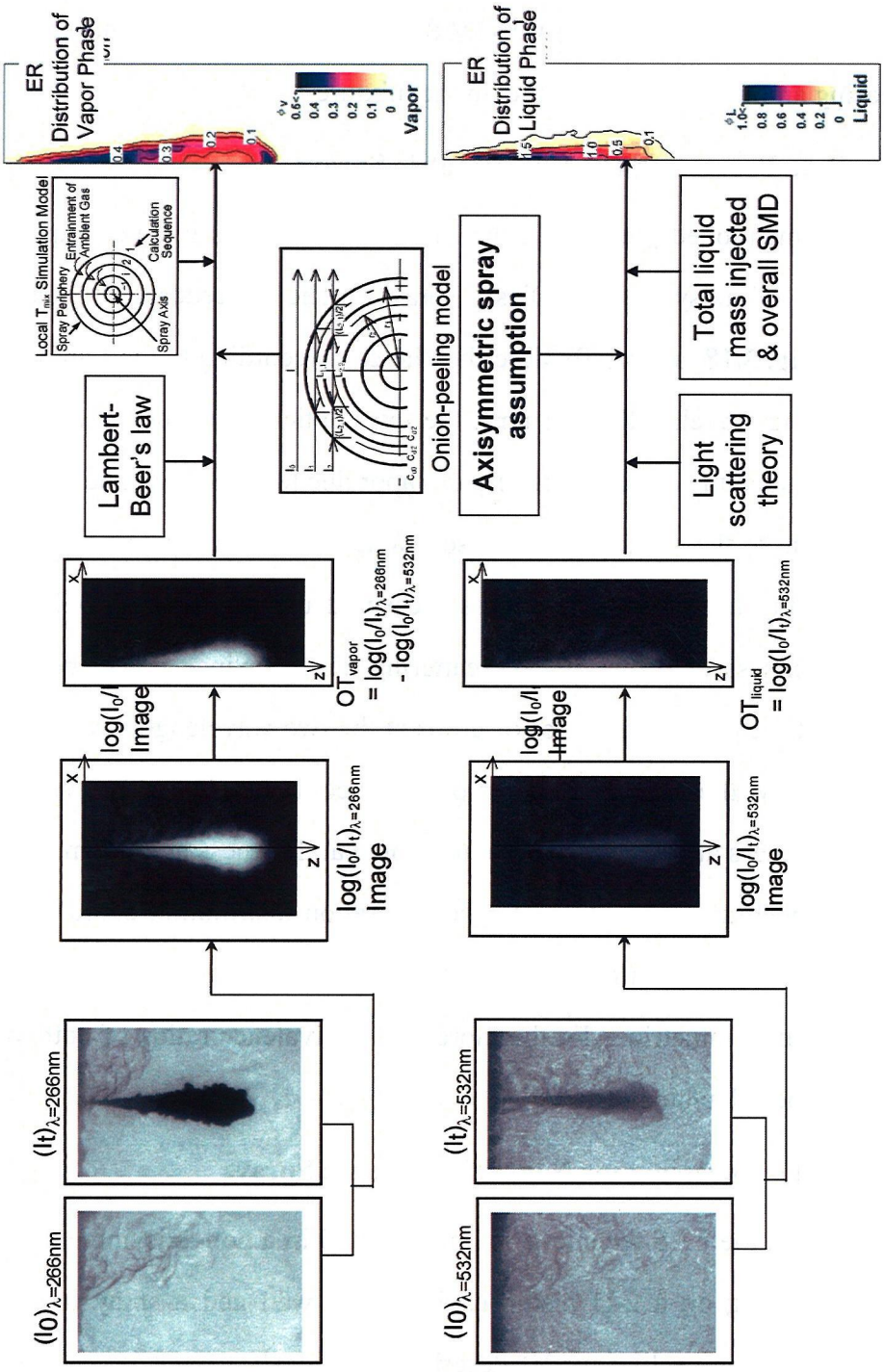

Figure 3.18 Flow chart of data processing for axisymmetric sprays

With assuming the molar absorption coefficient ε to be constant along a line of sight, **Eq. (3.5)** can be rewritten as

$$\ln\left(\frac{I_0}{I_t}\right)_{V_{abs}} = \frac{\varepsilon\times10^2}{MW}\cdot\int_0^L C_v dx = k_v\cdot m_v \tag{3.27}$$

or

$$m_v = \frac{MW}{\varepsilon\times10^2}\cdot\ln\left(\frac{I_0}{I_t}\right)_{V_{abs}} \tag{3.28}$$

where k_v is a proportional coefficient, and m_v is the mass of fuel vapor per unit projected area on the plane perpendicular to the incident beam axis. That is to say, the optical thickness of vapor is proportional to the vapor mass per unit projected area. Integrating **Eq. (3.28)** over the projected plane yields the total mass of vapor fuel, M_v:

$$M_v = \frac{MW}{\varepsilon\times10^2}\sum_S \ln\left(\frac{I_0}{I_t}\right)_{V_{abs}}\Delta S \tag{3.29}$$

where S : area of projected plane, m^2

ΔS : unit projected area, m^2

The optical thickness of the liquid phase fuel can also be assumed, under certain conditions, to be proportional to the mass of the liquid fuel per unit projected area. **Eq. (3.17)** can be rewritten as:

$$\ln\left(\frac{I_0}{I_t}\right)_{\lambda_T} = \frac{3}{2}\cdot\frac{R_k Q_{ext}}{\rho_f D_{32}}\cdot(C_l L) = k_l\cdot m_l \tag{3.30}$$

where k_l is a proportional coefficient, and m_l is the mass of the liquid fuel per unit projected area on the plane perpendicular to the incident beam axis. Introducing **Eq. (3.18)**, k_l can be expressed as

$$k_l = \frac{1}{M_l}\cdot\sum_S \ln\left(\frac{I_0}{I_t}\right)_{\lambda_T}\Delta S \tag{3.31}$$

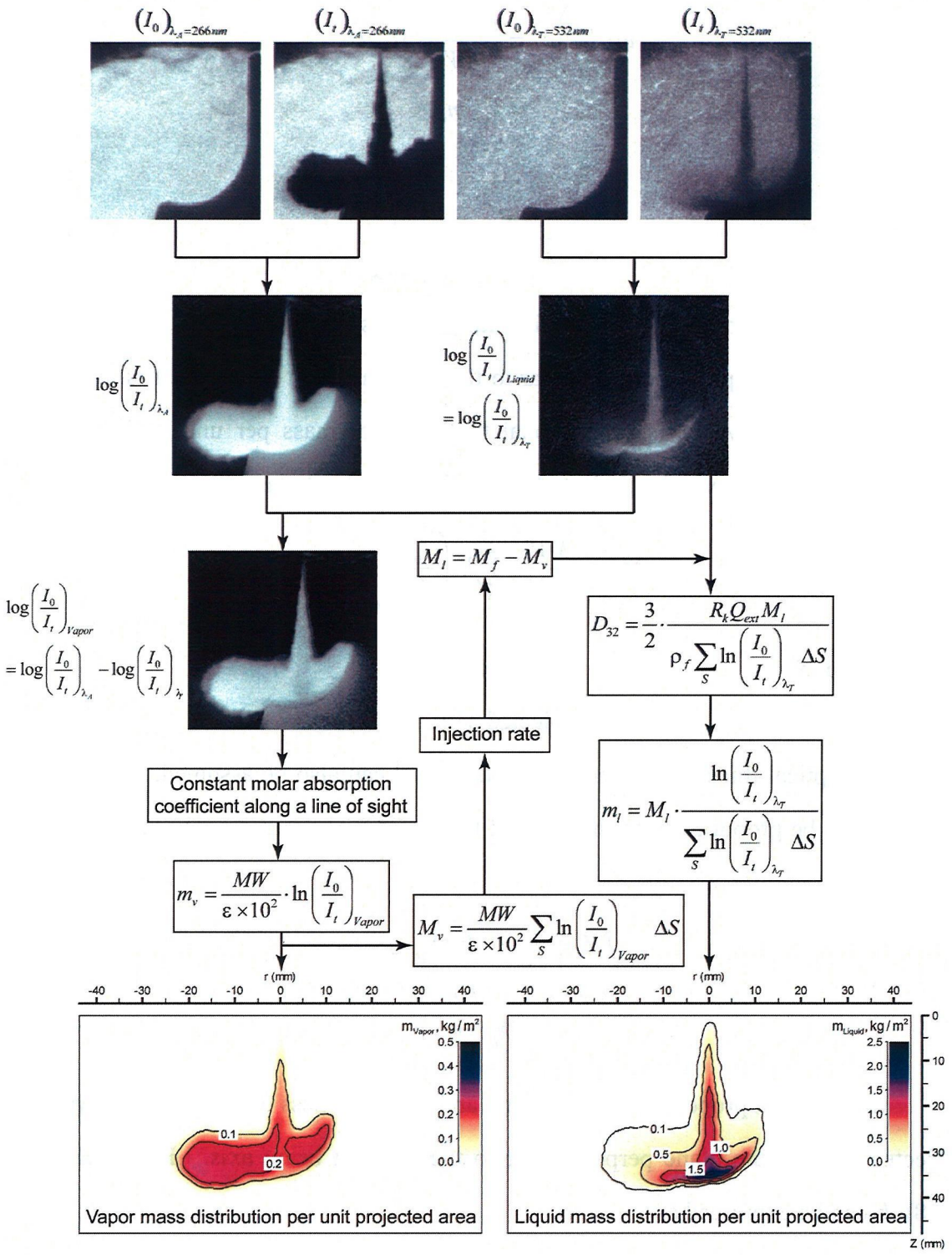

Figure 3.19 Flow chart of data processing for non-axisymmetric sprays

The total mass of the liquid phase fuel M_l can be obtained by removing the total mass of the vapor phase fuel M_v from the total injected fuel mass M_f that was determined from the injection rate curve.

$$M_l = M_f - M_v \tag{3.32}$$

Therefore, m_l can be expressed as

$$m_l = M_l \cdot \frac{\ln\left(\frac{I_0}{I_t}\right)_{\lambda_T}}{\sum_S \ln\left(\frac{I_0}{I_t}\right)_{\lambda_T} \Delta S} \tag{3.33}$$

As shown in **Fig. 3.19**, the procedures of data processing for non-axisymmetric sprays are summarized in a flow chart.

3.5 SUMMARY

In this dissertation work, a high pressure generation system was used to generate ultra-high injection pressures up to 300 MPa. A specially designed Diesel injector was employed and nozzles with different hole diameters ware investigated. Diesel sprays were formed under quiescent conditions in a constant volume vessel. Direct photography of non-evaporating sprays was conducted using a high-speed video camera system. The detailed mixture formation process was studied using the LAS technique. The LAS technique was applied to both axisymmetric and non-axisymmetric sprays. To correlate the mixture formation and combustion processes, direct photography and OH chemiluminescence imaging were carried out using a high-speed video camera system.

Chapter 4 Free Sprays

4.1 DIRECT PHOTOGRAPHY OF NON-EVAPORATING SPRAYS

4.1.1 Experimental Conditions

To acquire the preliminary knowledge of Diesel sprays, the direct photography of non-evaporating sprays was carried out using a high-speed video camera system. The primary variables were the injection pressure, nozzle hole diameter, and ambient density. **Table 4.1** shows the experimental conditions for the non-evaporating free spray. Four injection pressures (100, 200, 240, and 300 MPa) were investigated to clarify the effect of injection pressure on the spray and mixture characteristics. The nozzle with the diameter of 0.16 mm was selected as the baseline, and the performance of the other three nozzles (0.14, 0.10, and 0.08 mm) were investigated. Two ambient densities (11 and 15 kg/m^3) were used to simulate two engine conditions at different crank angles (-20 and -10 deg.ATDC). The parameters for the high-speed video camera system are shown in **Table 4.2**.

Table 4.1 Experimental conditions for direct photography of non-evaporating free spray

Ambient Gas Density (kg/m^3)	11 (-20 deg.ATDC)		15 (-10 deg.ATDC)	
Ambient Gas Pressure (MPa) /Temperature (K)	0.95/294		1.33/296	
Injection Pressure (MPa)	100	200	240	300
Nozzle Hole Diameter (mm)	0.16	0.14	0.10	0.08
Injection Quantity (mg)	15.47	11.85	6.04	3.87
Injection Duration (ms)	2.2 (@100MPa)	1.5 (@200MPa)	1.4 (@240MPa)	1.3 (@300MPa)
Assumed Number of Nozzle Holes for 70 mg	4	6	11	18

Table 4.2 Parameters for high-speed video camera system

Frame Rate (fps)	10,000
Resolution (pixel)	512 x 512
Exposure Time (s)	1/50,000
Focus Length (mm)	85
f/number	4.0

4.1.2 Spray Tip Penetration Length

Direct imaging of the Diesel sprays was performed under the non-evaporating conditions. For each test case, two sets of images were recorded by the high speed video camera. The background images were subtracted from the original ones and the images of free spray plumes were acquired. The spray plume was defined as the region with the intensity at least 20 counts larger than the background. By averaging the two sets of values acquired from the spray images, the spray tip penetration lengths were obtained. The results of spray tip penetration lengths for all test conditions are summarized in **Figs 4.1**, **4.2**, **4.3**, and **4.4**. It is obvious that the spray tip penetration length is dependent on the nozzle hole diameter. An increase in the injection pressure only causes a slight change in this dependency. With increasing the ambient density, the spray tip penetration length decreases and the difference between conventional nozzles (0.16 and 0.14 mm) and micro-hole nozzles (0.10 and 0.08 mm) becomes significant. At the high ambient density, to some extent, an increase in the injection pressure changes the dependency of the penetration on the nozzle hole diameter. Especially under the pressure of 300 MPa, four curves in **Fig. 4.4(b)** translate away to each other and the tendency is similar to that in **Fig. 4.4(a)**. It indicates that, at the high ambient density, to obtain a relatively high penetration length, higher injection pressures are required to generate enough kinetic energy.

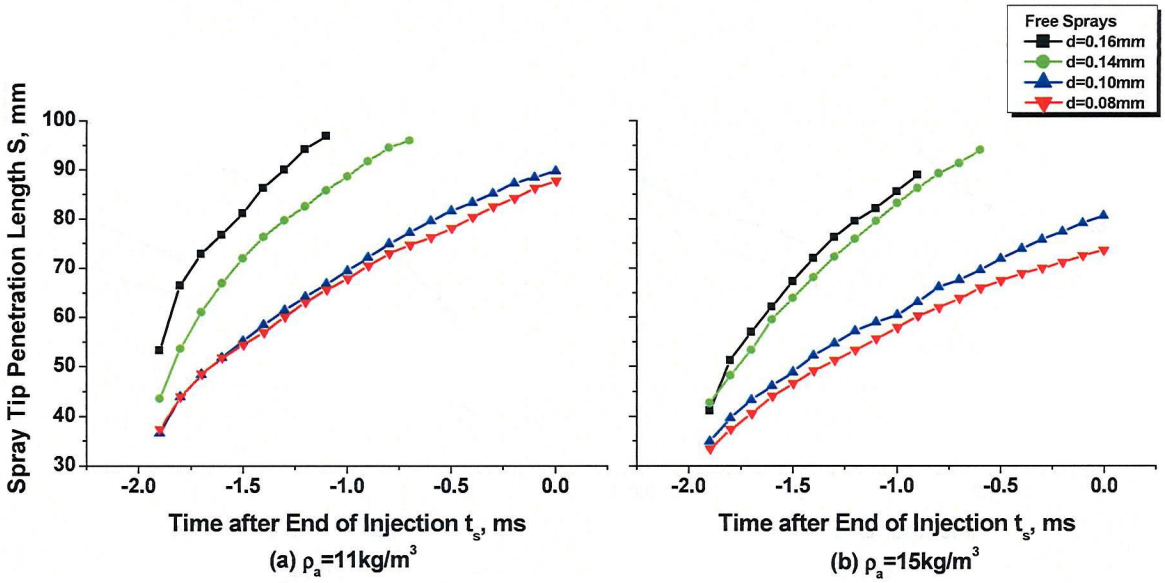

Figure 4.1 Spray tip penetration length versus time after EOI, non-evaporating free sprays, P_{inj} = 100 MPa, d = 0.16, 0.14, 0.10, and 0.08 mm, (a) ρ_a = 11 kg/m^3, (b) ρ_a = 15 kg/m^3

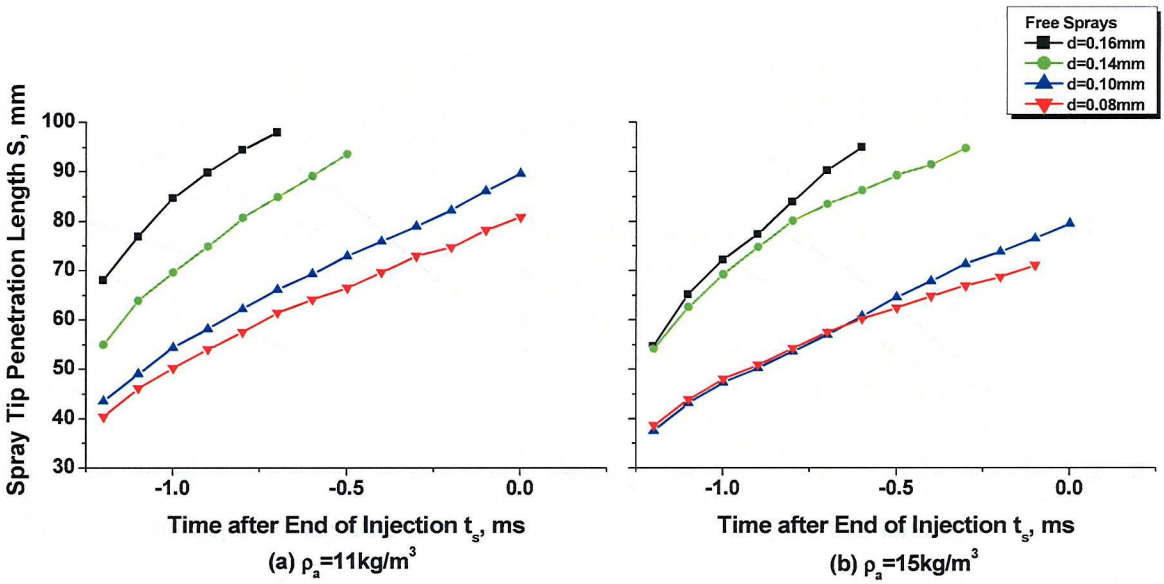

Figure 4.2 Spray tip penetration length versus time after EOI, non-evaporating free sprays, P_{inj} = 200 MPa, d = 0.16, 0.14, 0.10, and 0.08 mm, (a) ρ_a = 11 kg/m^3, (b) ρ_a = 15 kg/m^3

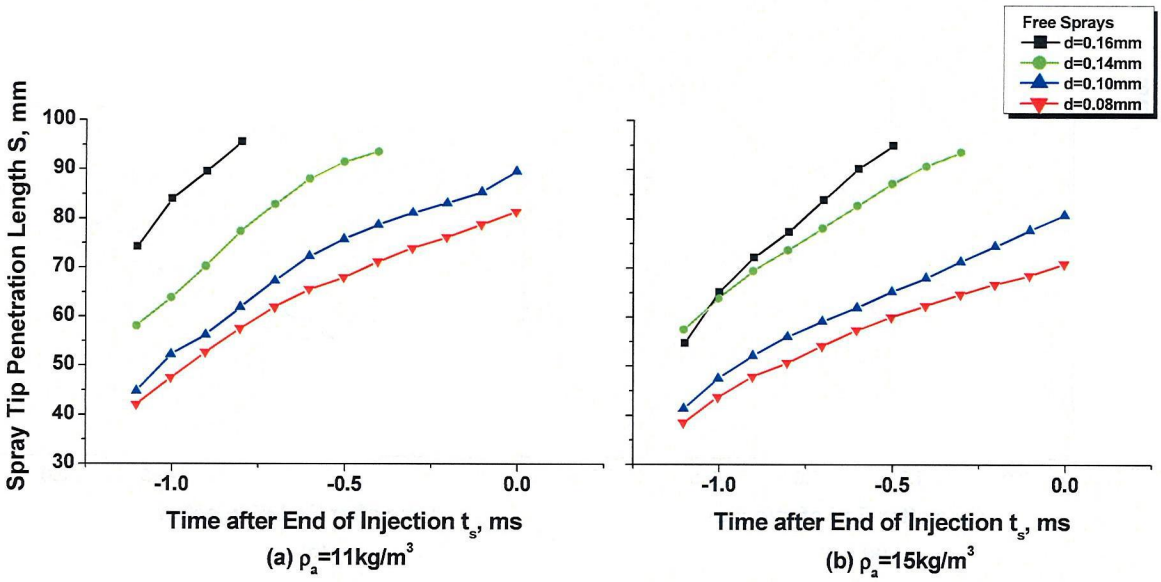

Figure 4.3 Spray tip penetration length versus time after EOI, non-evaporating free sprays, P_{inj} = 240 MPa, d = 0.16, 0.14, 0.10, and 0.08 mm, (a) ρ_a = 11 kg/m^3, (b) ρ_a = 15 kg/m^3

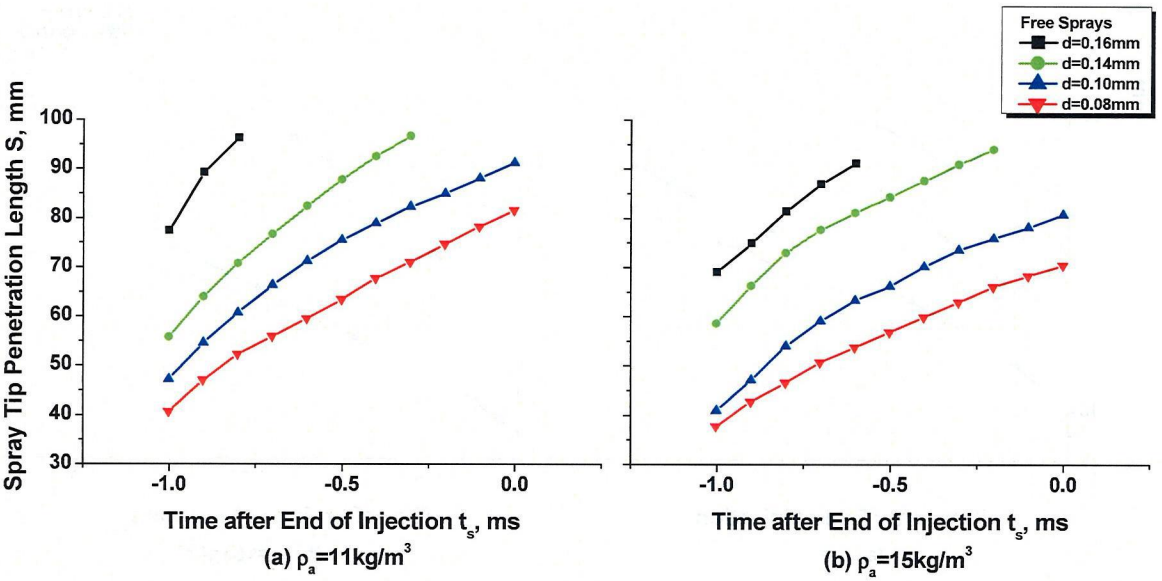

Figure 4.4 Spray tip penetration length versus time after EOI, non-evaporating free sprays, P_{inj} = 300 MPa, d = 0.16, 0.14, 0.10, and 0.08 mm, (a) ρ_a = 11 kg/m^3, (b) ρ_a = 15 kg/m^3

4.2 MEASUREMENT OF FREE SPRAYS USING LAS TECHNIQUE

4.2.1 Experimental Conditions

For non-evaporating sprays, a little information can be acquired using the direct photography system. In addition, at the operating conditions in real engines, the fuel vaporization is a vital process for the mixture formation and combustion. There are large differences between evaporating and non-evaporating sprays. Therefore, it is necessary to acquire sufficient information on the evaporating sprays from various nozzles under different injection pressures. In this work, as a part of the preliminary experiments, the LAS technique was employed to investigate the free sprays with varying the injection parameters.

Table 4.3 shows the experimental conditions. Note that an ambient density of 22 kg/m^3 was used. This density is higher than that used in other experiments of this dissertation work. To acquire more data with the limited window range, this higher density was employed to reduce the penetration length. The baseline condition was the nozzle hole diameter of 0.16 mm and injection pressure of 100 MPa. The measurements

Table 4.3 Experimental conditions for evaporating free sprays using LAS technique

Ambient Gas Density (kg/m^3)	22			
Ambient Gas Pressure (MPa) /Temperature (K)	4.52/673			
Injection Pressure (MPa)	100	200	300	
Injection Duration (ms)	2.2 (@100MPa)	1.5 (@200MPa)	1.3 (@300MPa)	
Laser Shot Timing (msAEOI)	0	0.5	1.0	
Nozzle Hole Diameter (mm)	0.16	0.14	0.10	0.08
Injection Quantity (mg)	15.47	11.85	6.04	3.87
Assumed Number of Nozzle Holes for 70 mg	4	6	11	18

were made of reducing the hole diameter and increasing the injection pressure step by step. The effects of the injection pressure and nozzle hole diameter were investigated using the LAS technique and axisymmetric data processing method.

Figure 4.5 shows the raw images of the spray plumes from 0.08 mm nozzle. The upper row of images, taken by the visible light, provides the 2-D distribution of theliquid phase fuel in the spray. The lower row of images, taken by the ultraviolet light, presents the distribution of the total injected fuel in the spray. After the data

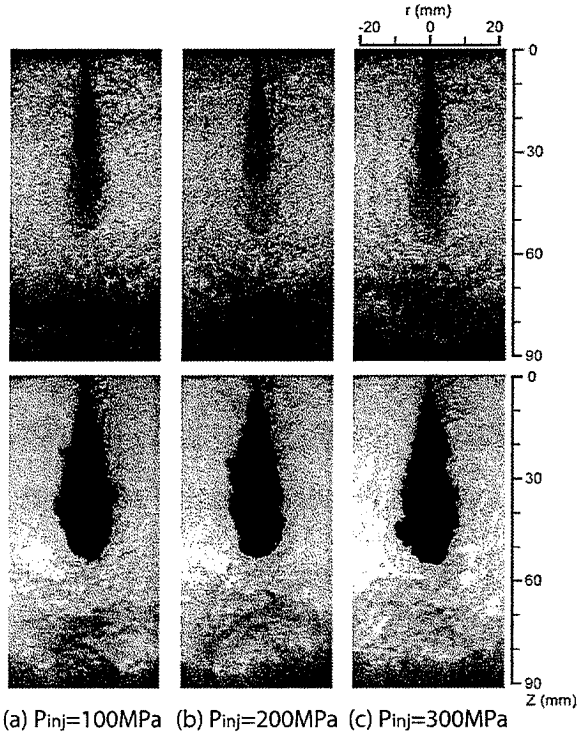

Figure 4.5 Raw images of evaporating free spray plumes, t_s = 0 msAEOI, d = 0.08 mm, P_{inj} =100, 200, and 300 MPa, ρ_a = 22 kg/m^3

processing, some useful information could be acquired. **Figure 4.6** shows the spray tip penetration length and SMD versus the time after EOI at different injection pressures. Note that all laser shot timings in this section are after the end of injection. An increase in the injection pressure results in an increase in the spray tip penetration length. In addition, with increasing the injection pressure, SMD decreases significantly after EOI. It indicates that the ultra-high injection pressure can intensify the dispersion of the fuel

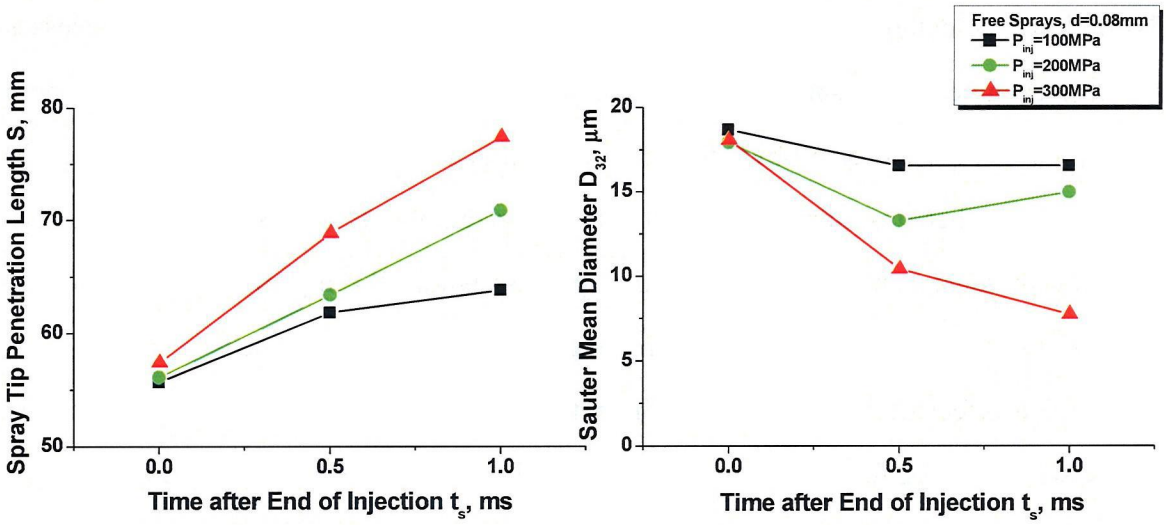

Figure 4.6 Spray tip penetration length and Sauter mean diameter versus time after EOI, d = 0.08 mm, P_{inj} =100, 200, and 300 MPa, ρ_a = 22 kg/m^3

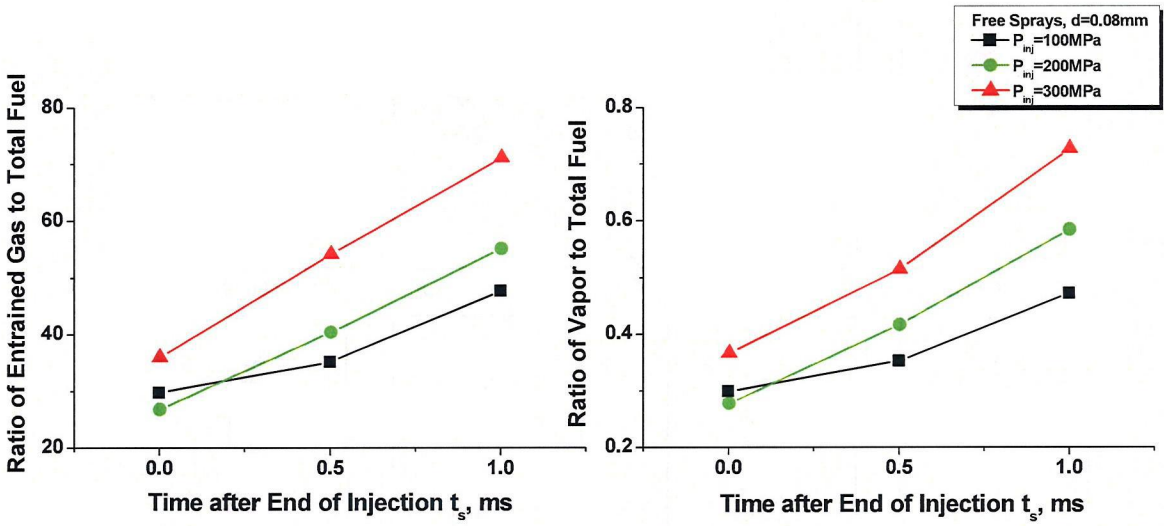

Figure 4.7 Ratio of entrained gas to total fuel (M_a/M_f) and Ratio of vapor to total fuel (M_v/M_f) versus time after EOI, d = 0.08 mm, P_{inj} =100, 200, and 300 MPa, ρ_a = 22 kg/m^3

and the disintegration of the fuel droplets. It is worth noting that, there are no pronounced differences in SMD at EOI. However, after EOI, SMD decreases significantly with increasing the injection pressure. It may be explained by the fact that the secondary breakup, which is primarily driven by aerodynamic forces exerted upon the droplets by the surrounding gas, is greatly influenced by the increased injection pressure.

To find out the detailed mechanism, the gas entrainment and fuel vaporization processes were investigated. As shown in **Fig. 4.7**, with increasing the injection pressure, both M_a/M_f and M_v/M_f increase obviously. Note that, at EOI, the micro-hole nozzle at 300 MPa has a higher gas entrainment and fuel vaporization. It means that the ultra-high injection pressure can enhance the mixing process within the injection duration, which plays an important role in reducing the mixing time for PCI combustion.

The effect of the nozzle hole diameter was shown in **Fig. 4.8**. By examining **Fig. 4.8(a)**, it can be found that, with decreasing the nozzle hole diameter, the liquid

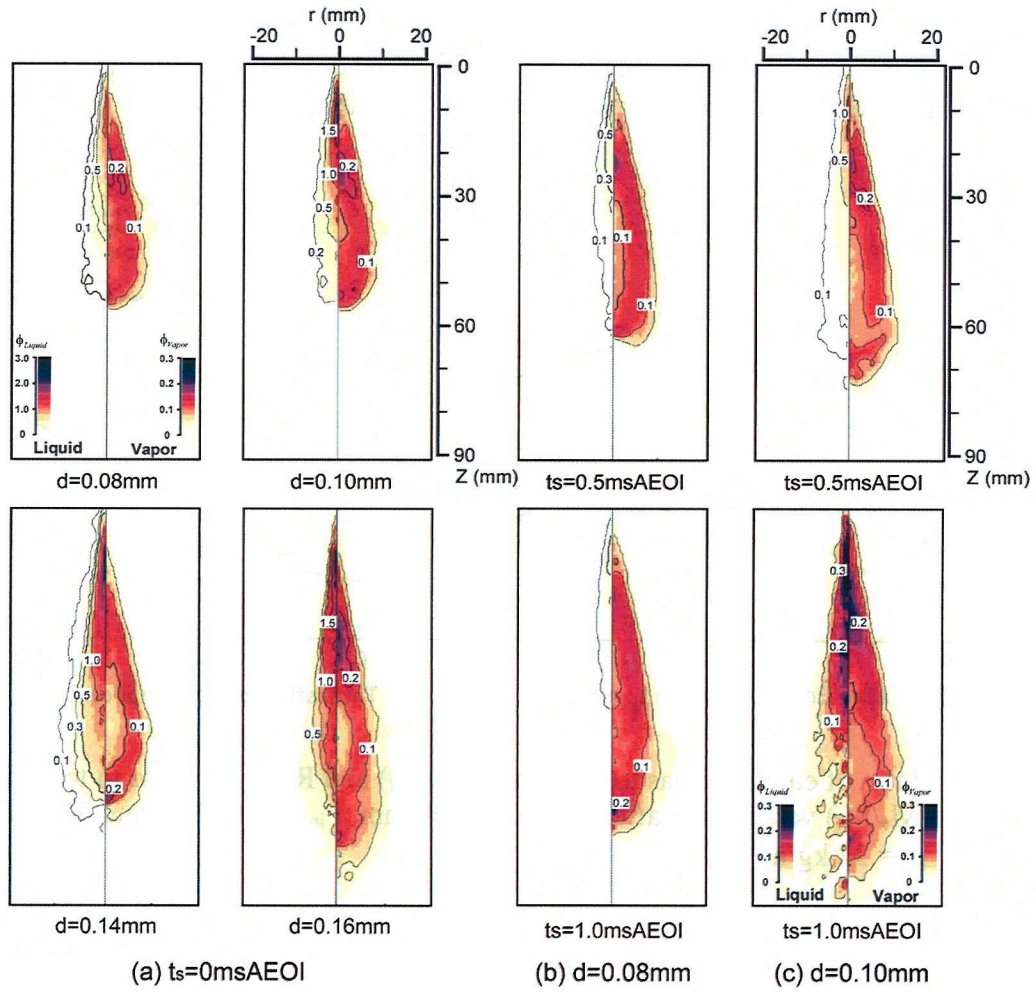

Figure 4.8 Contours of equivalence ratio distributions, P_{inj} = 300 MPa ρ_a = 22 kg/m^3, (a) d = 0.08, 0.10, 0.14, and 0.16 mm, t_s = 0 msAEOI, (b) d = 0.08 mm, t_s = 0.5 & 1.0 msAEOI, (c) d = 0.10 mm, t_s = 0.5 & 1.0 msAEOI

phase concentration decreases significantly. It indicates that the smaller droplets generated from a nozzle with a smaller hole diameter can vaporize very fast. Comparison of **Figs 4.8(b)** and **(c)** shows that, for the 0.08 mm nozzle at 1.0 ms AEOI, there is almost no liquid phase fuel left. And the vapor phase is more uniform than that for the 0.10 mm nozzle. Therefore, at the pressure of 300 MPa, with decreasing the nozzle hole diameter, not only the penetration decreases but also the air-fuel mixture becomes lean and uniform within a short time after EOI.

4.3 SUMMARY

Preliminary investigations were made of the direct photography of the non-evaporating free sprays and the quantitative imaging of the evaporating sprays using the LAS technique. The injection pressure, nozzle hole diameter, and ambient density were varied to acquire the basic knowledge of Diesel sprays from micro-hole nozzles under ultra-high injection pressures. Findings are summarized as follows.

1. Non-evaporating spray imaging shows that the spray tip penetration length is dependent on the nozzle hole diameter. This dependence is almost invariant with increasing the injection pressure, whereas it is influenced by the increased ambient density. At the higher ambient density, increasing the injection pressure up to 300 MPa may slightly change the dependence of the penetration on the nozzle hole diameter.
2. Results acquired using the LAS technique and axisymmetric data processing method show that the secondary breakup is influenced by increasing the injection pressure, which result in a significant decrease in SMD after EOI.
3. The combination of a micro-hole nozzle and an ultra-high injection pressure can accelerate the preparation of a lean and uniform mixture, which provides some promising characteristics for PCI combustion close to TDC.

Chapter 5 Sprays Impinging on a Flat Wall

5.1 EXPERIMENTAL CONDITIONS

To clarify the influence of the spray/wall interactions on the air-fuel mixture formation process, Diesel sprays impinging on a flat wall were studied using the LAS technique under both evaporating and non-evaporating conditions. Experimental conditions for evaporating sprays were determined according to the real engine conditions and are listed in **Table 1**. Two ambient densities (11 and 15 kg/m^3) were used to simulate two engine conditions at different crank angles (-20 and -10 deg.ATDC). Three injection pressures (100, 240, and 300 MPa) were investigated to clarify the effect of the injection pressure on the spray and mixture characteristics. The nozzle with a diameter of 0.16 mm was selected as the baseline, and the performance of two micro-hole nozzles (0.10 and 0.08 mm) was investigated. To simulate the operating condition of the prototype engine at full load, the injection quantity of the single-hole nozzle was determined by holding the total injection quantity at 70 mg/stroke and the total cross-sectional hole area at the same value. Injection durations were determined by the injection rate curves. The injection rate curves measured with the Bosch method at three injection pressures are given in **Fig. 3.2**. Since the objective of present study was to achieve premixed compression ignition (PCI) combustion close to TDC, EOI was used as the temporal reference point to investigate the mixing process both during and after the injection duration. The spray properties of 0.08 mm nozzle were measured at four timings (-0.5, 0, 0.5, and 1.0 msAEOI), however the spray properties of 0.10 and 0.16 mm nozzles could only be measured at three timings (-0.5, 0, and 0.5 msAEOI) and two timings (-0.5 and 0 msAEOI) respectively, because of the visual range limitation of the quartz windows in the constant volume vessel.

Table 5.2 shows the experimental conditions for non-evaporating sprays impinging on a flat wall. To rule out the effect of ambient density on the atomization process, the ambient densities were the same as those of elevated conditions. Only the

baseline condition (d = 0.16 mm and P_{inj} = 100 MPa) and objective condition (d = 0.08 mm and P_{inj} = 300 MPa) were investigated for non-evaporating sprays.

Table 5.1 Experimental conditions for evaporating sprays impinging on a flat wall

Ambient Gas Density (kg/m^3)	11 (-20 deg.ATDC)		15 (-10 deg.ATDC)
Ambient Gas Pressure (MPa) /Temperature (K)	2.6/797		4.04/885
Injection Pressure (MPa)	100	240	300
Nozzle Hole Diameter (mm)	0.16	0.10	0.08
Injection Quantity (mg)	15.47	6.04	3.87
Injection Duration (ms)	2.2 (@ 100 MPa)	1.4 (@ 240 MPa)	1.3 (@ 300 MPa)
Assumed Number of Nozzle Holes for 70 mg	4	11	18
Laser Timing (msAEOI)	-0.5, 0	-0.5, 0, 0.5	-0.5, 0, 0.5, 1.0

Table 5.2 Experimental conditions for non-evaporating sprays impinging on a flat wall

Ambient Gas Density (kg/m^3)	11 (-20 deg.ATDC)	15 (-10 deg.ATDC)
Ambient Gas Pressure (MPa) /Temperature (K)	0.95/294	1.33/296
Injection Pressure (MPa)	100	300
Nozzle Hole Diameter (mm)	0.16	0.08
Injection Quantity (mg)	15.47	3.87
Injection Duration (ms)	2.2 (@ 100 MPa)	1.3 (@ 300 MPa)
Assumed Number of Nozzle Holes for 70 mg	4	18
Laser Timing (msAEOI)	-0.5, 0	-0.5, 0, 0.5, 1.0

5.2 EFFECTS OF NOZZLE HOLE DIAMETER, INJECTION PRESSURE, AND AMBIENT DENSITY

5.2.1 Structure of Flat Wall Impinging Spray

The overall structures of the flat wall impinging sprays at three representative conditions are shown in optical thickness images (Fig. 4) taken by the LAS system. The liquid phase distributions were observed through the optical thickness at 532 nm (**Fig. 5.1**, left-hand column), and the vapor and liquid phases were observed through the optical thickness at 266 nm (**Fig. 5.1**, right-hand column). The spray tip penetration length in the present study was defined as the axial distance (S_{Axial}) from the nozzle tip to the impingement point plus the radial distance (S_{Radial}) from the impingement point to the furthest location of the fuel (**Fig. 5.1(a)**).

Comparison of **Fig. 5.1(a)** (d = 0.16 mm and P_{inj} = 100 MPa) and **Fig. 5.2(b)** (d = 0.08 mm and P_{inj} = 100 MPa) shows that the spray tip penetration length decreases significantly (S_{Radial} reduces by almost half at EOI) because of the decrease in the injected fuel quantity. In addition, note that there is much more liquid phase fuel close to the flat wall for the 0.16 mm nozzle than for the 0.08 mm nozzle. This indicates that the micro-hole nozzle is very effective in reducing the wall wetting.

Comparison of **Fig. 5.1(b)** (d = 0.08 mm and P_{inj} = 100 MPa) and **Fig. 5.1(c)** (d = 0.08 mm and P_{inj} = 300 MPa) shows the clear difference in the visible images. (Note that the injected fuel quantity at -0.5 msAEOI was different at two injection pressures because EOI was used as the temporal reference point.) In **Fig. 5.1(b)**, large part of fuel is located in the region close to the wall surface, whereas in **Fig. 5.1(c)**, fuel is dispersed into the region away from the wall surface. This indicates that the spray/wall interactions are intensified by increasing the injection pressure from 100 to 300 MPa. Therefore, more droplets with small diameters can be generated after the wall impingement.

By examining the UV images at EOI, it is worth noting that the volumes of the spray plumes are almost the same, but the optical thickness gradient at the edge region of

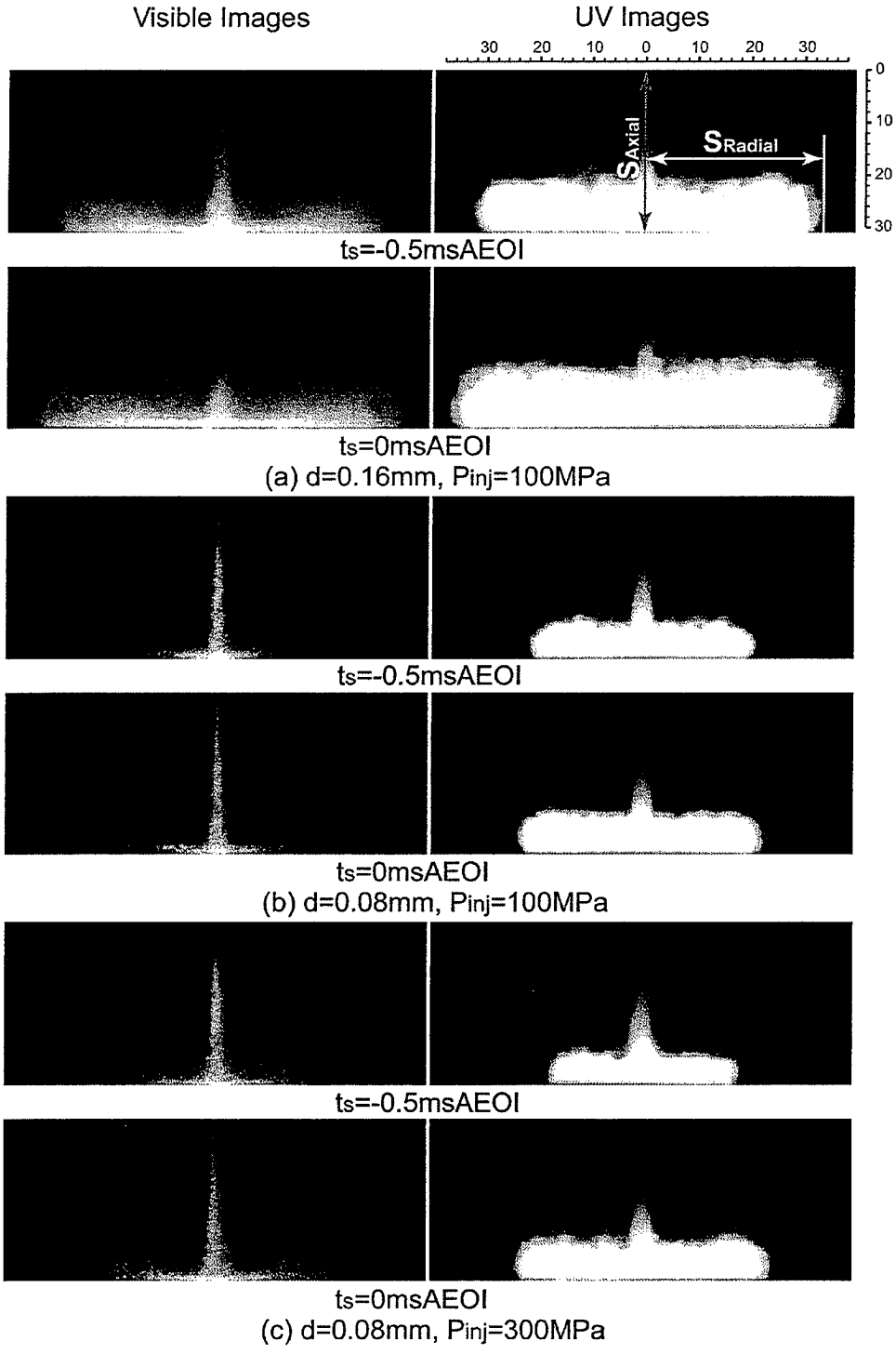

Figure 5.1 Optical thickness images for three representative conditions, ρ_a = 11 kg/m^3 (P_a = 2.6 MPa, T_a = 797 K)

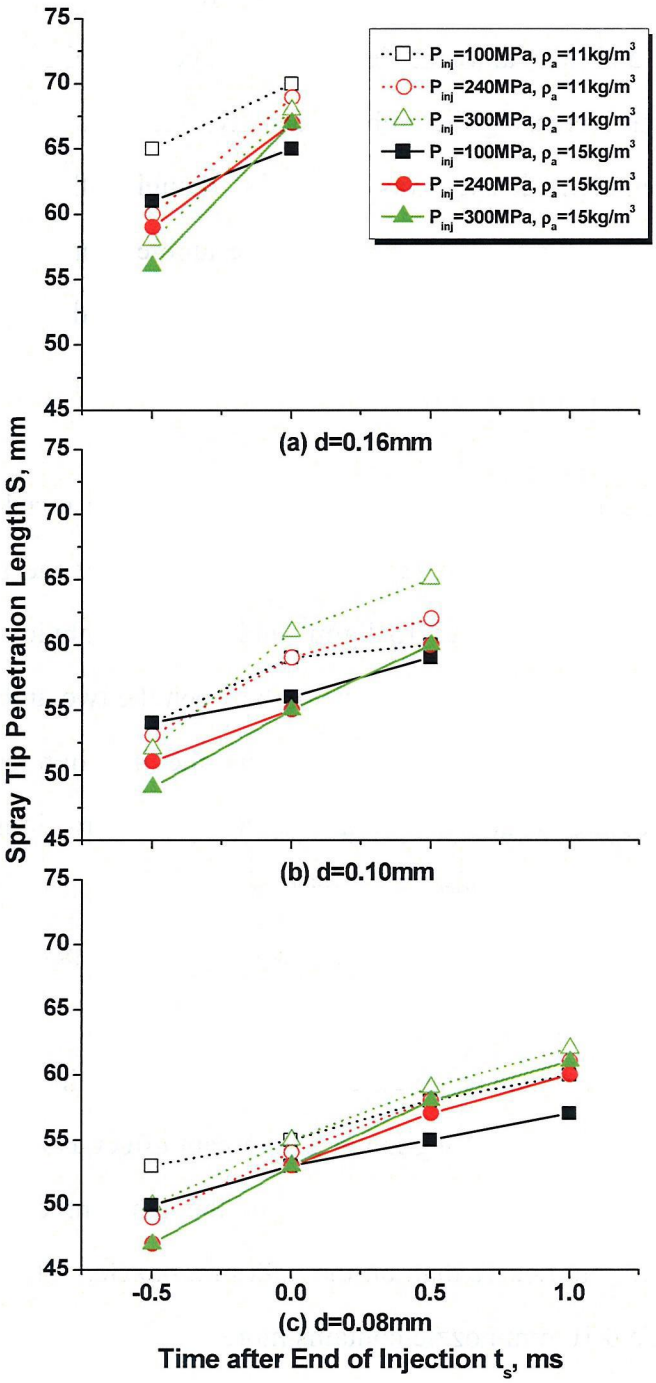

Figure 5.2 Spray tip penetration length under various injection pressures and ambient densities, (a) d = 0.16 mm, (b) d = 0.10 mm, (c) d = 0.08 mm

the spray plumes becomes smoother with increasing the injection pressure. It indicates that a leaner mixture is located at the edge region under the ultra-high injection pressure condition.

Figure 5.2 shows the spray tip penetration length of three nozzles under three injection pressures and two ambient densities. In general, the spray tip penetration length decreases with increasing the ambient density. It must be emphasized here that, in this study, the ambient density was varied by changing the ambient pressure and ambient temperature together. An increase in the ambient pressure would reduce the penetration by enhancing the atomization, spray dispersion, and air entrainment. At the same time, an increase in the ambient temperature would enhance the vaporization and slightly decrease the penetration.

By examining **Fig. 5.2**, different tendencies for three nozzles can be clarified. The data at EOI for 0.16 mm nozzle (**Fig. 5.2(a)**) show that the smallest penetration length is obtained at 100 MPa and 15 kg/m^3 and increases obviously with decreasing ambient density. The difference in penetration between the two ambient densities at the same injection pressure decreases with increasing the injection pressure. Since the higher injection pressure results in stronger spray/wall interactions, the wall wetting effect may be reduced and more fuel will spread away from the wall after the impingement. This may compensate for the decrease in the penetration length caused by the high ambient density.

When two kinds of micro-hole nozzles are compared in **Figs 5.2(b)** and **(c)**, it clearly indicates that the wall wetting is not a dominant effect as less liquid phase fuel is left at EOI. Results show that the increase in the ambient density has a stronger influence on the 0.10 mm nozzle than on the 0.08 mm nozzle. It implies that the spray plume formed by the 0.10 mm nozzle contains more droplets with large diameters whose breakup is greatly influenced by the increased ambient density. On the other hand, the small difference for the 0.08 mm nozzle shows that there is a compromise between the increased spray momentum and intensified vaporization.

5.2.2 Comparison of 0.16 and 0.10 mm Nozzles

When the injection pressure is increased from 100 to 300 MPa for the 0.10 mm nozzle, as shown in **Fig. 5.3**, M_a/M_f increases slightly and M_v/M_f remains almost

constant. This lack of change in M_a/M_f and M_v/M_f with increasing the injection pressure is consistent with the free jet results acquired by Siebers (1999). This

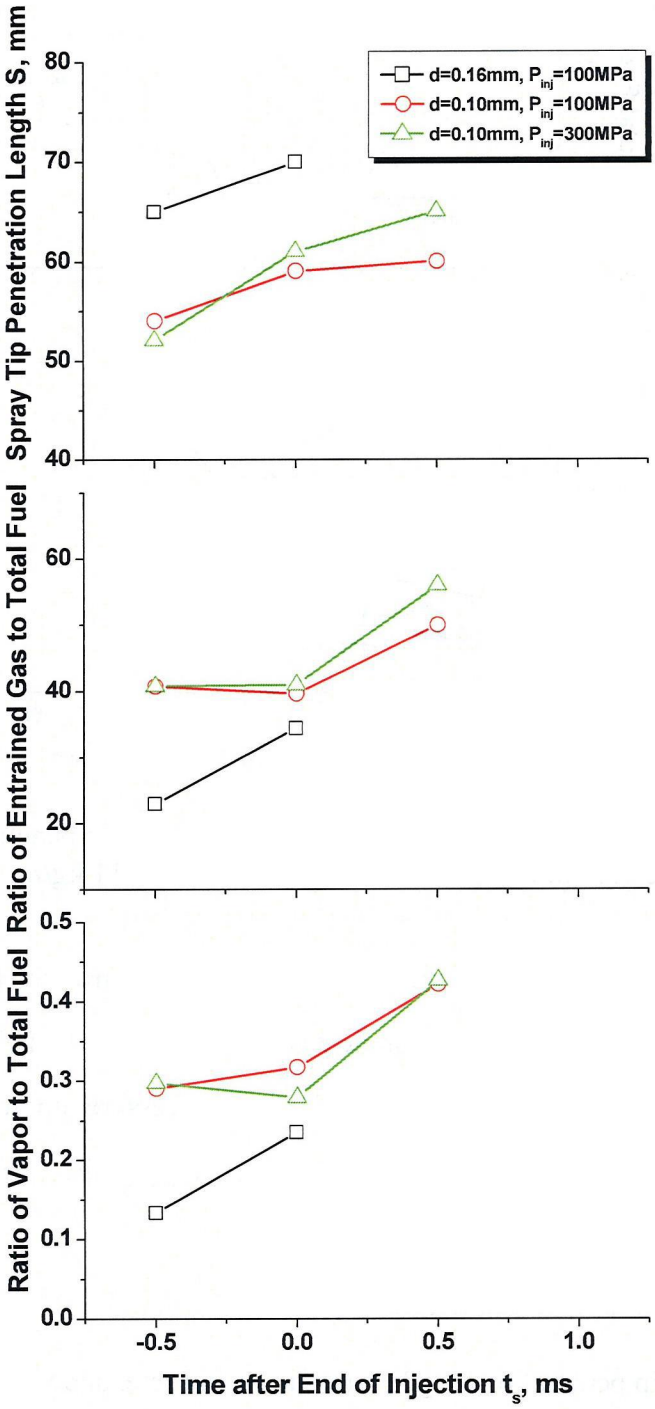

Figure 5.3 Spray tip penetration length, ratio of entrained gas to total fuel, and ratio of vapor to total fuel versus time after EOI, d =0.10 & 0.16 mm, P_{inj} = 100 & 300 MPa, ρ_a = 11 kg/m^3

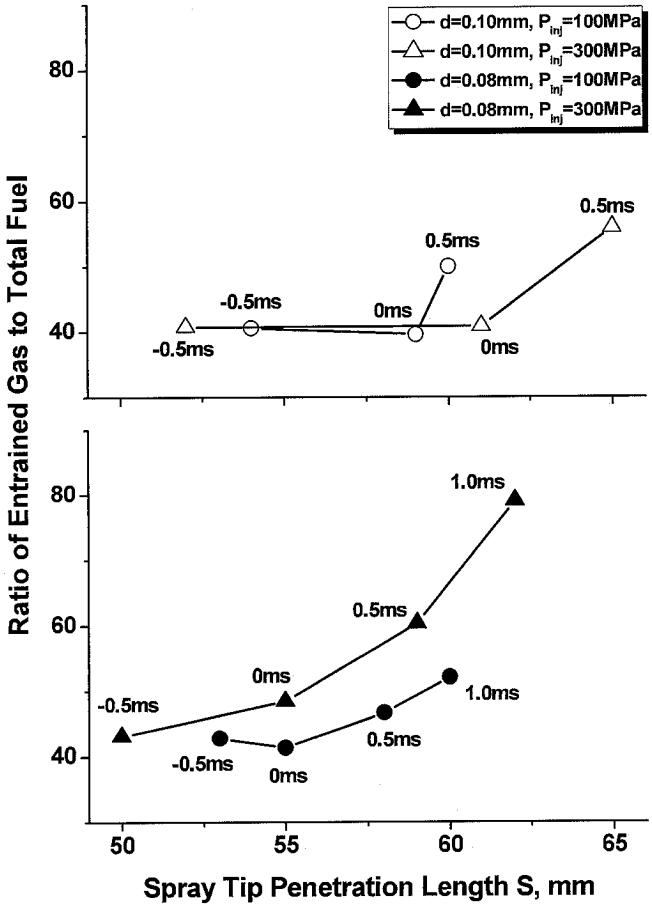

Figure 5.4 Ratio of entrained gas to total fuel versus spray tip penetration length, d = 0.10 & 0.08 mm, P_{inj} = 100 & 300 MPa, ρ_a = 11 kg/m^3

agreement shows that the mixing-limited vaporization holds true for the impinging spray formed by the 0.10 mm nozzle. It indicates that, although reducing the nozzle hole diameter to 0.10 mm and increasing the injection pressure up to 300 MPa have a significant influence on the atomization process, varying these parameters does not change the basic jet scaling process.

5.2.3 Comparison of 0.10 and 0.08 mm Nozzles

The spray tip penetration length, air entrainment rate, and vaporization rate are the three important factors of the spray properties. The maps of M_a/M_f versus penetration and M_v/M_f versus penetration are shown in **Figs 5.4** and **5.5** respectively. The spray and mixture characteristics were investigated using two kinds of micro-hole nozzles (0.10 and 0.08 mm) under two different injection pressures (100 and 300 MPa). In **Fig. 5.4**, note

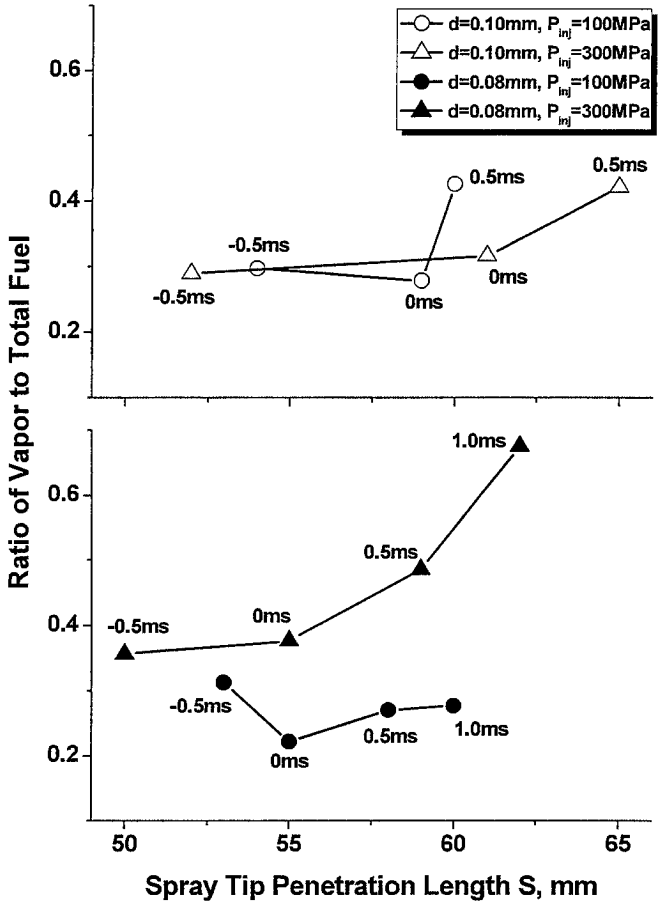

Figure 5.5 Ratio of vapor to total fuel versus spray tip penetration length, d = 0.10 & 0.08 mm, P_{inj} = 100 & 300 MPa, ρ_a = 11 kg/m^3

that M_a/M_f of 0.10 mm nozzle at EOI remains almost constant with increasing the injection pressure, whereas that of 0.08 mm nozzle increases obviously. It indicates that the mixing process within the injection duration for 0.08 mm nozzle is intensified by ultra-high injection pressures. These results, to some extent, are not consistent with the theory of mixing-limited vaporization. The detailed mechanism is still unclear and requires further studies. At the same time, the penetration length decreases significantly with decreasing the nozzle hole diameter. At 300 MPa and 0.5 msAEOI, two nozzles reach the similar value of M_a/M_f, but have different penetration lengths.

In **Fig. 5.5**, M_v/M_f at 100 MPa decreases a little from -0.5 msAEOI to EOI for the two nozzles, which is the opposite to the tendency of the conventional nozzle (Fig. 6). When the injection pressure is increased up to 300 MPa, the tendency is changed, which

is similar to that of the conventional one. It may be explained that the injection pressure of 100 MPa is not high enough for micro-hole nozzles to maintain a high kinetic energy close to EOI. Therefore, the speed of breakup and atomization processes decreases, thus resulting in more droplets with large diameters in the spray plumes. On the contrary, the injection pressure of 300 MPa can generate a very high spray momentum and can enhance the vaporization significantly. Currently, this explanation, however, is very difficult to justify because the measurement accuracy is relatively low for droplet size distribution under evaporating conditions.

5.2.4 Spray Equivalence Ratio Distributions of 0.08 mm Nozzle at 300 MPa

The contours of equivalence ratio distributions of both liquid and vapor phases fuel are shown in **Figs 5.6** and **5.7**. The spray and mixture characteristics of 0.08 mm nozzle at 300 MPa were investigated and the effect of ambient density is discussed in this subsection. It is found that the liquid-fuel-rich and vapor-fuel-rich fields move downwards with elapsed time. In the free spray region which is the part of spray plume above the impingement point, the richest field appears at the tip. After the impingement region, the liquid phase becomes very lean and the richest field of vapor phase appears at the tip of the radial jet region. Under this condition (micro-hole, ultra-high injection pressure, and hot wall), almost no obvious liquid fuel films are detected at the region close to the wall surface. It may be caused by the high spray momentum, strong spray/wall interactions, and fast vaporization.

Comparing the contours at different ambient densities indicates that the penetration length of both liquid and vapor phases decreases slightly with increasing the ambient density. At the same time, the liquid phase becomes leaner and the vapor phase becomes richer. It shows that more droplets with larger diameters disintegrate into smaller ones and more liquid fuel vaporizes at the higher ambient density. However, upstream of the free spray region, there are no pronounced differences between two conditions. The mechanism may be explained by the fact that the high ambient density can enhance the secondary breakup, spray dispersion, and air entrainment.

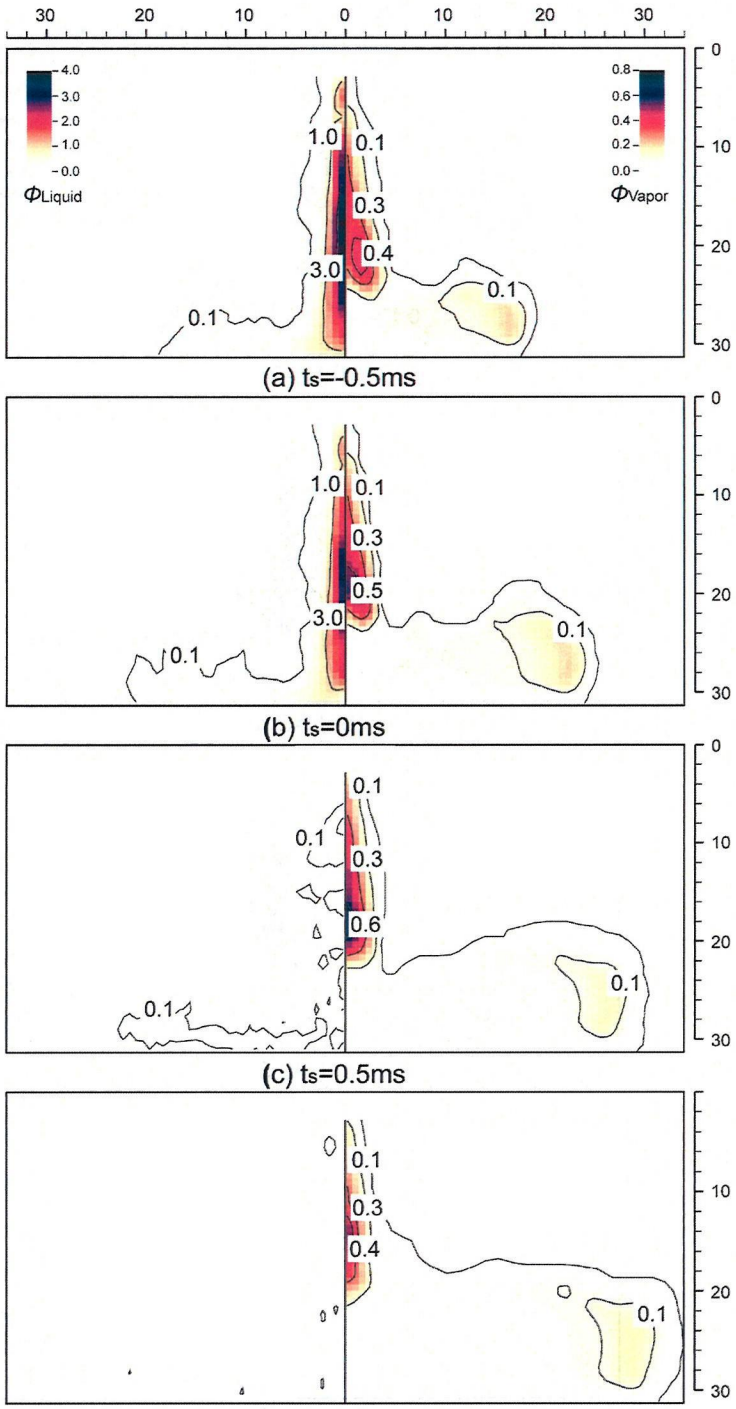

Figure 5.6 Contours of Equivalence Ratio Distributions, d = 0.08 mm, P_{inj} = 300 MPa, ρ_a = 11 kg/m^3

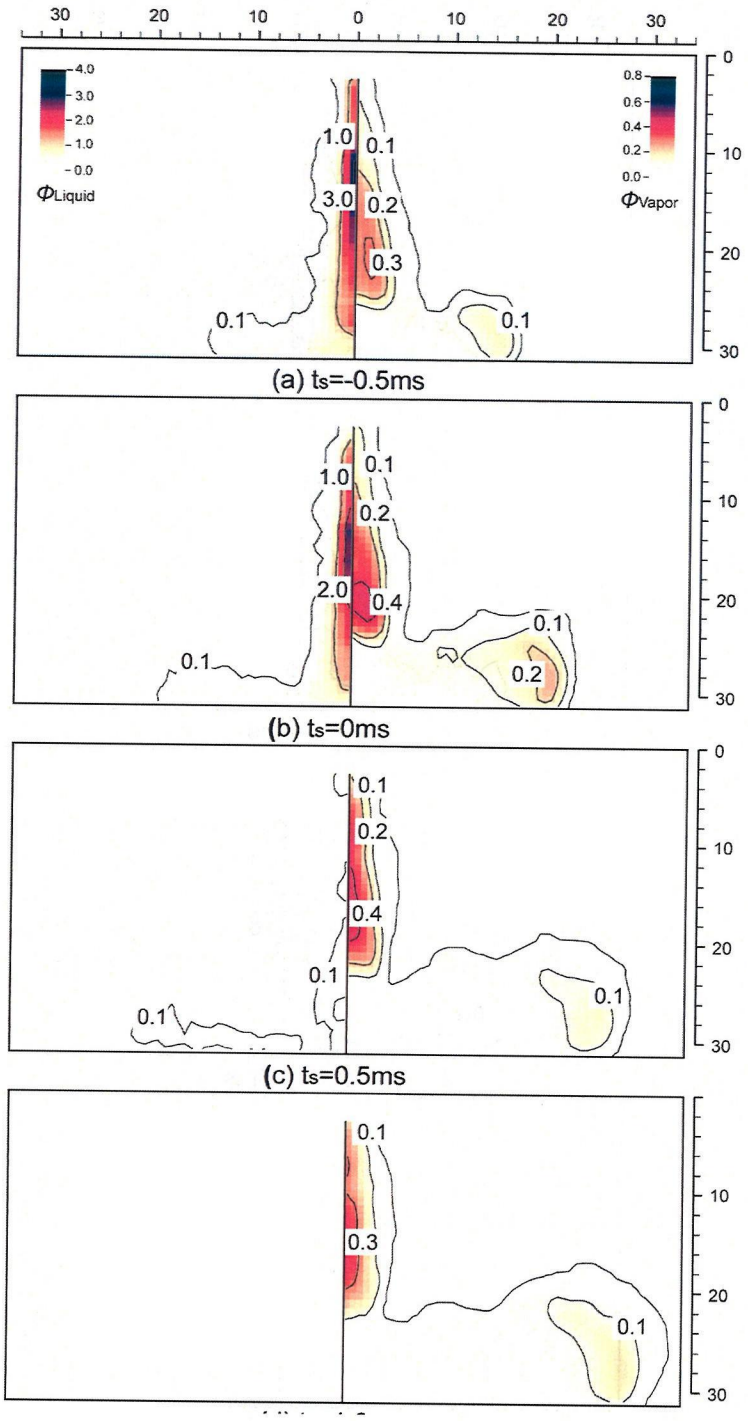

Figure 5.7 Contours of Equivalence Ratio Distributions, d = 0.08 mm, P_{inj} = 300 MPa, ρ_a = 15 kg/m^3

5.3 EFFECTS OF WALL IMPINGEMENT AND EVAPORATION

To clarify the effect of wall impingement on the sprays characteristics of the micro-hole nozzle under the ultra-high injection pressure, the maps of free sprays and flat wall impinging sprays were examined. As shown in **Fig. 5.8**, the spray tip penetration length decreases significantly and M_v/M_f decreases greatly by the wall impingement. It means that the vaporization process is inhibited by the wall impingement, which may be caused by the wall wetting effect. However, M_a/M_f increases slightly within the injection duration. It may be explained that the high spray momentum generated by ultra-high injection pressure intensifies the air entrainment and mixing process. At the

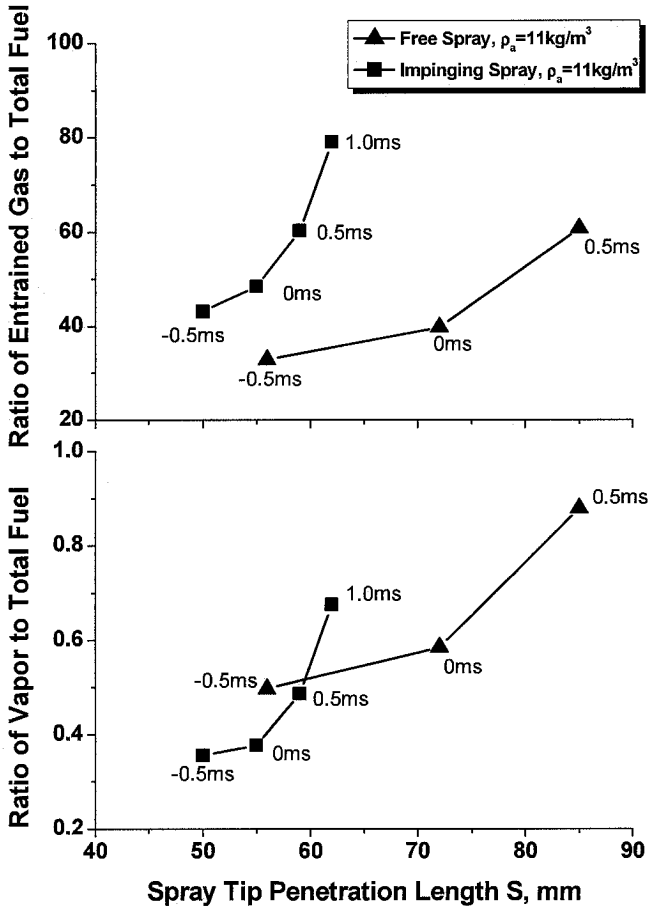

Figure 5.8 Ratio of entrained gas to total fuel and ratio of vapor to total fuel versus spray tip penetration length, free spray and flat wall impinging spray, d = 0.08 mm, P_{inj} = 300 MPa, ρ_a = 11 kg/m^3

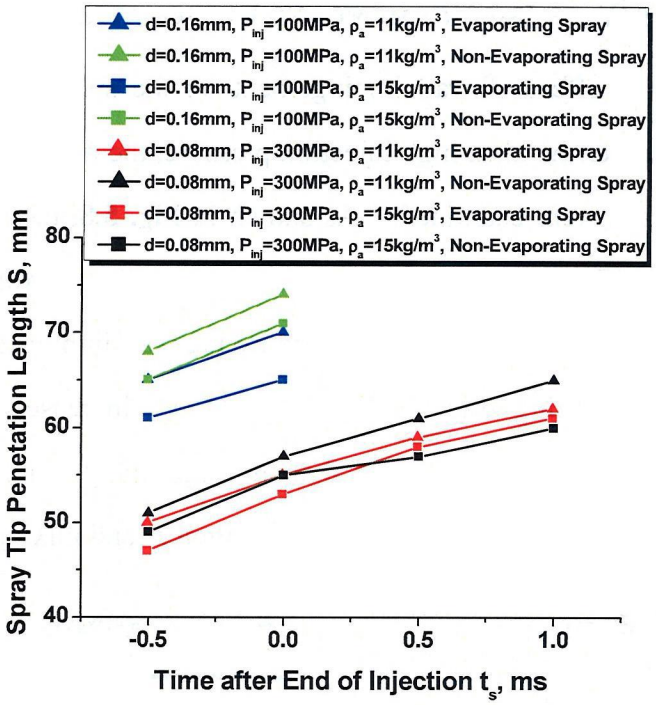

Figure 5.9 Spray tip penetration length, flat wall impinging sprays, non-evaporating and evaporating conditions, d = 0.08 & 0.16 mm, P_{inj} = 100 & 300 MPa, ρ_a = 11 & 15 kg/m^3

same time, the smaller initial droplets and stronger spray/wall interactions may change the secondary atomization process, thus resulting in an increase in the entrainment rate.

Since the fuel evaporation plays an important role in the mixture formation process, the experiments were carried out under both atmospheric and elevated conditions to clarify the effect of fuel evaporation (**Fig. 5.9**). The spray tip penetration length is generally decreased by fuel evaporation at almost all conditions. It is caused by the mixing process between the vapor fuel and ambient gas. As discussed previously, an increase in the ambient pressure would reduce the penetration by enhancing the atomization, spray dispersion, and air entrainment. At the same time, an increase in the ambient temperature would enhance the vaporization and slightly decrease the penetration. In **Fig. 5.9**, for two nozzles within the injection duration, it can be found that the decrease in penetration slightly reduces when ruling out the evaporation effect. For 0.08 mm nozzle after EOI, the penetration length increases most slowly under the non-evaporating condition with the higher ambient density. Increasing the

ambient density may change the processes of the secondary breakup, spray dispersion, and air entrainment. In addition, the wall wetting effect may play an important role under the non-evaporating condition, thus resulting in a further decease in the penetration length.

5.4 DISCUSSION ON MIXING RATE

In order to compare the performance of different nozzles under different conditions, statistical methods were employed to analyze the experimental results. There are several representative quantities and measures in the statistics (Nelson et al., 2003). Three of them were selected to describe the exprimental data in a more understandable form. The first one was the probability function that was used to present the fuel mass distribution within the spray plumes (**Eq. 5.1**). The second one was the overall equivalence ratio of total fuel that was the arithmetic mean of a set of data (**Eq. 5.2**). The third one was the inter-quartile range (IQR) that was a measure of spread and was equal to the difference between the upper quartile and lower quartile. The physical meaning of IQR was the range of the central 50% of total fuel in the probability distribution graph. To analyze the influence of different parameters on the mixing process, a measure of mixing rate (MR), defined by **Eq. 5.3**, was introduced. **Figure 5.10** shows an example how to calculate the mixing rate. MR from -0.5 to 0 msAEOI was equal to the IQR change during this 0.5 ms (IQR_1-IQR_2) divided by the IQR at -0.5 msAEOI (IQR_1) and multiplied by 100%.

$$f(\phi_i) = P(\Phi = \phi_i) = \frac{M_{f\Delta\phi}}{M_f} \tag{5.1}$$

$$\bar{\phi} = \sum_i \phi_i \cdot f(\phi_i) \tag{5.2}$$

$$MR = \frac{IQR_1 - IQR_2}{IQR_1} \times 100\% \tag{5.3}$$

where ϕ_i : equivalence ratio of total fuel

ϕ_0 = 0.06, $\Delta\phi$ = 0.01

$\overline{\phi}$: overall equivalence ratio

M_f : mass of total injected fuel, mg

$M_{f\Delta\phi}$: fuel mass at the range of $\Delta\phi$, mg

MR: mixing rate, %

IQR_i: inter-quartile range at certain timing

The probability distribution and overall equivalence ratio were calculated based on the experimental results using the method described above and are shown in **Fig. 5.11**. With the time elapsed, the vertical lines that stand for the overall equivalence ratios translate continuously to the leaner region. At the same time, the range of probability distribution curve decreases and the peak value increases. This indicates that large part of fuel falls in the range of low equivalence ratios.

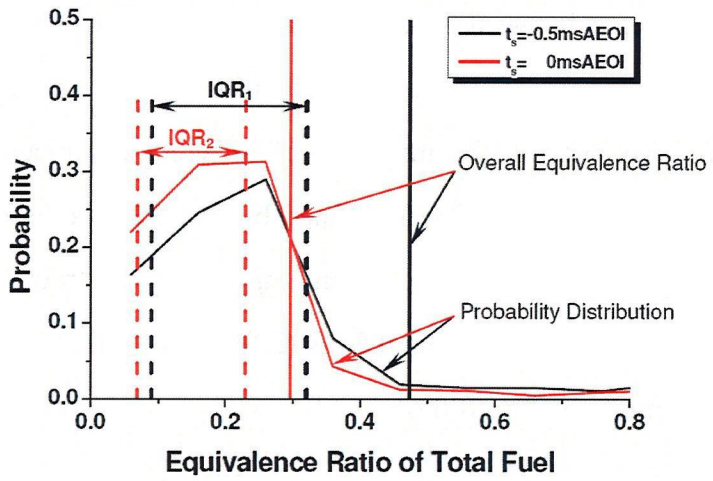

Figure 5.10 Example for mixing rate calculation, d = 0.08 mm, Pinj = 300 MPa, ρ_a = 11 kg/m^3, t_s = -0.5 & 0 msAEOI

Figure 5.12 shows the influence of the high injection pressure and ambient gas density on the overall equivalence ratio. It is obvious that the overall equivalence ratio decreases greatly with increasing the injection pressure from 100 to 300 MPa. Within the injection duration, the mixture is very rich for the micro-hole nozzle at the pressure of

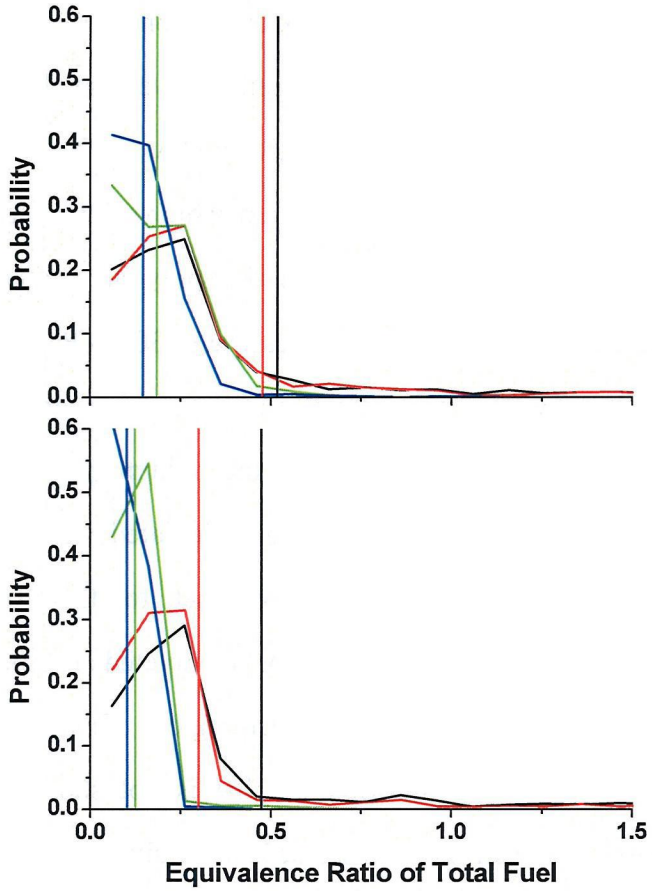

Figure 5.11 Probability distribution of fuel mass and overall equivalence ratio at various laser Shot timings, d = 0.08 mm, P_{inj} = 100 & 300 MPa, ρ_a = 11 kg/m^3

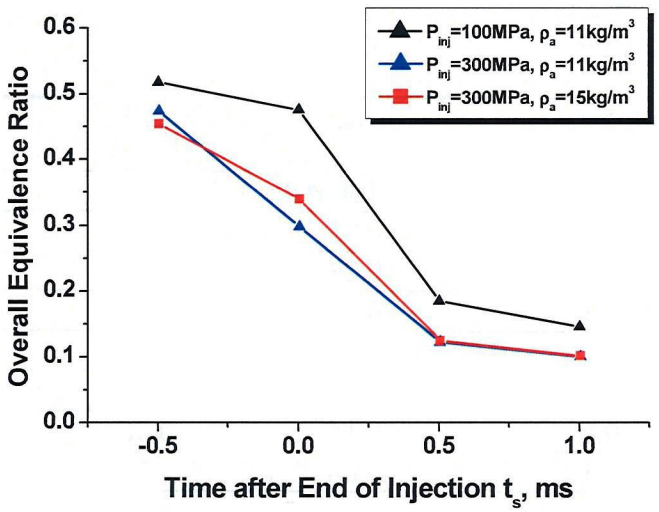

Figure 5.12 Overall equivalence ratio versus time after end of injection, d = 0.08 mm, P_{inj} = 100 & 300 MPa, ρ_a = 11 & 15 kg/m^3

100 MPa. After the end of injection, the mixture becomes fuel-lean very fast. This shows that although the micro-hole nozzle can generate very small initial droplets at the dense core region, the mixing process was relatively slow at the low injection pressure. This may be caused by the low spray momentum which results in the slow mass and momentum transport in the mixing layer between the spray plume and ambient gas.

Since the two curves for the injection pressure of 300 MPa are almost the same in **Fig. 5.12**, it is difficult to evaluate the influence of the ambient gas density. Therefore, the mixing rate (MR) is introduced to analyze the mixture preparation process. The inter-quartile ranges (IQR) at different timings and calculated MR are listed in **Table 5.3**. Comparison of these three groups of data shows that, for the two cases at the high injection pressure, the mixing processes are almost completed after 0.5 msAEOI. MR = 0 means that almost all fuel locates in the very lean region. In addition, from **Table 5.3**, it can be found that some useful information that is not shown in **Fig. 5.12**. The maximum mixing rates of the first two cases at low density are reached after the end of injection (0 ~ 0.5 msAEOI), whereas that of the third case at high density is reached before the end of injection (-0.5 ~ 0 msAEOI). This indicates that the ambient gas with high density is effective to accelerate the mixing process. It may be caused by two

Table 5.3 Mixing Rate (MR) & Inter-Quartile Range (IQR)

Time Interval (msAEOI)	IQR_1	IQR_2	MR (%)
0.08mm, 100MPa, 11kg/m^3			
-0.5 ~ 0	0.25	0.23	8
0 ~ 0.5	0.23	0.15	35
0.5 ~ 1	0.15	0.1	33
0.08mm, 300MPa, 11kg/m^3			
-0.5 ~ 0	0.23	0.16	30
0 ~ 0.5	0.16	0.08	50
0.5 ~ 1	0.08	0.08	0
0.08mm, 300MPa, 15kg/m^3			
-0.5 ~ 0	0.31	0.15	52
0 ~ 0.5	0.15	0.08	47
0.5 ~ 1	0.08	0.08	0

reasons: (1) the high pressure gas exerts a strong aerodynamic force upon the turbulent mixing layer between the spray plume and ambient gas, which enhances the secondary breakup of the fuel droplets and increases the turbulent mixing rate; (2) the high temperature enhances the fuel vaporization process, which results in a decrease in the local equivalence ratio.

Table 5.4 Experimental conditions for evaporating sprays impinging on a flat wall

Ambient Gas Density (kg/m^3)	11 (-20 deg.ATDC)	
Ambient Gas Pressure (MPa) /Temperature (K)	2.6/797	
Spray Type	Flat Wall Impinging Spray	
Injection Pressure (MPa)	100	300
Nozzle Hole Diameter (mm)	0.16	0.08
Injection Quantity (mg)	15.47	3.87
Injection Duration (ms)	2.2	1.3
Laser Timing (msAEOI)	-2.1, -2.05, -2.0, -1.8, -1.5, -1.2, -0.9	-1.15, -1.1, -1.05, -1.0, -0.9, -0.6, -0.3, 0

5.5 DISCUSSION ON EVOLUTION OF SPRAY PLUMES

Previous experiments are mainly focusing on the period around EOI. To get a better understanding of the evolution of spray plumes and to provide detailed information for calibration of the predicative spray models, further experiments were carried out from SOI with very short intervals. Experimental conditions are listed in **Table 5.4**. The baseline condition (d = 0.16 mm and P_{inj} = 100 MPa) and objective condition (d = 0.08 mm and P_{inj} = 300 MPa) were tested from the timing close to SOI.

The evolution of spray plumes is shown in **Figs 5.13** and **5.14** using optical thickness images of both liquid and vapor phases. It is obvious that, for the two test cases, the wall impingement occur at -2.05 and -1.1 msAEOI respectively. As described previously, the optical thickness gradient shows the concentration distribution. With

focusing on the timings around the wall impingement, the penetration lengths of liquid and vapor phases, gas entrainment rate, and fuel vaporization rate will be discussed in this section.

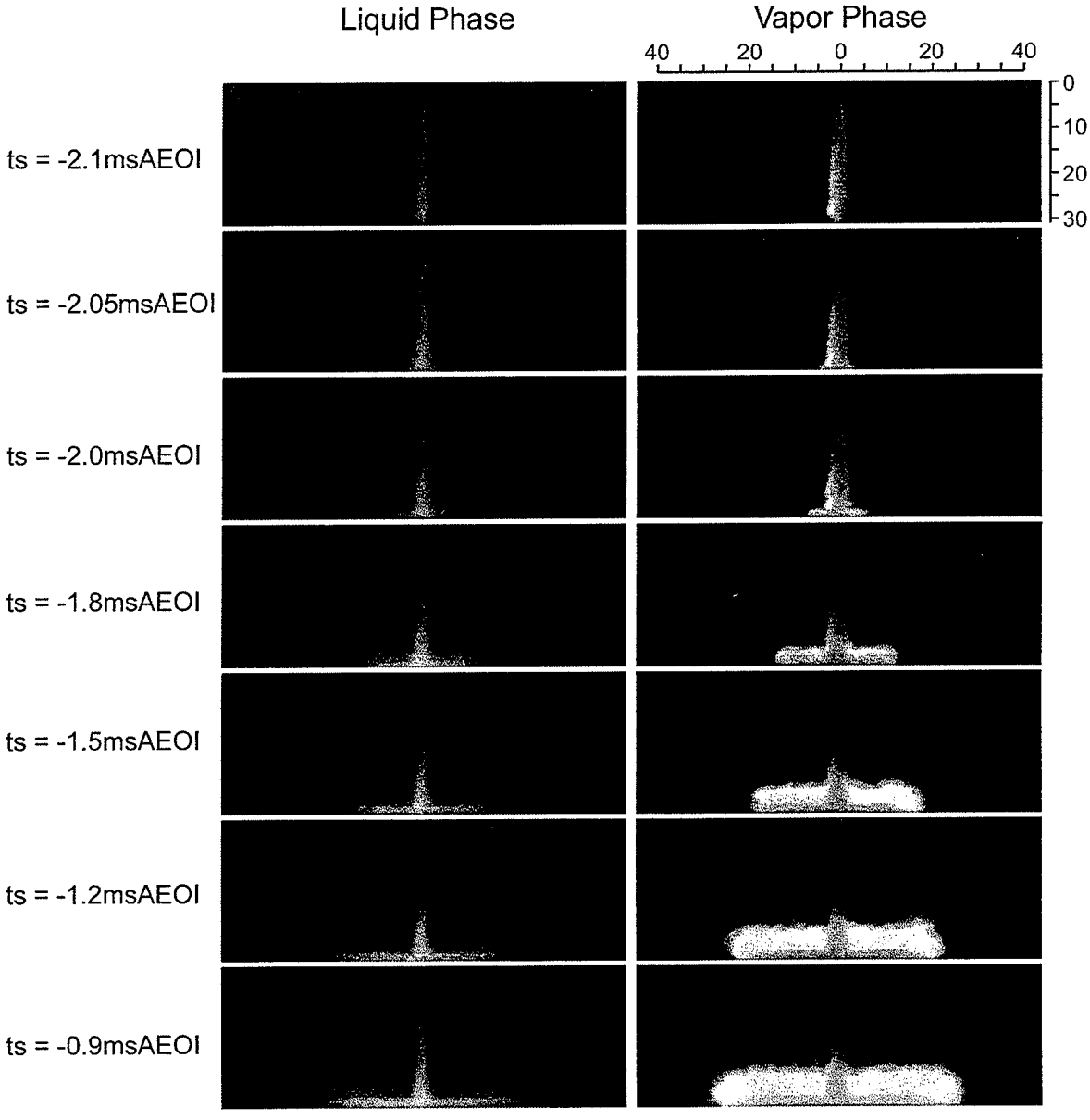

Figure 5.13 Evolution of flat wall impinging sprays, d = 0.16 mm, P_{inj} = 100 MPa, ρ_a = 11 kg/m^3

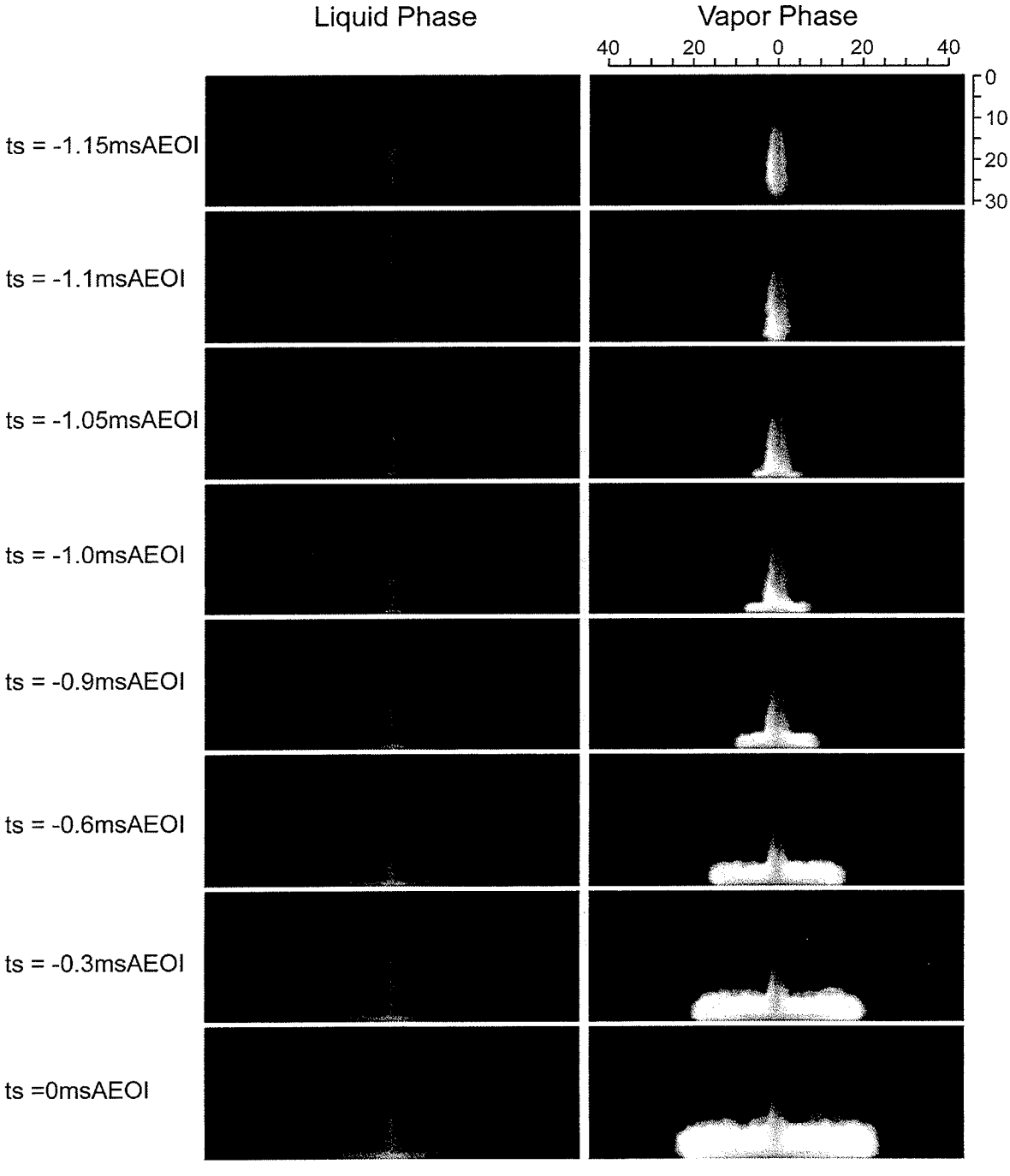

Figure 5.14 Evolution of flat wall impinging sprays, d = 0.08 mm, P_{inj} = 300 MPa, ρ_a = 11 kg/m^3

5.5.1 Penetration Lengths of Liquid and Vapor Phases Fuel

In the previous sections, only the spray tip penetration length, defined as a measure of the furthest location of a spray plume, was discussed. However, for evaporating sprays, the penetration lengths of both liquid and vapor phases fuel should be

considered separately. Especially for small bore D.I. Diesel engines, to reduce wall wetting effect and to control emissions, the design of combustion chambers required detailed information on the liquid phase penetration length.

The vapor phase penetration length is a measure of the furthest location of the vapor phase fuel. Since it is difficult to determine the exact boundary of the liquid phase in an evaporating spray, three lengths were measured with different liquid phase equivalence ratios (Φ_{Liquid} = 0.1, 0.5, and 1.0) to examine the experimental results. **Figure 5.15** shows the penetration lengths of liquid and vapor phases. It can be found that, within the injection duration, the spray tip penetration lengths for liquid and vapor phases (Φ_{Liquid} = 0.1 and Φ_{Vapor} = 0.1) increase continuously and the tendency is similar to each other. On the contrary, the penetration length with a larger equivalence ratio, for instance, the curves of Φ_{Liquid} = 1.0 in **Figs 5.15(a)** and **(b)**, reaches a steady value within very short time after SOI, which presents a slight difference for two test conditions. Therefore, Φ_{Liquid} = 0.1 and 1.0 cannot be used to determine the liquid phase penetration. However, the curve of Φ_{Liquid} = 0.5, which is different from the curve of Φ_{Vapor} = 0.1 and is dependent on the test conditions, can be used as the boundary of the liquid phase fuel.

As discussed above, in this research, the curve of Φ_{Liquid} = 0.5 was used to determined the liquid phase penetration length. In **Fig. 5.15**, it can be found that, for 0.16 mm nozzle, the liquid phase penetration length increase continuously. It indicates that, within the injection duration, the air-fuel mixture is enriched by the injected fuel and the entrainment and vaporization are not strong enough to disperse the liquid phase fuel. However, for the 0.08 mm nozzle, the liquid phase penetration length increases slightly after the wall impingement occurs. This indicates that, for 0.08 mm and 300 MPa, there is a balance between the increase in the injected fuel and the decrease in the liquid phase fuel caused by mixing and vaporization.

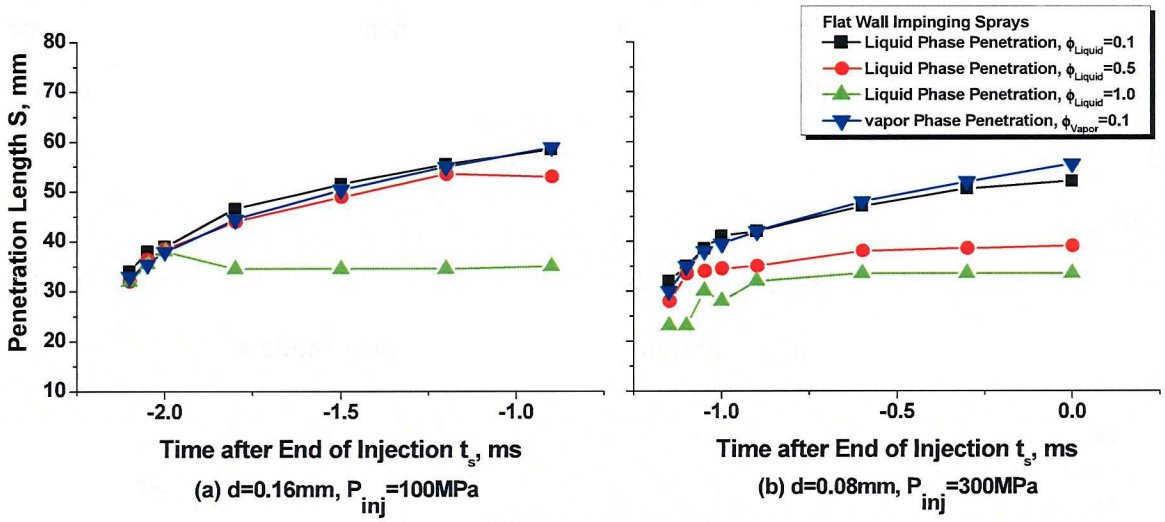

Figure 5.15 Penetration lengths of liquid and vapor phases, flat wall impinging sprays, ρ_a = 11 kg/m^3, (a) d = 0.16 mm, P_{inj} = 100 MPa, (b) d = 0.08 mm, P_{inj} = 300 MPa

5.5.2 Gas Entrainment Rate and Fuel Vaporization Rate

The characteristics of the gas entrainment and fuel vaporization are shown in **Figs 5.14** and **5.15**. M_a/M_f increases continuously for the two test cases, although it increases obviously faster for 0.08 mm and 300 MPa. The initial value of M_a/M_f for 0.08 mm and 300 MPa is about three times as large as that for 0.16 mm and 100 MPa. After the wall impingement, there is no obvious change in the tendency of M_a/M_f. In addition, as shown in **Fig. 5.15**, the initial value of M_v/M_f for 0.08 mm and 300 MPa is also about three times as large as that for 0.16 mm and 100 MPa. After the wall impingement, M_v/M_f decreases first and then increases. This tendency is more significant for 0.08 mm and 300 MPa.

Above results show that, for the conventional nozzle at the low injection pressure, both of the gas entrainment rate and fuel vaporization rate are much lower when compared to the micro-hole nozzle at the ultra-high injection pressure. This indicates that the reduced initial droplet size and increased spray momentum can intensify the primary breakup process and can enhance the entrainment and vaporization. The baseline case of 0.16 mm and 100 MPa is influenced more greatly by the wall

impingement. After the impingement, both the entrainment and vaporization become slower. However, for 0.08 mm and 300 MPa, with maintaining relatively high M_v/M_f, the spray momentum is still high enough to entrain sufficient ambient gas into the spray plume.

The detailed evolution of the flat wall impinging sprays may provide useful information for developing and calibrating the predicative spray models.

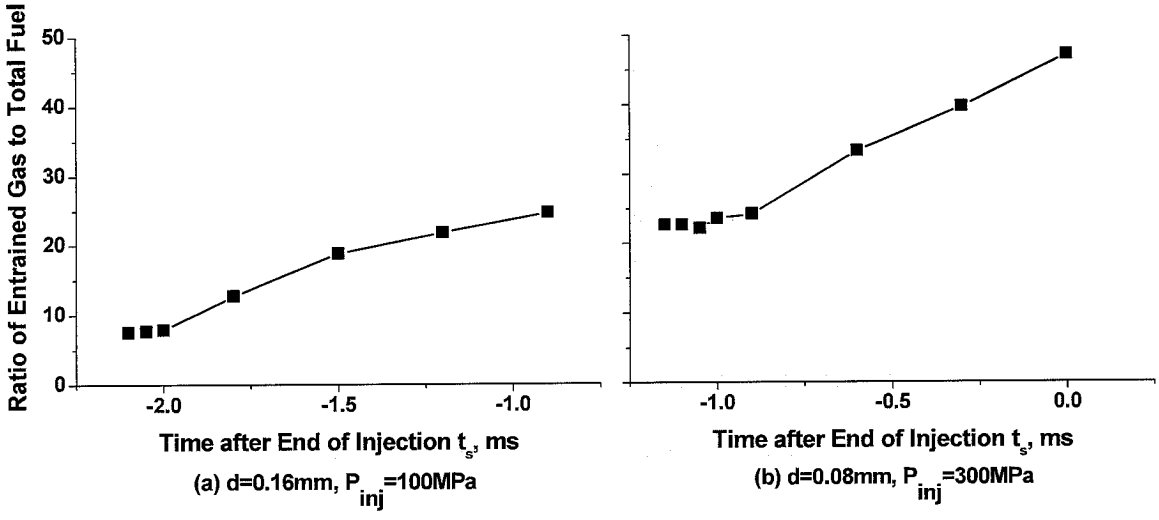

Figure 5.16 Ratio of entrained gas to total fuel, flat wall impinging sprays, ρ_a = 11 kg/m^3, (a) d = 0.16 mm, P_{inj} = 100 MPa, (b) d = 0.08 mm, P_{inj} = 300 MPa

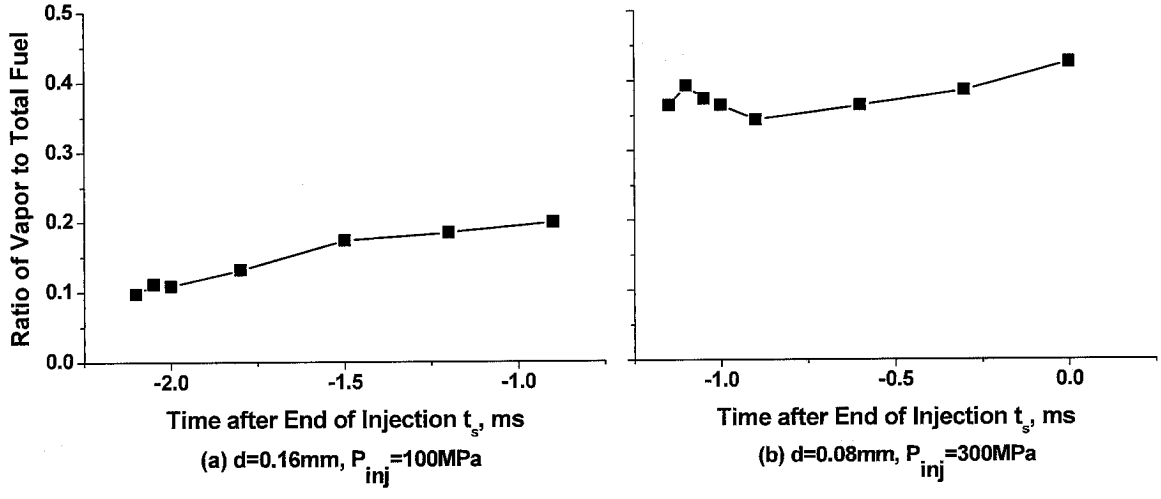

Figure 5.17 Ratio of vapor phase fuel to total fuel, flat wall impinging sprays, ρ_a = 11 kg/m^3, (a) d = 0.16 mm, P_{inj} = 100 MPa, (b) d = 0.08 mm, P_{inj} = 300 MPa

5.6 DISCUSSION ON WALL-IMPINGING GAS JET THEORY

In this subsection, the measured penetration length is compared with the predicted results using analytical method based on the wall-impinging gas jet theory. Since the physical process of Diesel sprays is not well understood, an approximation using gas jets has been accepted in a wide range for a long time. The expressions for wall-impinging jet penetration used here were derived by Glauert (1956) and Poreh et al. (1967). Song and Abraham (2003) modified the expressions and proposed a set of constants which predicted the penetration length in good agreement with the results measured by Fujimoto et al. (1997). The equation for the jet tip position can be expressed as (Song and Abraham, 2003)

$$S_{Radial}^{1-m} = (1-m)C_f F_m \left(K \frac{\rho_f}{\rho_a} \right)^{1/2} L^{-(1+m)} (\tau + t) \tag{5.4}$$

The kinematic momentum flux, K, can be calculated from the momentum of the jet, J, by the following equation (Schlichting, 1979)

$$K = J/\rho_f = C_a \pi d^2 U_0^2 / 4 \tag{5.5}$$

The injection velocity at the nozzle hole exit, U_0, is given by Bernoulli's equation

$$U_0 = C_v \sqrt{2(P_{inj} - P_a)/\rho_f} \tag{5.6}$$

The discharge coefficient, C_d= 0.9, is determined experimentally and the area-contraction coefficient, C_a, is assumed to be 0.95. Therefore, the coefficient of velocity can be calculated by $C_v = C_d / C_a$ (Siebers, 1999).

The constants used in **Eq. (5.4)**, F_m= 1.11, m = -1.12, and C_f= 0.305, are based on the study of Witze and Dwyer (1976) and as recommended by Song and Abraham (2003).

Figure 5.18 shows the measured penetration length and predicted results for 0.16 and 0.08 mm nozzles. Note that the predicted curves are almost proportional to the experimental results. It obviously shows that the gas jet theory can predict the tendency

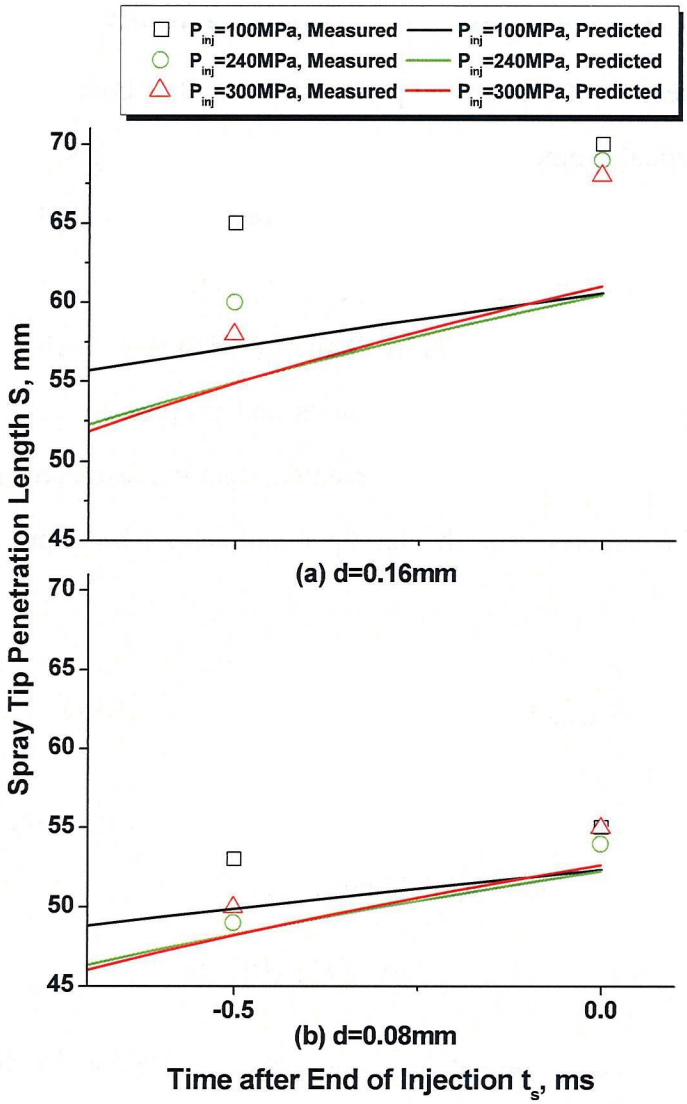

Figure 5.18 Comparison of measured and predicted results of spray tip penetration length, d = 0.08 & 0.16 mm, P_{inj} = 100, 240, and 300 MPa, ρ_a = 11 kg/m^3

of the Diesel sprays but may underestimate the penetration length for all test conditions. In addition, it is found that the difference between the measured and predicted results decreases with decreasing the nozzle hole diameter. This shows that, for the two-phase wall-impinging case, the spray formed by micro-hole nozzles is more similar to the gas jet. This can be explained by the previous experimental results. For the 0.08 mm nozzle, much smaller initial droplets are generated. At the same time, the gas entrainment rate and fuel vaporization rate are significantly high from the start of

injection. These results show that the characteristics of the spray from the micro-hole nozzle are more similar to those of a single-phase gas jet.

In addition, it can be concluded that the constants proposed by Song and Abraham (2003) should be adjusted when applied to the Diesel sprays. The agreement can be improved by changing the constants in **Eq. (5.4)**, but the optimal values should be determined and verified by a large amount of experimental data.

5.7 SUMMARY

Measurements were made of the Diesel sprays impinging on a flat wall. The impingement distance was held constant. Three parameters, the injection pressure, nozzle hole diameter, and ambient density, were varied to investigate the overall structure, gas entrainment, fuel vaporization, and evolution of the spray plumes. The spray characteristics of the micro-hole nozzles under ultra-high injection pressures were focused on. Findings are summarized as follows.

1. Micro-hole nozzles are effective to reduce the spray tip penetration length and adhered fuel film on the wall surface, which was useful for PCI combustion to control hydrocarbon emissions.
2. The ultra-high injection pressure can provide enough energy for micro-hole nozzles to maintain a high spray momentum close to EOI, whereas the conventional injection pressure (100 MPa) is not high enough and may cause the mixing process to deteriorate.
3. The 0.08 mm nozzle had much better characteristics than the 0.10 mm nozzle. At the same conditions, the 0.08 mm nozzle had the shorter penetration length with a similar gas entrainment rate.
4. The contour of $\Phi_{Liquid} = 0.5$ can be used as the boundary of the liquid phase fuel. Under the evaporating conditions, the liquid phase penetration length is dependent on the nozzle hole diameter. With the evolution of the spray plumes, this length will reach a steady state.

5. By examining the first stage of the injection duration, it is found that, for the micro-hole nozzle under the ultra-high injection pressure, both vaporization and entrainment are significantly high. The combination of micro-hole nozzle and ultra-high injection pressure may change the primary breakup mechanism.
6. Around the impingement timings, there are no pronounced changes in gas entrainment (M_a/M_f), whereas the fuel vaporization (M_v/M_f) decreases obviously after the wall impingement.
7. M_v/M_f increases from the start of injection, decreases after the wall impingement, and then increases slightly until the end of injection.
8. Comparison of measured and predicted penetration length results showed that gas jet theory could be used to simulate Diesel sprays approximately. The sprays formed by the micro-hole nozzle were more similar to the gas jets than those formed by the conventional nozzles were. To achieve good agreement, the experimentally determined constants should be carefully selected and verified.

Chapter 6 Sprays Impinging on a 2-D Piston Cavity Shape Wall

6.1 EXPERIMENTAL CONDITIONS

The shape of the combustion chamber is critical for the design of Diesel engines. To clarify the effect of the chamber shape on the spray and mixture formation process, Diesel sprays impinging on a 2-D piston cavity shape wall were investigated using the LAS technique. **Figure 6.1** shows the schematic diagram of two combustion chambers. The shallow dish type chamber was used as the baseline condition, and the reentrant type chamber was the objective one. Since 18 nozzle holes were arranged in zigzag shape, there are two spray umbrella angles (120 and 150 deg.) for the engine condition. The ambient condition in the constant volume vessel was the same as the real engine condition at the crank angle of -20 deg.ATDC.

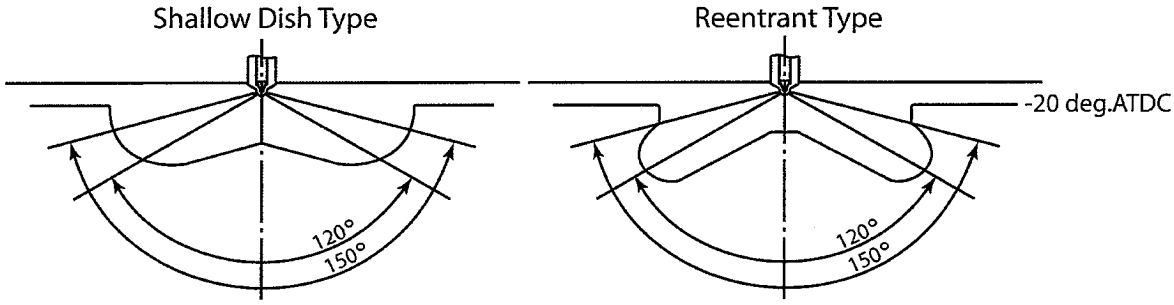

Figure 6.1 Schematic diagram of combustion chambers and spray umbrella angles

To employ a line-of-sight technique, 2-D piston cavity shape impingement wall should be used in this work. The schematic diagram of 2-D piston cavity shape impingement wall for reentrant type chamber is shown in **Fig. 6.1**. The upper metal block was used to simulate the reentrant type chamber wall, and the lower wedge-shape block was used to adjust the spray umbrella angle and impingement distance. All parameters were determined in terms of the operating conditions in a prototype engine. The detailed experimental conditions are shown in **Tables 6.1** and **6.2**. The impingement distances from the nozzle tip to the impingement point for four test conditions are shown in **Table 6.3**. The values used in this work are the same as those

used in the real engine test. The effects of the injection pressure, nozzle hole diameter, spray umbrella angle, and piston cavity shape on the spray and mixture formation process will be discussed in this chapter.

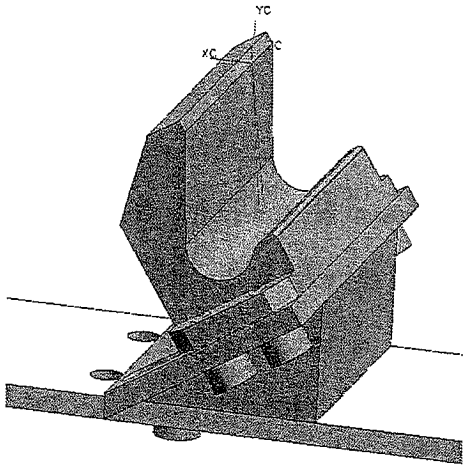

Figure 6.2 2-D piston cavity shape impingement wall for reentrant type chamber

Table 6.1 Experimental conditions for 2-D piston cavity shape wall impinging spray, shallow dish type wall

Ambient Gas Density (kg/m^3)	11 (-20 deg.ATDC)			
Ambient Gas Pressure (MPa) /Temperature (K)	2.6/797			
Spray Type	2-D Piston Cavity Shape Wall Impinging Spray: Shallow Dish Type Wall			
Injection Pressure (MPa)	100	100	300	
Spray Umbrella Angle (deg.)	150	150	150	120
Nozzle Hole Diameter (mm)	0.16	0.08		
Injection Quantity (mg)	15.47	3.87		
Injection Duration (ms)	2.2	2.2	1.3	
Laser Timing (msAEOI)	-2.05, -2.0, -1.95 -1.8, -1.5, -1.2, -0.9, -0.6, -0.3, 0	-2.0, -1.9, -1.8, -1.5, -1.2, -0.9, -0.6, 0.3, 0, 0.3, 0.6, 0.9	-1.1, -1.05,-1.0, -0.9, -0.6, -0.3, 0, 0.3, 0.6, 0.9	

Table 6.2 Experimental conditions for 2-D piston cavity shape wall impinging spray, reentrant type wall

Ambient Gas Density (kg/m^3)	11 (-20 deg.ATDC)		
Ambient Gas Pressure (MPa) /Temperature (K)	2.6/797		
Spray Type	2-D Piston Cavity Shape Wall Impinging Spray: Reentrant Wall		
Injection Pressure (MPa)	100	300	
Spray Umbrella Angle (deg.)	150	150	120
Nozzle Hole Diameter (mm)	0.16	0.08	
Injection Quantity (mg)	15.47	3.87	
Injection Duration (ms)	2.2	1.3	
Laser Timing (msAEOI)	-2.05, -2.0, -1.95, -1.8, -1.5, -1.2, -0.9, -0.6, -0.3, 0	-1.1, -1.05, -1.0, -0.9, -0.6, -0.3, 0, 0.3, 0.6, 0.9	

Table 6.3 Impingement distances from nozzle tip to impingement point for four test conditions

Wall Type	Spray Umbrella Angle (deg.)	Impingement Distance (mm)
Shallow Dish	150	37
Shallow Dish	120	34
Reentrant	150	31
Reentrant	120	39

6.2 EFFECTS OF NOZZLE HOLE DIAMETER AND INJECTION PRESSURE

The optical thickness images of liquid and vapor phases for the baseline condition (shallow dish type wall, d = 0.16 mm, P_{inj} = 100 MPa, ρ_a= 11 kg/m^3) are shown in **Fig. 6.3**. It shows that the wall impingement occurs at -2.0 msAEOI. Since there are more free surfaces in the left region, more fuel dispersed into this region and more ambient gas is entrained. By examining the optical thickness images, it can be found that large part of liquid phase fuel is located on the wall surface, whereas large part of vapor phase fuel

accumulates in the left tip region. The black region in the images of vapor phase fuel indicates a very strong liquid droplet scattering effect. As described in Chapter 3, the mass distributions per unit projected area can be obtained using the method of data processing for non-axisymmetric sprays. **Figure 6.4** shows the mass distributions of fuel and vapor phases fuel at three timings (t_s = -2.0, -0.9, and 0 ms AEOI). It can be found that, after the wall impingement, the richest vapor phase appears in the left spray tip region. The reduced gradient at the spray tip indicates that the vapor phase fuel

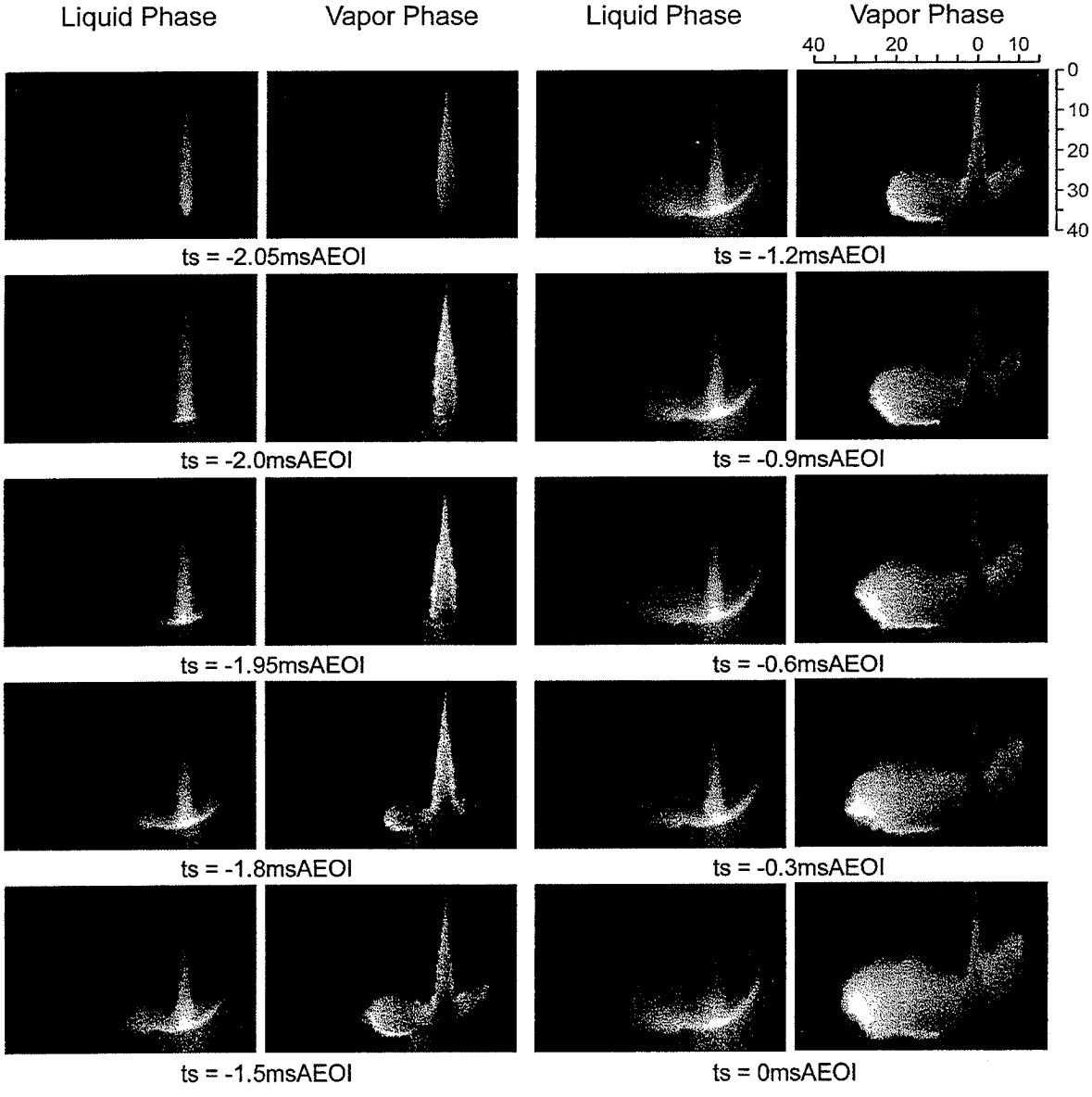

Figure 6.3 Optical thickness images of liquid and vapor phases, shallow dish type wall, d = 0.16 mm, P_{inj} = 100 MPa, ρ_a = 11 kg/m^3

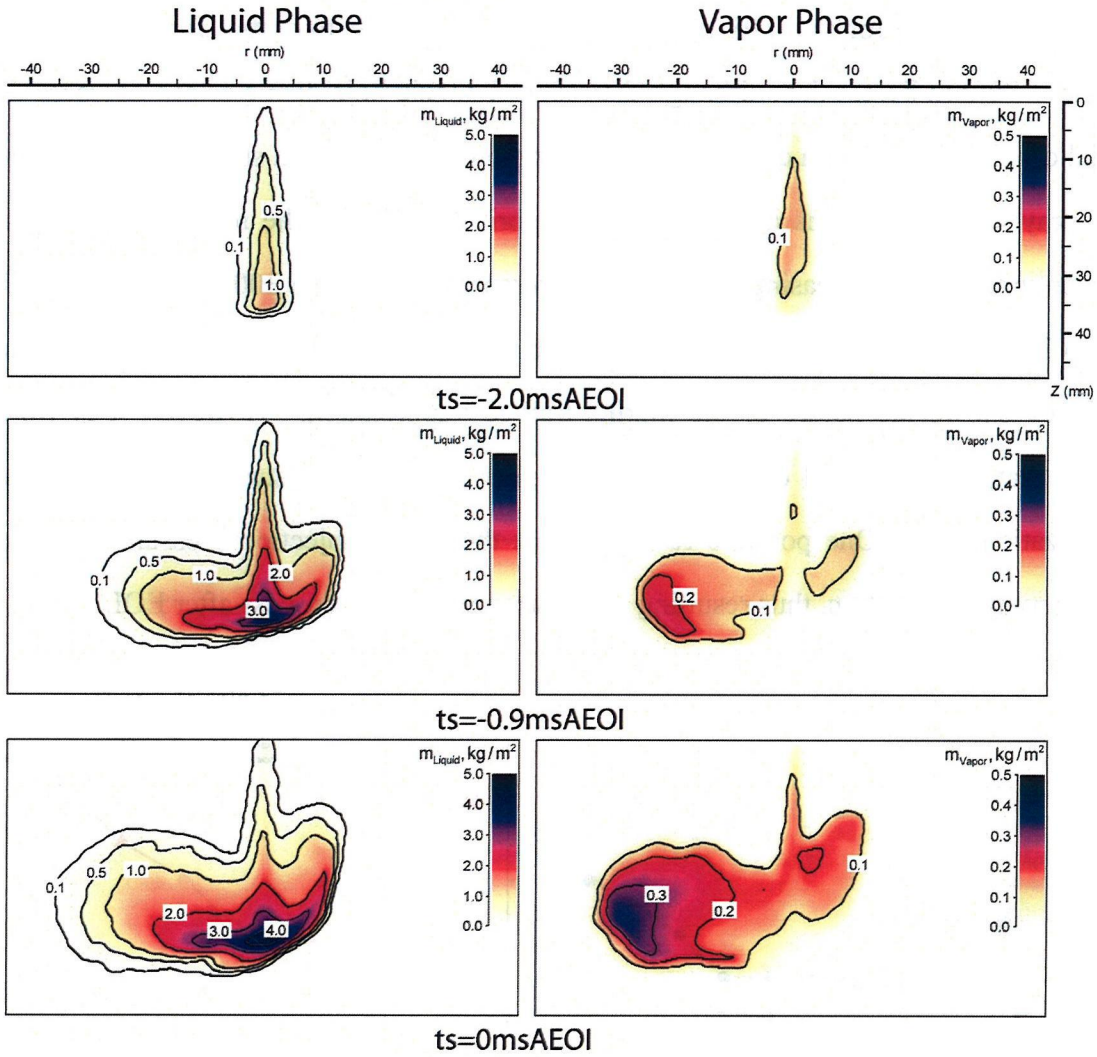

Figure 6.4 Mass distributions per unit projected area of fuel and vapor phases fuel at three timings (t_s = -2.0, -0.9, and 0 ms AEOI)

accumulates continuously in that region within the injection duration. However, for the liquid phase fuel, the richest part remains in the region close to the wall surface. This means that the wall wetting effect is very strong for 2-D piston cavity shape wall impinging sprays.

Comparison of three test cases for the shallow dish type wall impinging sprays is shown in **Fig. 6.5**. After the wall impingement, for three cases, M_v/M_f, with the similar tendency, decreases first and then increases slightly. After the end of injection, the vaporization becomes much faster. With decreasing the nozzle hole diameter, as shown in **Fig. 6.5(a)**, the initial fuel vaporization rate increases significantly. However, the

decrease in M_v/M_f for the 0.08 mm nozzle is much greater than that for the 0.16 mm nozzle. This indicates that, although the reduced nozzle hole diameter can decrease the initial droplet size and can enhance the vaporization rate at the first stage of the injection, the spray/wall interactions inhibit the fuel vaporization due to the relatively low spray momentum. With increasing the injection pressure from 100 to 300 MPa, as shown in **Fig. 6.5(b)**, the curve translates upwards without changing the tendency. This constant tendency shows the nature of the mixing-limited vaporization. However, it is worth noting that, after the end of injection, the higher injection pressure results in a faster vaporization rate. One possible reason is that the higher injection pressure generates higher spray momentum, thus resulting in the stronger mixing process after EOI.

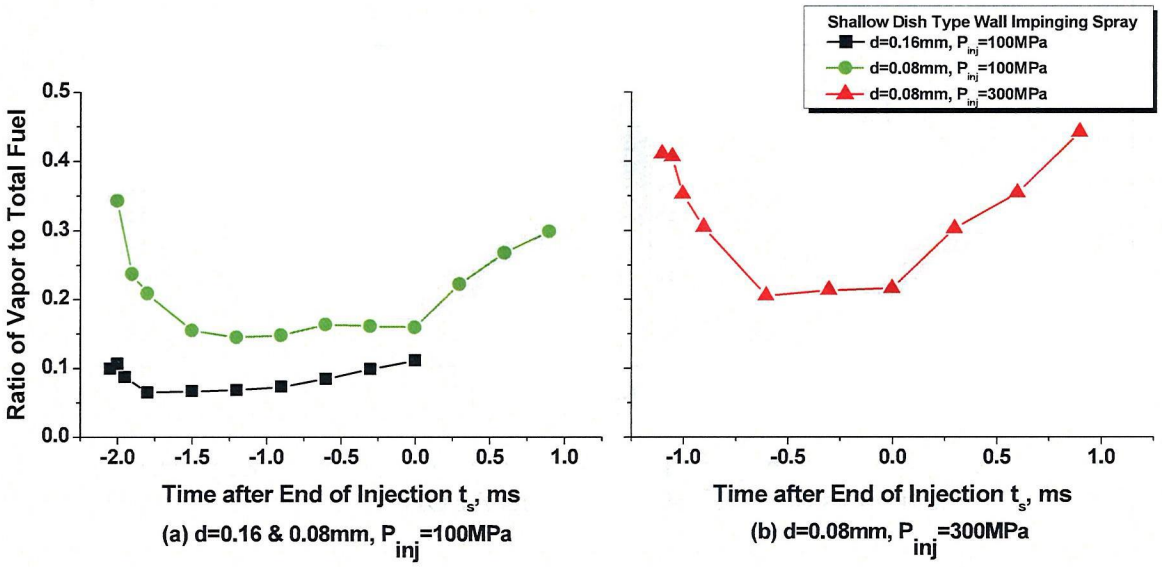

Figure 6.5 Ratio of vapor to total fuel versus time after EOI, shallow dish type wall, ρ_a = 11 kg/m^3, (a) d = 0.16 & 0.08 mm, P_{inj} = 100 MPa, (b) d = 0.08 mm, P_{inj} = 300 MPa

6.3 EFFECTS OF PISTON CAVITY SHAPE AND SPRAY UMBRELLA ANGLE

Figure 6.6 shows the ratio of vapor to total fuel for two piston cavity shapes. M_v/M_f for the 0.16 mm nozzle is only slightly influenced by the piston cavity shape. For the 0.08 mm nozzle, the initial value of M_v/M_f increases obviously. It may be caused by the reduced impingement distance (from 37 to 31 mm). At this initial stage,

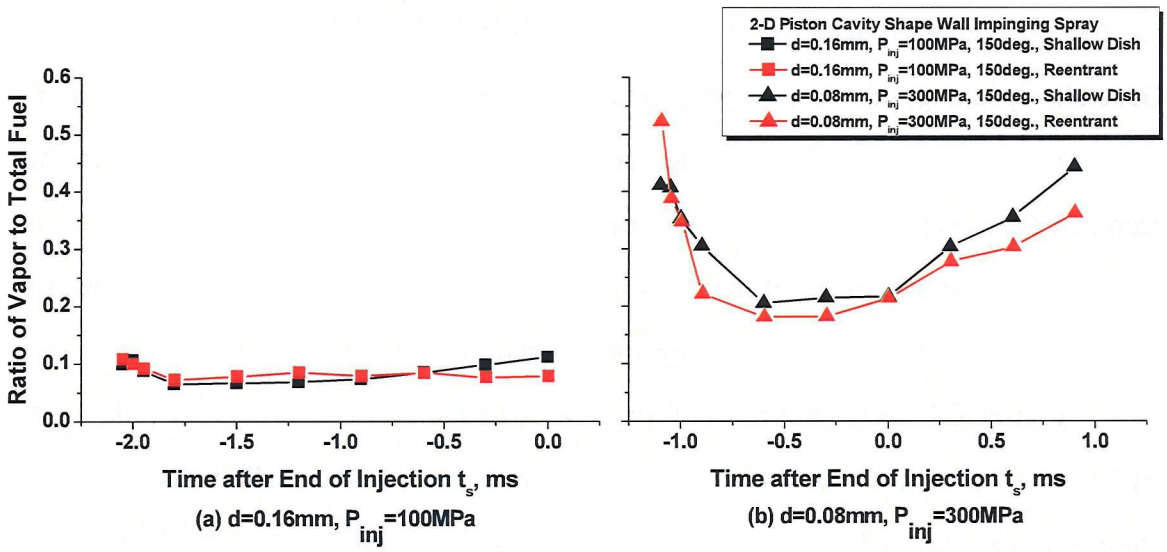

Figure 6.6 Ratio of vapor to total fuel versus time after EOI, shallow dish and reentrant type walls, ρ_a = 11 kg/m^3, (a) d = 0.16, P_{inj} = 100 MPa, (b) d = 0.08 mm, P_{inj} = 300 MPa

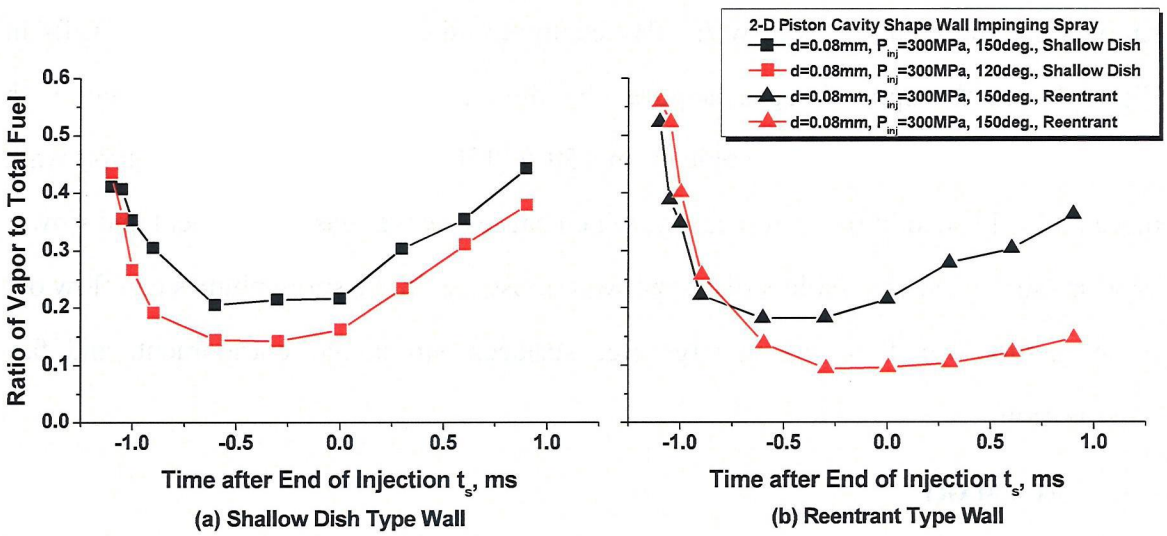

Figure 6.7 Ratio of vapor to total fuel versus time after EOI, spray umbrella angle = 150 & 120 deg., d = 0.08 mm, P_{inj} = 300 MPa, ρ_a = 11 kg/m^3, (a) shallow dish type wall, (b) reentrant type wall

the injected fuel mass is very small and the spray momentum is large enough to cause strong spray/wall interactions, thus resulting in faster vaporization. With greatly decreasing the impingement distance, this effect becomes more significant. However, with the evolution of the spray plume, more liquid fuel accumulates at the bottom of the

reentrant type cavity, the fuel vaporization is inhibited and M_v/M_f becomes smaller. Generally speaking, there are no pronounced influences of the piston cavity shape on the vaporization process under the quiescent condition. In the real engine, since the reentrant type chamber will generate a much stronger squish flow than the shallow dish type, it can be considered that the vaporization rate for the reentrant type chamber will become higher under the real engine operating conditions.

Figure 6.7 shows the ratio of vapor to total fuel for two spray umbrella angles with two piston cavity shape walls. It can be found that, for the shallow dish type wall, there is an obvious difference between two spray umbrella angles from the first stage of the injection duration (t_s = -1.0 ms AEOI). For the reentrant type wall, however, the difference becomes pronounced in the middle of the injection duration (t_s = -0.4 ms AEOI). It is obviously show that the influence of the spray umbrella angle is much stronger for the reentrant type wall. By examining the configurations of two walls in **Fig. 6.1** and the spray images acquired by the LAS system, it is found that, with decreasing the spray umbrella angle from 150 to 120 deg., for the reentrant type wall, more fuel is located in the piston cavity, which causes weaker gas entrainment and slower vaporization. For the shallow dish type wall, most fuel in the spray plumes can flow out of the cavity, which results in large free surfaces, strong gas entrainment, and fast vaporization.

6.4 SUMMARY

Measurements were made of the Diesel sprays impinging on 2-D piston cavity shape walls. Two kinds of cavity shapes, shallow dish type and reentrant type, were investigated. The baseline condition (d = 0.16 mm and P_{inj} = 100 MPa) was compared with the objective condition (d = 0.16 mm and P_{inj} = 100 MPa). The two spray umbrella angles were examined. Findings are summarized as follows.

1. M_v/M_f decreases first after the wall impingement, and then increases slightly until the end of injection. After EOI, for the objective condition, M_v/M_f increases significantly.

2. The influence of the spray umbrella angle on the vaporization process for reentrant type wall is much stronger than that for the shallow dish wall.
3. Under the quiescent condition, there are no obvious influences of the cavity shape on the vaporization process. The result indicates that it is possible to use the reentrant type combustion chamber that can generate a strong squish flow to obtain stronger entrainment and faster vaporization under the real engine condition.

Chapter 7 Sprays from a 2-Hole Nozzle

7.1 EXPERIMENTAL CONDITIONS

To investigate the interactions of two spray plumes and to correlate the results of single-hole nozzles and multi-hole nozzles, a 2-hole nozzle with a diameter of 0.08 mm was used in this research work. The configuration of the 2-hole nozzle is schematically shown in **Fig. 7.1**. The angle between the axes of two cylindrical holes is 23.7 deg., which is the same as that in a multi-hole nozzle. The experimental conditions are shown in **Table 7.1**. The measurements were made of the free spray, flat wall impinging spray, and 2-D piston cavity shape wall impinging spray. The laser timing started close to SOI, and the spray evolution within the injection duration was acquired using the LAS system. The non-axisymmetric analysis method was used to conduct the data processing. The mass distributions per unit projected area and fuel vaporization will be discussed in this chapter.

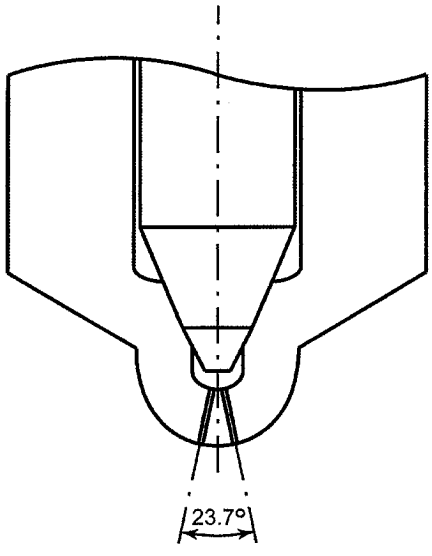

Figure 7.1 Configuration of 2-hole nozzle tip, d = 0.08 mm

Table 7.1 Experimental conditions for 2-hole nozzle, free spray, flat wall impinging spray, and 2-D piston cavity shape wall impinging spray

Ambient Gas Density (kg/m^3)	11 (-20 deg.ATDC)		
Ambient Gas Pressure (MPa) /Temperature (K)	2.6/797		
Injection Pressure (MPa)	300		
Nozzle Hole Diameter (mm)	0.08		
Injection Quantity (mg)	7.74		
Injection Duration (ms)	1.3		
Spray Type	Free Spray	Flat Wall Impinging Spray	2-D Piston Cavity Shape Wall Impinging Spray
Laser Timing (msAEOI)	-1.1, -1.05,-1.0, -0.9, -0.6, -0.3, 0	-1.1, -1.05,-1.0, -0.9, -0.6, -0.3, 0	-1.1, -1.05,-1.0, -0.8, -0.6, -0.3, 0

7.2 RESULTS AND DISCUSSION

Since 18 micro-holes in a multi-hole nozzle were arranged in a zigzag shape, it is important for the nozzle design to get a better understanding of the interactions between the spray plumes. **Figures 7.2** and **7.3** show the optical thickness images of the vapor phase fuel for the free spray, flat wall impinging spray, and 2-D piston cavity shape wall impinging spray. Note that, since it is impossible to make the same rounding shape for the inlets of two micro-holes, there is a slight difference between the spray characteristics of two spray plumes. In **Fig. 7.2(a)**, it can be found that there are no pronounced interactions between two spray plumes. For the flat wall impinging spray shown in **Fig. 7.2(b)**, however, at t_s = -0.9 msAEOI, the tips of the two spray plumes touch each other. The strong interactions result in an increase in the height of the wall jet in the center of the plumes. In the experiment of the 2-D piston cavity shape wall impinging spray, the nozzle was rotated a angle to simulate the spray in a real engine. This offset angle was 51 deg. By examining **Fig. 7.3**, it is found that the interactions between two plumes are stronger for the reentrant type wall. Most fuel is located at the bottom of the cavity.

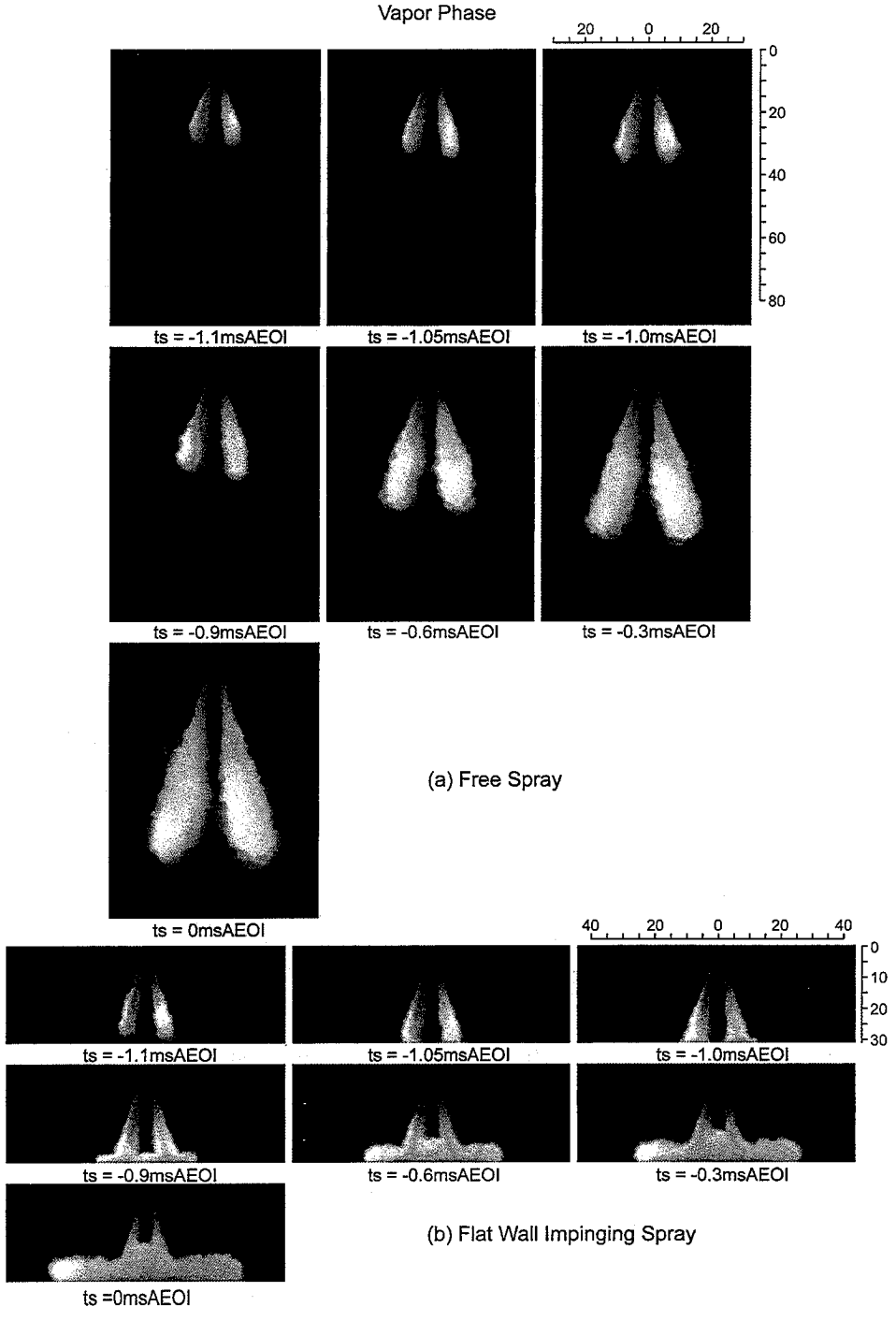

Figure 7.2 Optical thickness images of vapor phase fuel, sprays from a 2-hole nozzle, d = 0.08 mm, P_{inj} = 300 MPa, ρ_a = 11 kg/m^3, (a) free spray, (b) flat wall impinging spray

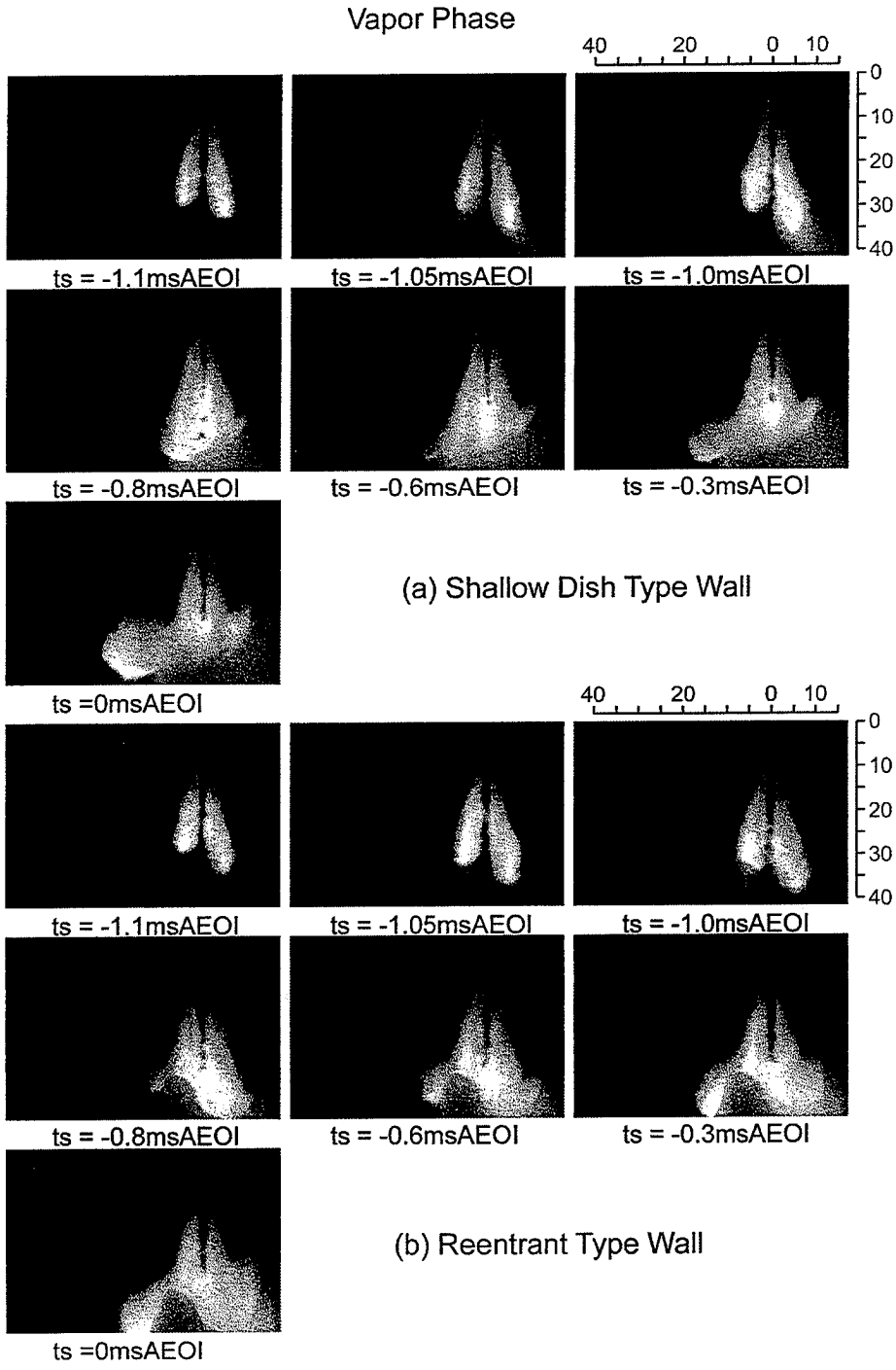

Figure 7.3 Optical thickness images of vapor phase fuel, 2-D piston cavity shape wall impinging spray from a 2-hole nozzle, d = 0.08 mm, P_{inj} = 300 MPa, ρ_a = 11 kg/m^3, (a) shallow dish type wall, (b) reentrant type wall

However, for the shallow dish type wall, large part fuel can flow out of the cavity and can mix with the ambient gas. The richest vapor phase fuel appears in the left tip region and middle region.

The characteristics of fuel vaporization for four test cases are shown **Fig. 7.4**. At the same time, comparison of sprays from a single-hole nozzle and a 2-hole nozzle is shown in **Fig. 7.5**. For the free spray, the tendency of the vaporization rate is similar to that of single-hole nozzle. However, for the flat wall impinging spray, the tendency is slightly different. As discussed in Chapter 5, after the wall impingement, M_v/M_f decreases first and then increases. For the spray from a 2-hole nozzle, it is obvious that

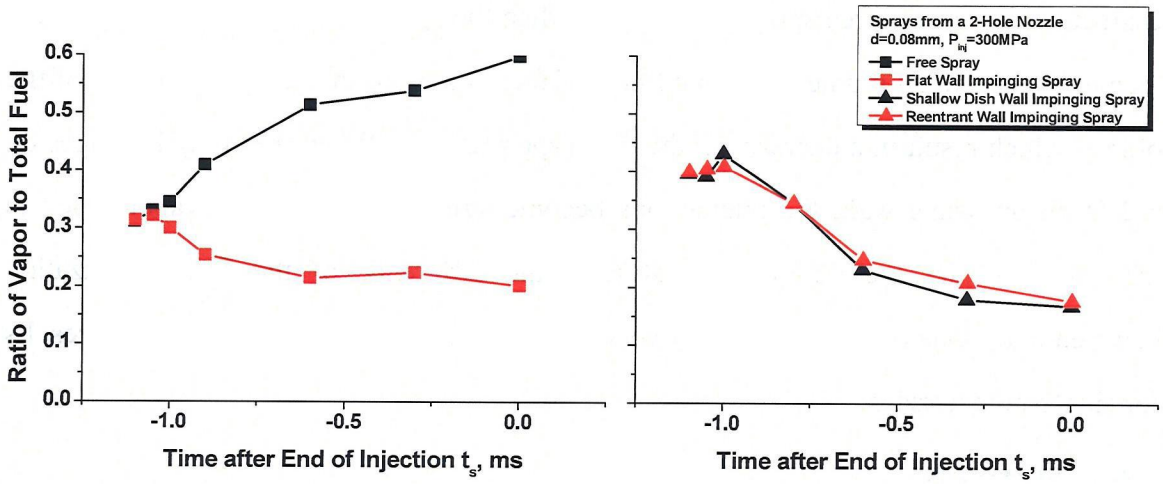

Figure 7.4 Ratio of vapor to total fuel versus time after EOI, free spray, flat wall impinging spray, and 2-D piston cavity shape wall impinging spray from a 2-hole nozzle, d = 0.08 mm, P_{inj} = 300 MPa, ρ_a = 11 kg/m^3

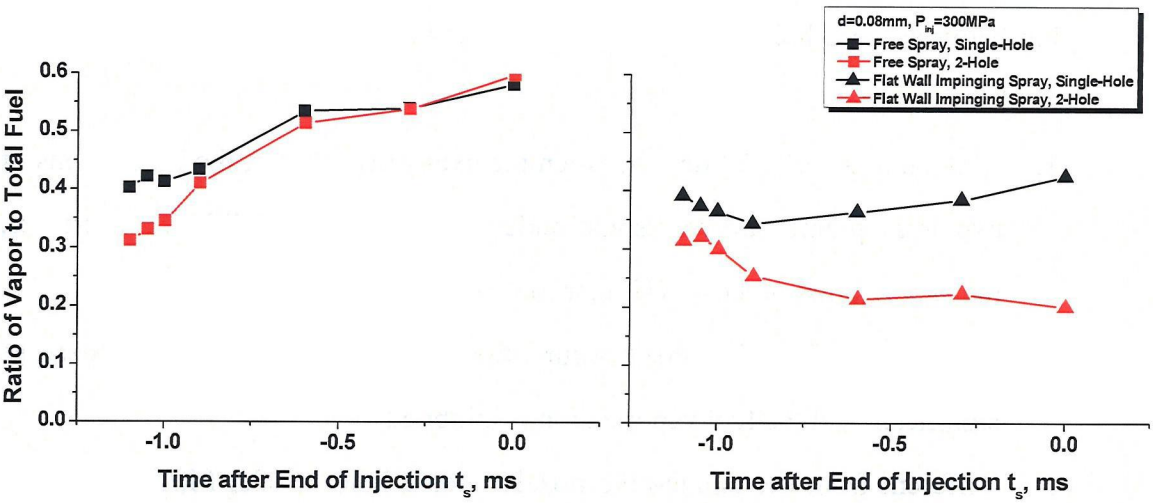

Figure 7.5 Ratio of vapor to total fuel versus time after EOI, free and flat wall impinging sprays from a single-hole nozzle and a 2-hole nozzle, d = 0.08 mm, P_{inj} = 300 MPa, ρ_a = 11 kg/m^3

M_v/M_f decreases continuously after the wall impingement. For the 2-D piston cavity shape wall impinging spray, comparison of **Figs 6.6** and **7.4** clearly shows the similar change in the tendency of M_v/M_f. According to the findings in the optical thickness images, this change may result from the influence of the interactions between two spray plumes on the vaporization. Since an angle of 23.7 deg. is large enough to avoid the overlap between the two free spray plumes, there are no pronounced changes in the spray characteristics for the free spray. However, when the spray impinges on a flat wall, the interactions between plumes occur and part of fuel is located in the central region of the plume, which result in a decrease in the fuel vaporization. When the spray impinges on a 2-D piston shape wall, the interactions become stronger and the fuel vaporization is inhibited. Under the quiescent conditions, the difference of the fuel vaporization between two kinds of cavity shapes is very small, which is similar to the previous results for single-hole nozzles.

7.3 SUMMARY

Measurements were made of the free spray, flat wall impinging spray, shallow dish type wall impinging spray, and reentrant type wall impinging spray from a 2-hole nozzle with a hole diameter of 0.08 mm. The interactions of spray plumes and the correlation between the 2-hole and single-hole nozzles were investigated. Findings are summarized as follows.

1. With an angle of 27.3 deg. between the axes of two holes, the interactions of two spray plumes are very small under the free spray condition. Therefore, the vaporization process is similar to that of single-hole nozzles.
2. When the wall impingement occurs, the interactions of two plumes become significant and the fuel vaporization is inhibited.
3. Different from the single-hole nozzles, for 2-hole nozzle, M_v/M_f decreases continuously after the wall impingement. It indicates that, with increasing the injected fuel mass, the vaporization rate cannot be maintained even under

ultra-high injection pressures. It should be very careful to apply the findings of single-hole nozzles to a multi-hole nozzle.

4. Under the quiescent condition, the influence of the cavity shape on the vaporization is very small.

Chapter 8 Ignition and Combustion of Sprays

8.1 EXPERIMENTAL CONDITIONS

As reviewed in Chapter 2, there is a close correlation between the air-fuel mixture formation and combustion processes. In the previous chapters, the mixture formation process in the free spray, flat wall impinging spray, 2-D piston cavity shape wall impinging spray, and sprays from a 2-hole nozzle were investigated using the experimental method and theoretical analysis. Some useful findings were identified. To correlate the findings in the spray measurement with the combustion process, the direct photography of the Diesel spray combustion was performed using a high-speed video camera. The natural luminosity was visualized without any filters. In addition, the OH chemiluminescence imaging was also conducted to investigate the high temperature combustion process.

Table 8.1 shows the experimental conditions for the spray combustion imaging. Four injection pressures (100, 200, 240, and 300 MPa) and two nozzle hole diameters were investigated. Diesel fuel (JIS#2, CN = 62) was used. The constant volume vessel was filled with the compressed air. To ensure the stable ignition and combustion under the fuel-lean condition, the high temperature and pressure (T_a = 885 K, P_a = 4.04 MPa) were used as the ambient conditions. The measurements were made of both the free spray and flat wall impinging spray. The parameters for the high-speed video camera system are shown in **Table 8.2**. Since an image intensifier (LaVision Inc., HS-IRO) was coupled with the high-speed video camera for all test cases, the exposure time, controlled through the image intensifier, and gain of the image intensifier were optimized to use as much of the dynamic range of the detection system as possible. At the same time, great care was taken to avoid the saturation in the images.

Table 8.1 Experimental conditions for direct photography of Diesel spray combustion

Ambient Gas Density (kg/m^3)	15 (-10 deg.ATDC)			
Ambient Gas Pressure (MPa) /Temperature (K)	4.04/885			
Spray Type	Free Spray		Flat Wall Impinging Spray	
Nozzle Hole Diameter (mm)	0.16		0.08	
Injection Pressure (MPa)	100	200	240	300
Injection Quantity (mg)	15.47	11.85	6.04	3.87
Injection Duration (ms)	2.2 (@100MPa)	1.5 (@200MPa)	1.4 (@240MPa)	1.3 (@300MPa)
Assumed Number of Nozzle Holes for 70 mg	4	6	11	18

Table 8.2 Parameters for high-speed video camera system, free spray and flat wall impinging spray

	Free Spray	Impinging Spray
Frame Rate (fps)	10,000	20,000
Resolution (pixel)	512 x 512	512 x 256
Exposure Time (s)	Controlled through image intensifier	
Focus Length (mm)	105	
f/number	4.5	

8.2 RESULTS AND DISCUSSION

8.2.1 Auto-Ignition Process

When a Diesel spray is injected into the hot air in the constant volume vessel, the spray vaporization and the ignition processes take place. The auto-ignition process in Diesel engines has been studied by a lot of researchers. The aim of this work is to present the results of the spray combustion formed by a micro-hole nozzle under an ultra-high injection pressure. The initial auto-ignition was detected using the OH chemiluminescence imaging. In Diesel engines, the auto-ignition timing is commonly

defined as the crank angle when the apparent hear release rate reverses direction or first goes positive. However, as reviewed in Chapter 2, relatively weak flame emission that is due to chemiluminescence occurs prior to the conventional auto-ignition timing. **Figure 8.1** shows the images of the ignition process for free sprays under different conditions. The images of the non-evaporating free sprays, acquired using a high-speed video camera, were also shown in **Fig. 8.1**. Note that the visual comparisons of brightness level between images cannot be used to make quantitative comparisons of actual measured intensities. The reason is that the sensitivity of the detection system was optimized for each image separately to use the full dynamic range of the camera. Therefore, the same apparent brightness in two images with different sensitivity values will correspond to different numbers of incident photons. The images given here only show the overall structures of the spray flames.

As shown in **Fig. 8.1**, since the penetration length decreases greatly as the nozzle hole diameter decreases, the auto-ignition point shifts upstream. It should be noted that the auto-ignition marked by OH chemiluminescence occurs at around the leading portion of spray plumes. The region is relatively large, especially for the 0.16 mm nozzle, which suggests that the ignition occurs at multiple points nearly simultaneously. At the end of injection, the chemiluminescence emission appears across the whole downstream region of the spray plume. As the nozzle hole diameter decreases, the region of the chemiluminescence emission at the auto-ignition timing decreases obviously. At the same time, with increasing the injection pressure, this region also decreases. Comparison of these results and the previous findings in the spray experiments using the LAS technique shows that it may be caused by the fact that the overall equivalence ratio is decreased by the reduced nozzle hole diameter and increased injection pressure.

The temporal sequence and comparison of the evaporating spray and combusting jet injected from the 0.08 mm nozzle at 300 MPa is shown in **Fig. 8.2**. It is obvious that the auto-ignition occurs at the tip region with a higher vapor phase equivalence ratio. After the auto-ignition, the area of the chemiluminescence emission increases

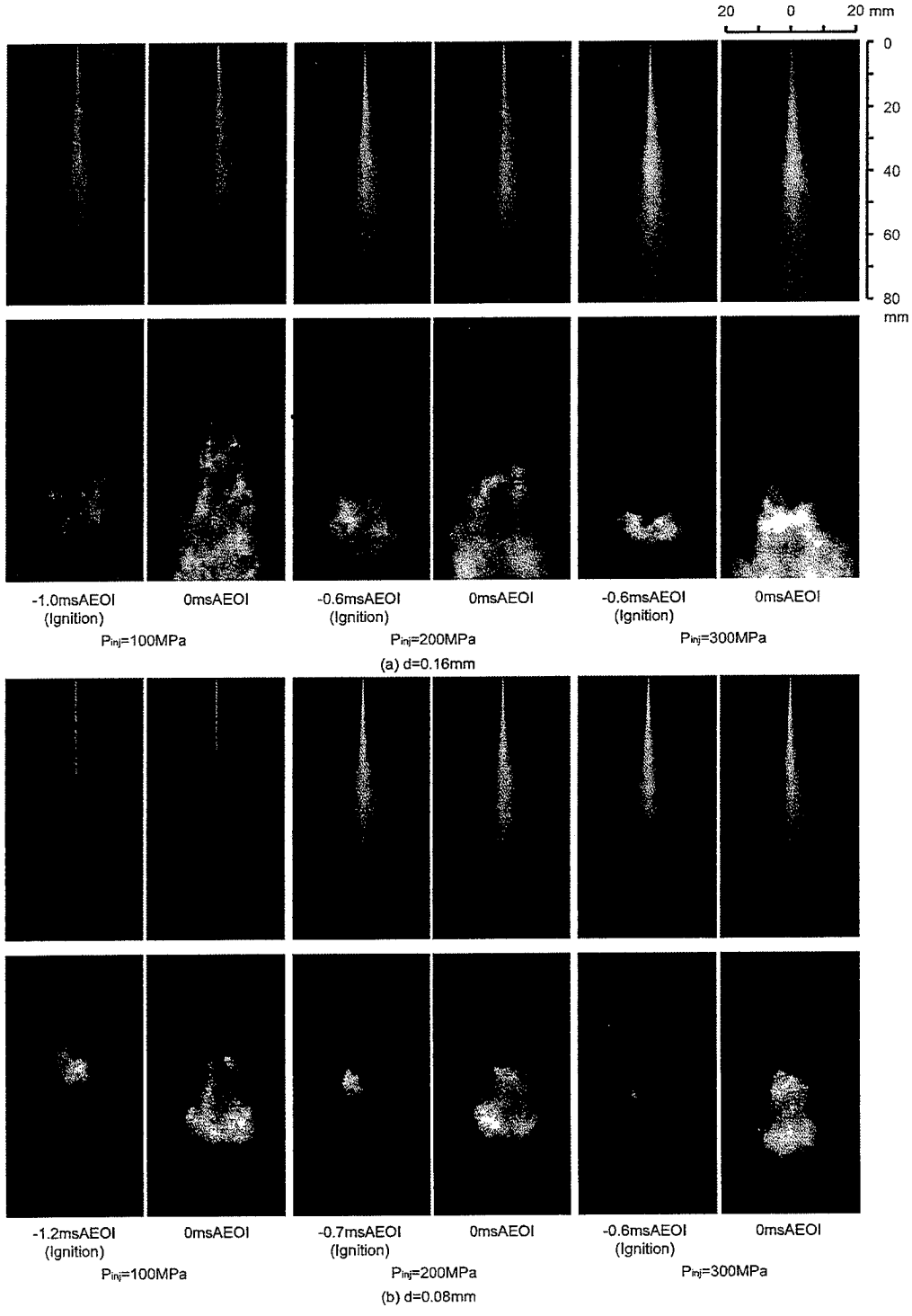

Figure 8.1 Spray and flame images at the ignition timing and at EOI, P_{inj} = 100, 200, and 300 MPa, ρ_a = 15 kg/m^3, (a) d = 0.16 mm, (b) d = 0.08 mm

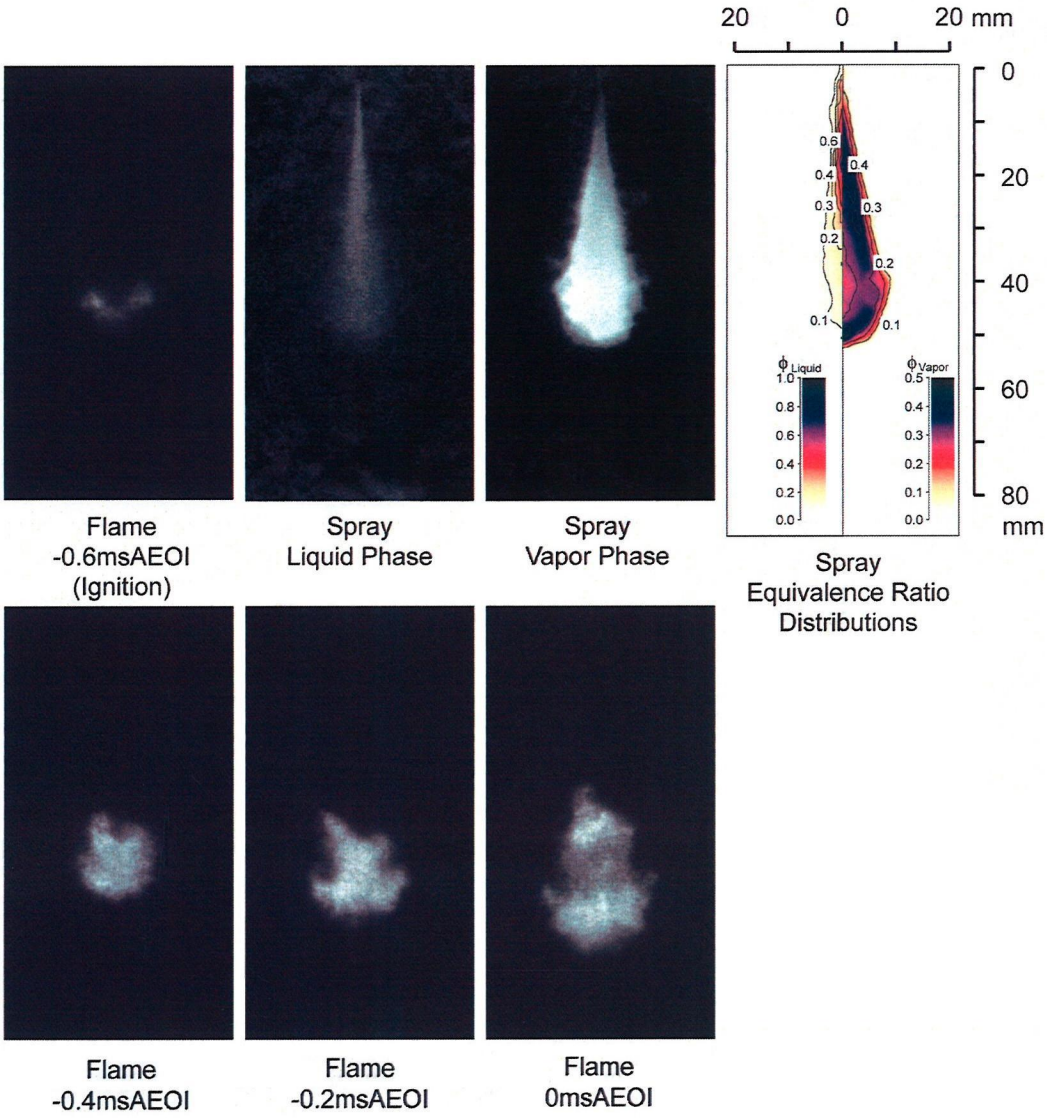

Figure 8.2 Temporal sequence of spray flame images at four timings, optical thickness images and equivalence ratio distribution contours of the evaporating spray at the auto-ignition timing (-0.6 msAEOI), d = 0.08 mm, P_{inj} = 300 MPa, ρ_a = 15 kg/m^3

significantly. It is worth noting that, since the images are integrated along the line of sight through the spray plume, they do not show whether the chemical reactions are confined to the peripheral regions or are volumetric.

Figure 8.3 shows the ignition delay for two nozzles under different injection pressures. It obviously indicates that, for two test nozzles, the increased injection pressure has a strong influence on the ignition delay. For the 0.16 mm nozzle, as the injection pressure increases from 100 to 300 MPa, the ignition delay reduces by half.

Note that, since the total injected fuel quantity is different for the two nozzles, the influence of the nozzle hole diameter cannot be acquired from **Fig. 8.3**. As the injection quantity increases, the ignition delay increases due to the heat absorption during the fuel evaporation process.

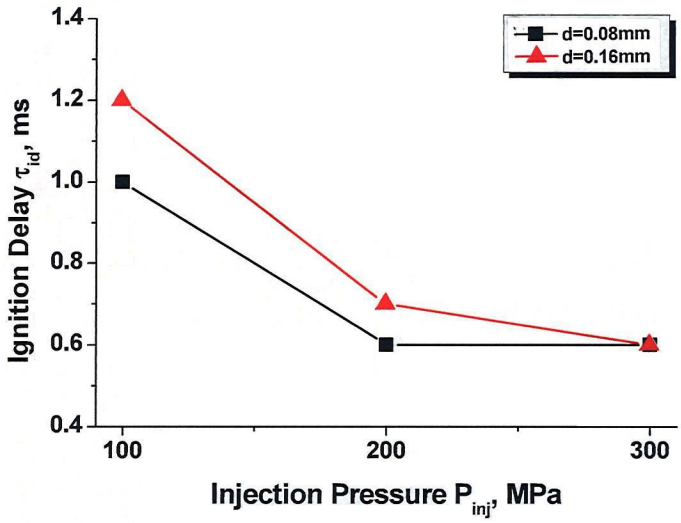

Figure 8.3 Ignition delay of free spray combustion under different injection pressures, P_{inj} = 100, 200, and 300 MPa, d = 0.16 and 0.08 mm, ρ_a = 15 kg/m^3

8.2.2 Flame Lift-Off Length

After the auto-ignition process is completed, on a high-temperature D.I. Diesel spray under quiescent conditions, the flame stabilizes at a quasi-steady, axisymmetric location downstream of the nozzle tip. The most upstream location of combustion on the spray during injection is referred to as the lift-off length. In this work, for the free sprays, the effects of the injection pressure and nozzle hole diameter on the flame lift-off length will be discussed qualitatively.

Figure 8.4 shows the OH chemiluminescence images of the lifted turbulent flames under different conditions. The top of each image is the nozzle tip. It is obvious that, the lift-off length increases with increasing the injection pressure. The dependence of the flame lift-off length on the injection pressure is consistent with the discussion on the air entrainment in Chapter 4. The air entrainment measured with the LAS technique increases obviously with increasing the injection pressure, thus resulting

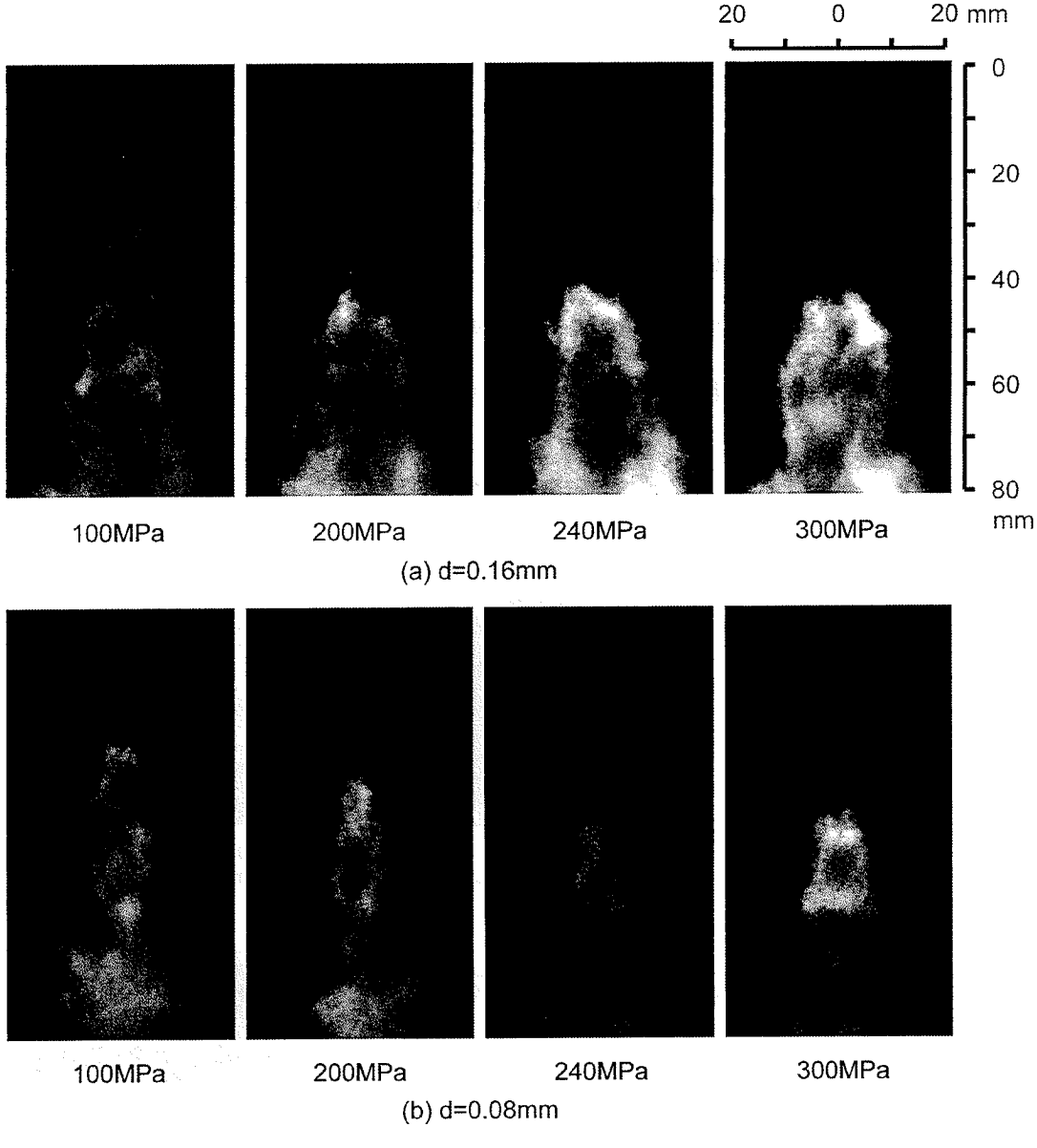

Figure 8.4 Flame lift-off length in OH chemiluminescence images, P_{inj} = 100, 200, 240, and 300 MPa, ρ_a = 15 kg/m^3, (a) d = 0.16 mm, (b) d = 0.08 mm

in the increase in the lift-off length. In addition, as the nozzle hole diameter decreases, the lift-off length decreases slightly. According to the previous results in Chapter 4, the air entrainment increases significantly with decreasing the nozzle hold diameter, which results in an increase in the fuel vaporization rate and in a decrease in the ignition delay.

The results of the spray combustion presented in this section shows that the dependence of the life-off length on the nozzle hole diameter is much smaller than that of the fuel vaporization rate.

8.2.3 Effect of Spray/Wall Interactions on Spray Flames

When a Diesel spray impinges on a flat wall, as described in Chapter 5, the spray characteristics will be greatly different from that of a free spray. The natural soot luminosity images acquired using a high-speed video camera without any filters were used to qualitatively analyze the sooting flame. Although this method cannot provide quantitative information on the soot concentrations, it gives a general picture of the sooting flame integrated along the line of sight through the spray plume.

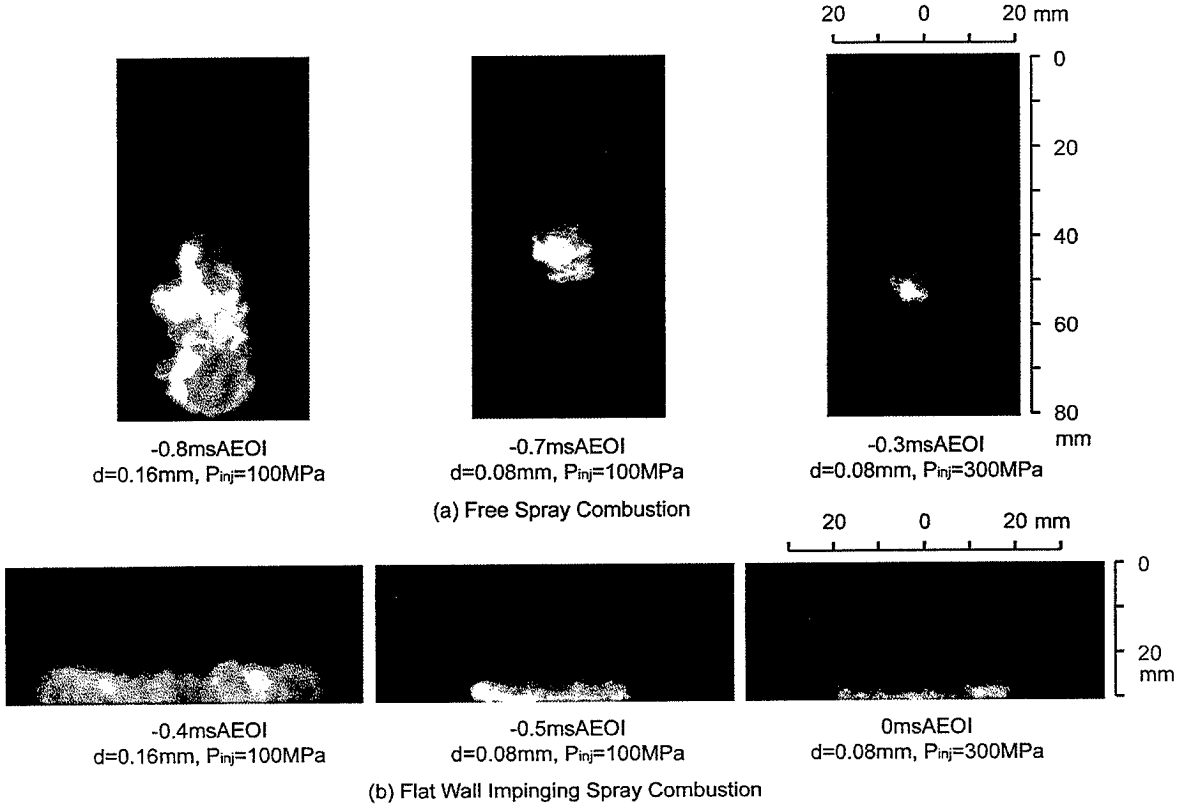

Figure 8.5 Natural soot luminosity images at the timing of start of soot formation, d = 0.16 and 0.08 mm, P_{inj} = 100 and 300 MPa, ρ_a = 15 kg/m^3 (a) free spray combustion, (b) flat wall impinging spray combustion

Figure 8.5 shows the natural soot luminosity images for both free and flat wall impinging sprays at three representative conditions. The occurrence of a very bright region after the auto-ignition is considered as the start of the soot formation. As the nozzle hole diameter decreases from 0.16 to 0.08 mm, the region of soot luminosity becomes smaller. As the injection pressure increases from 100 to 300 MPa for the 0.08

mm nozzle, the bright region further reduces. The comparison of the free spray combustion images and flat wall impinging spray combustion ones shows the spray/wall interactions obviously postpone the occurrence of the sooting flames. In comparison of this result and the findings of the air entrainment in Chapter 5, this delay of the soot formation is likely caused by the fact that, within the injection duration, the air entrainment rate is increased by the wall impingement, which enhances the soot oxidation and reduces the soot formation. Therefore, this delay may be dependence on the intensity of the spray/wall interactions. As shown in **Fig. 8.5**, the delay for 0.16 mm nozzle at 100 MPa is 0.4 ms, whereas that for 0.08 mm at 100 MPa is only 0.2 ms. The nozzle with a smaller diameter generates smaller drop size and results in weaker drop/wall interactions. At the same time, the relatively low temperature of the impingement wall may cool the combusting jet and reduce the rate of soot formation. The detailed mechanism requires further quantitative investigations.

8.3 SUMMARY

Measurements were made of the natural soot luminosity imaging and OH chemiluminescence imaging of both the free and flat wall impinging spray combustion. Qualitative analysis of the flame images was performed and some results were correlated to the previous findings of the sprays.

1. The auto-ignition marked by OH chemiluminescence occurs at around the leading portion of spray plumes. The region is relatively large and decreases obviously with decreasing the nozzle hole diameter or with increasing the injection pressure.
2. The compassion of spray and combustion images shows that the auto-ignition occurs at the spray tip region with a higher vapor phase equivalence ratio.
3. The flame lift-off length increases with increasing the injection pressure, which is caused by the enhanced air entrainment. The dependence of the flame lift-off length on the nozzle hole diameter is much smaller than that of the fuel vaporization rate.

4. Comparison of the free and flat wall impinging spray combustion images shows the spray/wall interactions obviously postpone the occurrence of the sooting flames. One possible reason is that the spray/wall interactions enhance the air entrainment, increase the soot oxidation, and decrease the rate of soot formation.

Chapter 9 Conclusions

The spray and mixture formation process was investigated using the LAS technique to acquire the qualitative and quantitative information on the characteristics of free sprays, flat wall impinging sprays, 2-D piston cavity shape sprays, and 2-hole nozzle sprays. The auto-ignition and flame structure were investigated using a high-speed video camera system. The correlation between spray characteristics of single-hole and 2-hole nozzle was clarified, and the relationship between the mixture formation and combustion processes was presented. Measurements and analyses were focused on the spray and combustion of Diesel sprays from micro-hole nozzles under ultra-high injection pressures. The injection parameter and ambient condition were varied to acquire a better understanding of the governing mechanisms of mixture formation and combustion processes. General conclusions are summarized as follows.

9.1 SPRAY CHARACTERISTICS

9.1.1 Penetration

Non evaporating spray imaging shows that, for the free spray, the spray tip penetration length is dependent on the nozzle hole diameter. This dependence is almost invariant with increasing the injection pressure, whereas it is influenced by the increased ambient density. At the higher ambient density, increasing the injection pressure up to 300 MPa may slightly change the dependence of the penetration on the nozzle hole diameter. Under the evaporating condition, for the flat wall impinging spray, the micro-hole nozzles are also very effective in reducing the spray tip penetration length. The contour of $\Phi_{Liquid} = 0.5$ can be used as the boundary of the liquid phase fuel. The liquid phase penetration length is dependent on the nozzle hole diameter. With the evolution of the spray plumes, this length will reach a steady state.

9.1.2 Entrainment

Generally speaking, the air entrainment increases with increasing the injection pressure or decreasing the nozzle hole diameter. By examining the first stage of the injection duration, it is found that, for the micro-hole nozzle under the ultra-high injection pressure, both vaporization and entrainment are significantly high. The combination of micro-hole nozzles and ultra-high injection pressures may change the primary breakup mechanism.

For the flat wall impinging spray, at around the impingement timings, there are no pronounced changes in the air entrainment (M_a/M_f). In comparison to the free spray, within the injection duration, the air entrainment is enhanced by the spray/wall interactions.

9.1.3 Vaporization

Due to the spray/wall or spray/spray interactions, the tendency of the fuel vaporization (M_v/M_f) varies for different spray types.

For the free spray, M_v/M_f increases continuously.

For the wall (flat and 2-D) impinging spray, M_v/M_f increases from the start of injection, decreases after the wall impingement, and then increases slightly until the end of injection.

For the free spray from a 2-hole nozzle, since there are almost no interactions between two plumes under current test conditions, the tendency of M_v/M_f is similar to that for the free spray from a single-hole nozzle.

For the wall impinging spray from a 2-hole nozzle, M_v/M_f decreases continuously after the wall impingement because of the interactions between two plumes.

9.1.4 Other Findings

Comparison of measured and predicted penetration length results showed that gas jet theory could be used to simulate Diesel sprays approximately. The sprays formed by the micro-hole nozzle were more similar to the gas jets than those formed by the

conventional nozzles were. To achieve good agreement, the experimentally determined constants should be carefully selected and verified.

Results acquired using the LAS technique and axisymmetric data processing method show that the secondary breakup is influenced by increasing the injection pressure, which result in a significant decrease in SMD after EOI. Further studies on the flat wall impinging sprays show that, for micro-hole nozzles, the injection pressure of 100 MPa is not high enough and may, to some extent, cause the mixing process to deteriorate. The injection pressure of 300 MPa can provide enough energy for micro-hole nozzles to maintain a high spray momentum close to EOI.

Under the quiescent condition, for both single-hole and 2-hole nozzles, there are no obvious influences of the cavity shape on the vaporization process. The result indicates that it is possible to use the reentrant type combustion chamber that can generate a strong squish flow to obtain stronger entrainment and faster vaporization under the real engine condition.

The influence of the spray umbrella angle on the vaporization process for the reentrant type wall is much stronger than that for the shallow dish wall.

The combination of a micro-hole nozzle and an ultra-high injection pressure can accelerate the preparation of a lean and uniform mixture, which provides some promising characteristics for PCI combustion close to TDC.

9.2 COMBUSTION CHARACTERISTICS

The auto-ignition marked by OH chemiluminescence occurs at around the leading portion of spray plumes. The region is relatively large and decreases obviously with decreasing the nozzle hole diameter decreases or increasing the injection pressure. The compassion of spray and combustion images shows that the auto-ignition occurs at the spray tip region with a higher vapor phase equivalence ratio.

The flame lift-off length increases with increasing the injection pressure, which is caused by the enhanced air entrainment. The dependence of the flame lift-off length on the nozzle hole diameter is much smaller than that of the fuel vaporization rate.

Comparison of the free and flat wall impinging spray combustion images shows the spray/wall interactions obviously postpone the occurrence of the sooting flames. One possible reason is that the spray/wall interactions enhance the air entrainment, increase the soot oxidation, and decrease the rate of soot formation.

9.3 RECOMMENDATIONS FOR FUTURE WORK

Several recommendations can be made for future work in this field. Most recommendations could be performed using the same experimental apparatus.

The detailed mechanisms of spray/wall interactions are still unclear. Further investigation could start from designing a fundamental experiment to measure the mass of wall film. This work could improve the accuracy of the current LAS system and could provide more information for the numerical simulation.

Current results show that, for micro-hole nozzles, the discrepancy between measurements and predictions is relatively large. It may be caused by the fact that there is a significant difference in the spray atomization and mixing processes between the conventional nozzles and micro-hole ones. Therefore, more fundamental experiments with systematically varying more parameters are recommended to provide data for calibrating the predicative models. New breakup models for the nozzle with the diameter less than 0.1 mm are required for the accurate simulation.

Some phenomena appeared in the present experiments may result from the different nature of the internal flow for micro-hole nozzles under ultra-high injection pressure. A new experimental setup could be designed to investigate the real-size internal flow. The better understanding of the cavitation and turbulence inside the nozzle hole is believed to be helpful to explain the present results more accurately.

Bibliography

1. Akagawa, H., Miyamoto, T., Harada, A., Sasaki, S., Shimazaki, N., Hashizume, T., and Tsujimura, K. (1999) Approaches to Solve Problems of the Premixed Lean Diesel Combustion. *SAE Paper* 1999-01-0183.
2. Amann, M., Buckingham, J., and Kono, N. (2006) Evaluation of HCCI Engine Potentials in Comparison to Advanced Gasoline and Diesel Engines. *SAE Paper* 2006-01-3249.
3. Baritaud, T. A., Heinze, T. A., and Le Coz, J. F. (1994) Spray and Self-Ignition Visualization a DI Diesel Engine. *SAE Paper* 940681.
4. Baumgarten, C. (2006) *Mixture Formation in Internal Combustion Engine*. Berlin Heidelberg, Springer-Verlag.
5. Benajes, J., Molina, S., De Rudder, K., Maroteaux, D., and Hamouda, H. B. H. (2006) The Use of Micro-Orifice Nozzles and Swirl in a Small HSDI Engine Operating at a Late Split-Injection LTC Regime. *Proceedings of the Institution of Mechanical Engineers Part D-Journal of Automobile Engineering*, **220**, 1807-1817.
6. Bergstrand, P. and Denbratt, I. (2001) Diesel Combustion with Reduced Nozzle Orifice Diameter. *SAE Paper* 2001-01-2010.
7. Bohren, C. F. and Huffman, D. R. (1983) *Absorption and Scattering of Light by Small Particles*. New York, John Wiley & Sons.
8. Bruneaux, G. (2001) Liquid and Vapor Spray Structure in High-Pressure Common Rail Diesel Injection. *Atomization and Sprays*, **11**, 533-556.
9. Cavaliere, A. and Mara, d. J. (2004) Mild Combustion. *Progress in Energy and Combustion Science*, **30**, 329-366.
10. Chehroudi, B., Chen, S.-H., Bracco, F. V., and Onuma, Y. (1985) On the Intact Core of Full-Cone Sprays. *SAE Paper* 850126.
11. Chigier, N. (2006) Challenges for Future Research in Atomization and Spray Technology: Arthur Lefebvre Memorial Lecture. *Atomization and Sprays*, **16**, 727-736.
12. Choi, D., Miles, P. C., Yun, H., and Reitz, R. D. (2005) A Parametric Study of Low-Temperature, Late-Injection Combustion in a HSDI Diesel Engine. *JSME International Journal, Serie B, Fluids and Thermal Engineering*, **48**, 656-664.
13. Chraplyvy, A. R. (1981) Nonintrusive Measurements of Vapor Concentrations inside Sprays. *Appl. Opt.*, **20**, 2620-2624.
14. Christensen, M., Hultqvist, A., and Johansson, B. (1999) Demonstrating the Multi-Fuel Capability of a Homogeneous Charge Compression Ignition Engine With Variable Compression Ratio. *SAE Paper* 1999-01-3679.
15. Christensen, M., Johansson, B., Amneus, P. J. H., and Mauss, F. (1998) Supercharged Homogeneous Charge Compression Ignition. *SAE Paper* 980787.
16. Costa, M., Vaglieco, B., and Corcione, F. (2005) Radical Species in the Cool-Flame Regime of Diesel Combustion: A Comparative Numerical and Experimental Study. *Experiments in Fluids*, **39**, 514-526.
17. Dec, J. E. (1992) Soot Distribution in a D.I. Diesel Engine Using 2-D Imaging of Laser-Induced Incandescence, Elastic Scattering, and Flame Luminosity. *SAE Paper* 920115.
18. Dec, J. E. (1997) A Conceptual Model of DI Diesel Combustion Based on Laser-Sheet Imaging. *SAE Paper* 970873.
19. Dec, J. E. and Espey, C. (1995) Ingition and Early Soot Formation in a D.I. Diesel Engine Using Multiple 2-D Imaging Diagnostics. *SAE Paper* 950456.
20. Dec, J. E. and Espey, C. (1998) Chemiluminescence Imaging of Autoignition in a DI Diesel Engine. *SAE Paper* 982685.
21. Dodge, L. G., Simescu, S., Neely, G. D., Maymar, M. J., Dickey, D. W., and Savonen, C. L. (2002) Effect of Small Holes and High Injection Pressures on Diesel Engine Combustion. *SAE Paper* 2002-01-0494.
22. Eckbreth, A. C. (1996) *Laser Diagnostics for Combustion Temperature and Species*. 2nd ed., Amsterdam, Gordon and Breach.

23. Ekholm, K., Karlsson, M., Tunestal, P., Johansson, R., Johansson, B., and Strandh, P. (2008) Ethanol-Diesel Fumigation in Multi-Cylinder Engine. *SAE Paper* 2008-01-0033.
24. Espey, C. and Dec, J. E. (1993) Diesel Engine Combustion Studies in a Newly Designed Optical-Access Engine Using High-Speed Visualization and 2-D Laser Imaging. *SAE Paper* 930971.
25. Faeth, G. M. (1987) Mixing, Transport and Combustion in Sprays. *Progress in Energy and Combustion Science*, **13**, 293-345.
26. Faeth, G. M. (1991) Structure and Atomization Properties of Dense Turbulent Sprays. *Symposium (International) on Combustion*, **23**, 1345-1352.
27. Faeth, G. M., Hsiang, L. P., and Wu, P. K. (1995) Structure and Breakup Properties of Sprays. *International Journal of Multiphase Flow*, **21**, 99-127.
28. Flynn, P. F., Durrett, R. P., Hunter, G. L., Loye, A. Z., Akinyemi, O. C., Dec, J. E., and Westbrook, C. K. (1999) Diesel Combustion: An Integrated View Combining Laser Diagnostics, Chemical Kinetics, and Empirical Validation. *SAE Paper* 1999-01-0509.
29. Fujimoto, H., Hyun, G.-S., Nogami, M., Hirakawa, K., Asai, T., and Senda, J. (1997) Characteristics of Free and Impinging Gas Jets by Means of Image Processing. *SAE Paper* 970045.
30. Fujimoto, H., Iids, H., Aoyama, T., and Senda, J. (1994) Analysis of Combustion Characteristics in Diesel Flame by Means of Chemiluminescence. *Proc. COMODIA '94.*
31. Gaydon, A. G. (1974) *The Spectroscopy of Flames*. 2nd ed., London, Chapman and Hall.
32. Glauert, M. B. (1956) The Wall Jet. *Journal of Fluid Mechanics*, **1**, 625-643.
33. Gray III, A. W. and Ryan III, T. W. (1997) Homogeneous Charge Compression Ignition (HCCI) of Diesel Fuel. *SAE Paper* 971676.
34. Gulder, O. L., Smallwood, G. J., and Snelling, D. R. (1992) Diesel Spray Structure Investigation by Laser Diffraction and Sheet Illumination. *SAE Paper* 920577.
35. Gumprecht, R. O. and Sliepcevich, C. M. (1953) Scattering of Light by Large Spherical Particles. *J. Phys. Chem.*, **57**, 90-95.
36. Hammond Jr., D. C. (1981) Deconvolution Technique for Line-of-Sight Optical Scattering Measurements in Axisymmetric Sprays. *Applied Optics*, **20**, 493.
37. Hasegawa, R. and Yanagihara, H. (2003) HCCI Combustion in DI Diesel Engine. *SAE Paper* 2003-01-0745.
38. Hashizume, T., Miyamoto, T., Akagawa, H., and Tsujimura, K. (1998) Combustion and Emission Characteristics of Multiple-Dtage Diesel Combustion. *SAE Paper* 980505.
39. Heywood, J. B. (1988) *Internal Combustion Engine Fundamentals*. New York, McGraw-Hill.
40. Higgins, B., Siebers, D., and Aradi, A. (2000) Diesel-Spray Ignition and Premixed-Burn Behavior. *SAE Paper* 2000-01-0940.
41. Hildingsson, L., Persson, H., Johansson, B., Collin, R., Nygren, J., Richter, M., Alden, M., Hasegawa, R., and Yanagihara, H. (2005) Optical Diagnostics of HCCI and UNIBUS Using 2-D PLIF of OH and Formaldehyde. *SAE Paper* 2005-01-0175.
42. Hiroyasu, H. (2000) Spray Breakup Mechanism from the Hole-Type Nozzle and Its Applications. *Atomization and Sprays*, **10**, 511-527.
43. Hiroyasu, H. and Arai, M. (1990) Structures of Fuel Sprays in Diesel Engines. *SAE Paper* 900475.
44. Hiroyasu, H., Arai, M., and Shimizu, M. (1982) The Breakup of a High Speed Jet in a High Pressure Gaseous Atmosphere. *Proc. ICLASS-82.*
45. Ikegami, M. (1990) Role of Flows and Turbulent Mixing in Combustion and Pollutant Formation in Diesel Engines. *Int. Symp. COMODIA 90.* Kyoto, Japan.
46. Ishii, H., Koike, N., Suzuki, H., and Odaka, M. (1997) Exhaust Purification of Diesel Engines by Homogeneous Charge with Compression Ignition Part 2: Analysis of Combustion Phenomena and NO_x Formation by Numerical Simulation with Experiment. *SAE Paper* 970315.
47. Ishikawa, N., Ohkubo, Y., and Kudou, K. (2007) Study on the Effects of EGR Cooler Performance on Combustion Properties of the Pre-Mixed Compression Ignition Combustion by Multi-Cylinder DI Diesel Engine. *SAE Paper* 2007-01-1881.
48. Iwabuchi, Y., Kawai, K., Shoji, T., and Takeda, Y. (1999) Trial of New Concept Diesel Combustion System - Premixed Compression-Ignition Combustion. *SAE Paper* 1999-01-0185.
49. Kamimoto, T. and Kobayashi, H. (1991) Combustion Processes in Diesel Engines. *Progress in Energy and Combustion Science*, **17**, 163-189.

50. Kamimoto, T., Yokota, H., and Kobayashi, H. (1989) A New Technique for the Measurement of Sauter Mean Diameter of Droplets in Unsteady Dense Sprays. *SAE Paper* 890316.
51. Kato, T., Tsujimura, K., Shintani, M., Minami, T., and Yamaguchi, I. (1989) Spray Characteristics and Combustion Improvement of DI Diesel Engine with High Pressure Fuel Injection. *SAE Paper* 890265.
52. Kerker, M. (1969) *The Scattering of Light, and Other Electromagnetic Radiation.* New York, Academic Press.
53. Kimura, S., Aoki, O., Kitahara, Y., and Aiyoshizawa, E. (2001) Ultra-Clean Combustion Technology Combining a Low-Temperature and Premixed Combustion Concept for Meeting Future Emission Standards. *SAE Paper* 2001-01-0200.
54. Kimura, S., Aoki, O., Ogawa, H., Muranaka, S., and Enomoto, Y. (1999) New Combustion Concept for Ultra-Clean and High-Efficiency Small Di Diesel Engines. *SAE Paper* 1999-01-3681.
55. Kimura, S., Ogawa, H., Matsui, Y., and Enomoto, Y. (2002) An Experimental Analysis of Low-Temperature and Premixed Combustion for Simultaneous Reduction of NO_x and Particulate Emissions in Direct Injection Diesel Engines. *International Journal of Engine Research*, **3**, 249-259.
56. Kitabatake, R., Shimazaki, N., and Nishimura, T. (2007) Expansion of Premixed Compression Ignition Combustion Region by Supercharging Operation and Lower Compression Ratio. *SAE Paper* 2007-01-3614.
57. Ko, K. and Arai, M. (2002a) The Characteristics of Postimpingement Diesel Spray, Part I: Penetration and Volume. *Atomization and Sprays*, **12**, 403-417.
58. Ko, K. and Arai, M. (2002b) The Characteristics of Postimpingement Diesel Spray, Part II: Empirical Equation of Penetration. *Atomization and Sprays*, **12**, 419-430.
59. Ko, K. and Arai, M. (2002c) Diesel Spray Impinging on a Flat Wall, Part I: Characteristics of Adhered Fuel Film in an Impingement Diesel Spray. *Atomization and Sprays*, **12**, 737-751.
60. Ko, K. and Arai, M. (2002d) Diesel Spray Impinging on a Flat Wall, Part II: Volume and Average Air-Fuel Ratio of an Impingement Diesel Spray. *Atomization and Sprays*, **12**, 753-767.
61. Kobori, S., Kamimoto, T., and Aradi, A. A. (2000) A Study of Ignition Delay of Diesel Fuel Sprays. *International Journal of Engine Research*, **1**, 29-39.
62. Kohse-Hoinghaus, K. and Jeffries, J. B. (2002) *Applied Combustion Diagnostics.* New York, Taylor & Francis.
63. Kong, S. C. (2007) Drop/Wall Interaction Criteria and Their Applications in Diesel Spray Modeling. *Atomization and Sprays*, **17**, 473-499.
64. Kosaka, H. and Kamimoto, T. (1993) Quantitative Measurement of Fuel Vapor Concentration in an Unsteady Evaporating Spray via a 2-D Mie-Scattering Imaging *SAE Paper* 932653.
65. Kosaka, H., Won, Y.-H., and Kamimoto, T. (1992) A Study of the Structure of Diesel Sprays Using 2-D Imaging Techniques. *SAE Paper* 920107.
66. Kowalewicz, A. (1984) *Combustion Systems of High Speed Piston I.C. Engines.* New York, Elsevier.
67. Lefebvre, A. H. (1989) *Atomization and Sprays.* New York, Hemisphere.
68. Li, T. (2004) *Characterization of Spray and Mixture Formation Processes of DI Gasoline Engines.* Ph.D. Dissertation, Kinki University.
69. MacPhee, A. G., Tate, M. W., Powell, C. F., Yue, Y., Renzi, M. J., Ercan, A., Narayanan, S., Fontes, E., Walther, J., Schaller, J., Gruner, S. M., and Wang, J. (2002) X-ray Imaging of Shock Waves Generated by High-Pressure Fuel Sprays. *Science*, **295**, 1261-1263.
70. Mathews, W. S., Lee, C. F., and Peters, J. E. (2003) Experimental Investigations of Spray/Wall Impingement. *Atomization and Sprays*, **13**, 223-242.
71. Matsui, Y., Kamimoto, T., and Matsuoka, S. (1979) A Study on the Time and Space Resolved Measurement of Flame Temperature and Soot Concentration in a D.I. Diesel Engine by the Two-Color Method. *SAE Paper* 790491.
72. Matsui, Y., Kamimoto, T., and Matsuoka, S. (1982) Formation and Oxidation Processes of Soot Particulates in a D. I. Diesel Engine - An Experimental Study via the Two-color Method. *SAE Paper* 820464.
73. Matsumoto, Y., Gao, J., and Nishida, K. (2008) Spray and Mixture Characteristics of Group-Hole Nozzle for a D.I. Diesel Engine. *Transactions of JSAE*, **39**, 177-182.

74. Melton, L. A. and Verdieck, J. F. (1985) Vapor/Liquid Visualization in Fuel Sprays. *Symposium (International) on Combustion*, **20**, 1283-1290.
75. Minato, A., Tanaka, T., and Nishimura, T. (2005) Investigation of Premixed Lean Diesel Combustion with Ultra High Pressure Injection. *SAE Paper* 2005-01-0914.
76. Molina, S., Benajes, J., Garcia, J. M., and Novella, R. (2004) Influence of Boost Pressure and Injection Pressure on Combustion Process and Exhaust Emissions in a HD Diesel Engine. *SAE Paper* 2004-01-1842.
77. Montgomery, D. T., Chan, M., Chang, C. T., Farrell, P. V., and Reitz, R. D. (1996) Effect of Injector Nozzle Hole Size and Number on Spray Characteristics and the Performance of a Heavy-Duty D.I. Diesel Engine. *SAE Paper* 962002.
78. Mueller, C. J. and Martin, G. C. (2002) Effects of Oxygenated Compounds on Combustion and Soot Evolution in a DI Diesel Engine: Broadband Natural Luminosity Imaging. *SAE Paper* 2002-01-1631.
79. Musculus, M. P. B. (2006) Multiple Simultaneous Optical Diagnostic Imaging of Early-Injection, Low-Temperature Combustion in a Heavy-Duty Diesel *SAE Paper* 2006-01-0079.
80. Najt, P. M. and Foster, D. E. (1983) Compression-Ignited Homogeneous Charge Combustion. *SAE Paper* 830264.
81. Nelson, P. R., Coffin, M., and Copeland, K. A. F. (2003) Summarizing Data. *Introductory Statistics for Engineering Experimentation.* San Diego, Academic Press.
82. Nishijima, Y., Asaumi, Y., and Aoyagi, Y. (2001) Premixed Lean Diesel Combustion (PREDIC) Using Impingement Spray System. *SAE Paper* 2001-01-1892.
83. Noguchi, M., Tanaka, Y., Tanaka, T., and Takeuchi, Y. (1979) A Study on Gasoline Engine Combustion By Observation of Intermediate Reactive Products During Combustion. *SAE Paper* 790840.
84. Okude, K., Mori, K., Shiino, S., and Moriya, T. (2004) Premixed Compression Ignition (PCI) Combustion for Simultaneous Reduction of NO_x and Soot in Diesel Engine. *SAE Paper* 2004-01-1907.
85. Onishi, S., Jo, S. H., Shoda, K., Jo, P. D., and Kato, S. (1979) Active Thermo-Atmosphere Combustion (ATAC) - A New Combustion Process for Internal Combustion Engines. *SAE Paper* 790501.
86. Oppenheim, A. K. (1984) The Knock Syndrome - Its Cures and Its Victims. *SAE Paper* 841339.
87. Oppenheim, A. K. (1988) Quest for Controlled Combustion Engines. *SAE Paper* 880572.
88. Pierpont, D. A. and Reitz, R. D. (1995) Effects of Injection Pressure and Nozzle Geometry on D.I. Diesel Emissions and Performance. *SAE Paper* 950604.
89. Poling, B. E., Prausnitz, J. M., and O'Connell, J. P. (2001) *The Properties of Gases and Liquids.* 5th ed., New York, McGraw-Hill.
90. Poreh, M., Tsuei, Y. G., and Cermak, J. E. (1967) Investigation of a Turbulent Radial Wall Jet. *Journal of Fluids Engineering-Transactions of the ASME*, **34**, 457-463.
91. Pucher, G. R., Gardiner, D. P., Bardon, M. F., and Battista, V. (1996) Alternative Combustion Systems for Piston Engines Involving Homogeneous Charge Compression Ignition Concepts--A Review of Studies Using Methanol, Gasoline and Diesel Fuel. *SAE Paper* 962063.
92. Ryan III, T. W. and Callahan, T. J. (1996) Homogeneous Charge Compression Ignition of Diesel Fuel. *SAE Paper* 961160.
93. Ryan III, T. W., Callahan, T. J., and Mehta, D. (2004) HCCI in a Variable Compression Ratio Engine - Effects of Engine Variables. *SAE Paper* 2004-01-1971.
94. Ryan III, T. W. and Matheaus, A. C. (2003) Fuel Requirements for HCCI Engine Operation. *SAE Paper* 2003-01-1813.
95. Schefer, R. W. (1997) Flame Sheet Imaging Using CH Chemiluminescence. *Combustion Science and Technology*, **126**, 255-270.
96. Schlichting, H. (1979) *Boundary-Layer Theory.* 7th ed., New York, McGraw-Hill.
97. Settles, G. S. (2001) *Schlieren and Shadowgraph Techniques: Visualizing Phenomena in Transparent Media.* Berlin, Springer.
98. Shimazaki, N., Minato, A., and Nishimura, T. (2007) Premixed Diesel Combustion Using Direct Injection near Top Dead Centre. *International Journal of Engine Research*, **8**, 259-270.

99. Shimazaki, N., Tsurushima, T., and Nishimura, T. (2003) Dual Mode Combustion Concept with Premixed Diesel Combustion by Direct Injection near Top Dead Center. *SAE Paper* 2003-01-0742.
100. Siebers, D. L. (1998) Liquid-Phase Fuel Penetration in Diesel Sprays. *SAE Paper* 980809.
101. Siebers, D. L. (1999) Scaling Liquid-Phase Fuel Penetration in Diesel Sprays Based on Mixing-Limited Vaporization. *SAE Paper* 1999-01-0528.
102. Siebers, D. L. and Higgins, B. S. (2001) Measurement of the Flame Lift-Off Location on DI Diesel Sprays Using OH Chemiluminescence. *SAE Paper* 2001-01-0918.
103. Smallwood, G. J. and Gulder, O. L. (2000) Views on the Structure of Transient Diesel Sprays. *Atomization and Sprays*, **10**, 355-386.
104. Song, L. and Abraham, J. (2003) Entrainment Characteristics of Transient Turbulent Round, Radial and Wall-Impinging Jets: Theoretical Deductions. *Journal of Fluids Engineering-Transactions of the ASME*, **125**, 605-612.
105. Stanglmaier, R. H. and Roberts, C. E. (1999) Homogeneous Charge Compression Ignition (HCCI): Benefits, Compromises, and Future Engine Applications *SAE Paper* 1999-01-3682.
106. Su, T. F. and Farrell, P. V. (1998) Characterization of High-Injection-Pressure Diesel Sprays with Relation to Particulate and NOx Emissions. *Atomization and Sprays*, **8**, 83-107.
107. Suzuki, H., Koike, N., Ishii, H., and Odaka, M. (1997) Exhaust Purification of Diesel Engines by Homogeneous Charge with Compression Ignition Part 1: Experimental Investigation of Combustion and Exhaust Emission Behavior under Pre-Mixed Homogeneous Charge Compression Ignition Method. *SAE Paper* 970313.
108. Suzuki, H., Koike, N., and Odaka, M. (1998) Combustion Control Method of Homogeneous Charge Diesel Engines. *SAE Paper* 980509.
109. Suzuki, M., Nishida, K., and Hiroyasu, H. (1993) Simultaneous Concentration Measurement of Vapor and Liquid in an Evaporating Diesel Spray. *SAE Paper* 930863.
110. Takeda, Y., Keiichi, N., and Keiichi, N. (1996) Emission Characteristics of Premixed Lean Diesel Combustion with Extremely Early Staged Fuel Injection. *SAE Paper* 961163.
111. Tanner, F. X., Feigl, K. A., Ciatti, S. A., Powell, C. F., Cheong, S. K., Liu, J., and Wang, J. (2006) Structure of High-Velocity Dense Sprays in the Near-Nozzle Region. *Atomization and Sprays*, **16**, 579-597.
112. Thermodynamics Research Center (1982) *Selected Values of Properties of Hydrocarbons and Related Compounds*. College Station, Texas A&M University.
113. Tree, D. R. and Svensson, K. I. (2007) Soot Processes in Compression Ignition Engines. *Progress in Energy and Combustion Science*, **33**, 272-309.
114. Tsujimura, T., Oguma, M., and Goto, S. (2008) A Study of Fuel Auto-Ignitability on Premixed Compression Ignition Characteristics. *SAE Paper* 2008-01-0062.
115. Van de Hulst, H. C. (1981) *Light Scattering by Small Particles*. New York, Dover.
116. Verhoeven, D., Vanhemelryck, J.-L., and Baritaud, T. (1998) Macroscopic and Ignition Characteristics of High-Pressure Sprays of Single-Component Fuels. *SAE Paper* 981069.
117. Wilhelmsson, C., Tunestal, P., and Johansson, B. (2007) Operation Strategy of a Dual-Fuel HCCI Engine With VGT. *SAE Paper* 2007-01-1855.
118. Witze, P. O. and Dwyer, H. A. (1976) The Turbulent Radial Jet. *Journal of Fluid Mechanics*, **75**, 401-417.
119. Wu, P.-K. and Faeth, G. M. (1993) Aerodynamic Effects on Primary Breakup of Turbulent Liquids. *Atomization and Sprays*, **3**, 265-289.
120. Yanagihara, H., Satou, Y., and Mizuta, J. (1996) A Simultaneous Reduction of NO_x and Soot in Diesel Engines under a New Combustion System (Uniform Bulky Combustion System - UNIBUS). *17th Int. Vienna Motor Symposium.*
121. Yokota, H., Kudo, Y., Nakajima, H., Kakegawa, T., and Suzuki, T. (1997) A New Concept for Low Emission Diesel Combustion. *SAE Paper* 970891.
122. Yokota, H., Nakajima, H., and Kakaegawa, T. (1998) A New Concept for Low-Emission Diesel Combustion (2nd Report: Reduction of HC and CO Emission, and Improvement of Fuel Consumption by EGR and MTBE Blended Fuel). *SAE Paper* 981933.
123. Yue, Y., Powell, C. F., Poola, R., Wang, J., and Schaller, J. K. (2001) Quantitative Measurements of Diesel Fuel Spray Characteristics in the Near-Nozzle Region Using X-Ray Absorption. *Atomization and Sprays*, **11**, 471-490.

124. Yule, A. J. and Salters, D. G. (1995) The Breakup Zone of a Diesel Spray, Part 1, Length of Zone and Volume of Unatomized Liquid. *Atomization and Sprays*, **5**, 157-174.
125. Yule, A. J. and Watkins, A. P. (1991) Measurement and Modeling of Diesel Sprays. *Atomization and Sprays*, **1**, 441-465.
126. Zhang, Y. (2001) *A Study on Mixture Formation in Diesel Sprays with Split Injection Strategy.* Ph.D. Dissertation, University of Hiroshima.
127. Zhang, Y. and Nishida, K. (2004) Imaging of Vapor/Liquid Distributions of Split-Injected Diesel Sprays in a Two-Dimensional Model Combustion Chamber. *Combustion Science and Technology*, **176**, 1465 - 1491.
128. Zhang, Y., Nishida, K., and Yoshizaki, T. (2001) Quantitative Measurement of Droplets and Vapor Concentration Distributions in Diesel Sprays by Processing UV and Visible Images. *SAE Paper* 2001-01-1294.
129. Zhang, Y., Yoshizaki, T., and Nishida, K. (2000) Imaging of Droplets and Vapor Distributions in a Diesel Fuel Spray by Means of a Laser Absorption-Scattering Technique. *Applied Optics*, **39**, 6221-6229.
130. Zhao, H. and Ladammatos, N. (2001) *Engine Combustion Instrumentation and Diagnostics.* Warrendale, SAE.
131. Zhao, H. and Ladommatos, N. (1998a) Optical Diagnostics for In-cylinder Mixture Formation Measurements in IC Engines. *Progress in Energy and Combustion Science*, **24**, 297-336.
132. Zhao, H. and Ladommatos, N. (1998b) Optical Diagnostics for Soot and Temperature Measurement in Diesel Engines. *Progress in Energy and Combustion Science*, **24**, 221-255.